Application of solid state NMR for the study of surface bound species and fossil fuels

by

Stacey Althaus

A dissertation submitted to the graduate faculty

in partial fulfillment of the requirements for the degree of

DOCTOR OF PHILOSOPHY

Major: Physical Chemistry

Specialization: Instrumentation

Program of Study Committee:

Marek Pruski, Co-major Professor
Aaron Sadow, Co-major Professor
Igor Slowing
Theresa Windus
Wenyu Huang

Iowa State University

Ames, Iowa

2014

ProQuest LLC.
789 East Eisenhower Parkway
P.O. Box 1346
Ann Arbor, MI 48106 - 1346

TABLE OF CONTENTS

ACKNOWLEDGEMENTS

The past six years have been an adventure and there are many people I would like to thank for helping me navigate my way through this time. First of all I would like to thank my PhD advisor, Marek Pruski, for his support and guidance over the years. Thank you for helping me to learn to think more critically and express my research more clearly. I would also like to thank my committee members past and present: Dr. Aaron Sadow, Dr. Igor Slowing, Dr. Klaus Schmidt-Rohr, Dr. Theresa Windus, Dr. Wenyu Huang, Dr. Patricia Thiel, Dr. Brian Trewyn and the late Dr. Victor Shang-Yi Lin, for their support and suggestions over the years. You have all been great mentors and teachers to me, both inside and outside of the class room.

The support of the Pruski group members has been invaluable over my years in graduate school. Thank you to Dr. Jennifer Rapp, who not only helped me start my research and acquire my first solids spectrum, but was also there as a good friend. Dr. Jerzy Wiench and Dr. Kanmi Mao, thank you for helping me start my research and working with me on a number of my projects. Dr. Takeshi Kobayashi, who is a never ending fountain of knowledge, thanks for dealing with my never ending train of questions and helping me with so much. Jennifer Goldston and Andra Castle thanks for being there when questions arose, either lab or life related.

During my time here I was also lucky to have a number of collaborative studies with researchers outside the Pruski group. Specifically I would like to thank Dr. Kapil

Kandel, Dr. Justin Valenstein, Dr. Brian Trewyn and Dr. Igor Slowing for letting me take part in their amazing work on mesoporous nanoparticles. Their confidence in me helped me grow as a researcher. A big thank you is also due to Dr. Gordon Kenendy at Exxon Mobile, who was instrumental in my coal study and a true joy to work with.

On a more personal note, I want to thank my parents, Jean and Carl Althaus, for their encouragement and belief in me, as well as the rest of my family, for their understanding and support over the past six years. It was great knowing that you were there for me, no matter what.

To my friends, you know who you are, who were there for scientific talks, personal talks, grabbing a meal (or a beer), crafting, canoeing, going for bike ride, heading to yoga, traveling, or anything else that helped relieve the stress of graduate school, thank you for being there. You all made Ames a great place to be and made the graduate experience a much more enjoyable one. And most of all a very heartfelt and loving thank you to James Hofmann, for encouraging me and trying to keep my life in perspective. Thank you for your patience as I dealt with the craziness of graduate school, and for being there to support me and pick me up when I was down.

CHAPTER 1: AN INTRODUCTION TO SOLID STATE NUCLEAR MAGNETIC RESONANCE

General NMR

Nuclear Magnetic Resonance (NMR) is a popular spectroscopic technique because it can provide atomic-scale structural and dynamic information on a diverse assortment of systems. Not only can NMR detect small changes in the local environment, it is also non-destructive and can utilize a variety of available NMR-active nuclei. Although NMR was first demonstrated in solids [1], it quickly became a popular technique for the detection of liquid samples since very narrow lines could be obtained in these spectra [2]. Thanks to a multitude of advances in the hardware and software, solid-state (SS) NMR resurged in the 1980s. One of the main drawbacks of SSNMR is the broadened line shape caused by the anisotropic interactions in powder-like systems that are averaged out in liquids to isotropic values by the fast rotational motion. The development of magic angle spinning (MAS) [3], discussed in more detail in section 4, allowed spectroscopists to measure solids with improved resolution. Other advances, including multiple pulse sequences (such as those used for homonuclear decoupling), higher magnetic fields, and improvements in probe design have also enhanced the progress of SSNMR. Nonetheless, SSNMR's quest for improved sensitivity and resolution continues until this day.

This chapter will introduce the basics of NMR by describing the vector and quantum mechanical models. MAS and its benefits will also be described in more detail,

along with several important pulse sequences that will be used throughout the following chapters to examine a variety of materials including coals and mesoporous nanoparticles.

Vector Model

Net Magnetization

Before approaching the more complex quantum mechanical model of NMR, one can first examine NMR from a semi-classical approach via the vector model. The vector model is a simplified way of visualizing a nuclear spin system, especially during basic pulsed NMR experiments involving isolated spin pairs.

In the vector model we examine the net magnetization vector $\vec{M}$ which is a sum of the individual magnetic spin moment $\vec{\mu}$ possessed by each nuclei. The magnetic spin moment is related to the nuclear spin operator $\hat{\mathbf{I}}$ by

$$\vec{\boldsymbol{\mu}} = \boldsymbol{\gamma}\hbar\hat{\vec{\mathbf{I}}} \tag{1-1}$$

where the gyromagnetic ratio γ is unique to each type of nuclei. Without a magnetic field the net magnetization in most materials is zero. However, when a sample is placed in a magnetic field $\vec{B}_0$ a small net magnetization is induced along the $\vec{B}_0$direction (Figure 1).

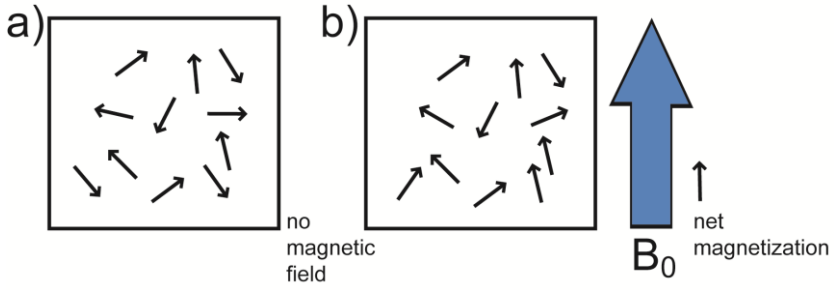

Figure 1. When no magnetic field is present the overall net magnetization is zero (a). The introduction of a magnetic field, $\vec{B}_0$, creates a small overall net magnetization vector, $\vec{M}$, aligned with $\vec{B}_0$ (b).

This induced effect minimizes the magnetic energy. For nuclei with positive γ, such as ^{1}H or ^{13}C, the lower energy is associated with vector $\vec{\mu}$ being aligned parallel with the magnetic field, while the higher energy corresponds to the anti-parallel orientation. Despite thermal motion, which causes randomization, the small net magnetization along $\vec{B}_0$ persists as long as the sample remains undisturbed in the external magnetic field, giving a non-zero magnetization of bulk sample.

Precession

When the bulk magnetization vector is tipped away from the $\vec{B}_0$, it rotates in a cone about the $\vec{B}_0$ direction (Figure 2). This motion is referred to as precession. The frequency ω_0 often referred to as the Larmor frequency, at which the precession occurs in a fixed magnetic field is given by:

$$\vec{\omega}_0 = -\gamma \vec{B}_0 \, . \qquad (1\text{-}2)$$

The precession of non-equilibrium magnetization can be detected via induced current in a coil around the sample. The resulting signal is often referred to as the free induction decay (FID). This time domain signal can then be Fourier transformed to the frequency domain, which yields the spectra that can serve as fingerprints of individual nuclei in the sample.

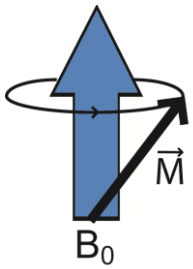

Figure 2. When the net magnetization vector is tipped away from alignment with the external magnetic field (*i.e.,* by an RF pulse) the vector precesses about the magnetic field at the Larmor frequency ω_0.

Radiofrequency Pulses in Vector Model

At equilibrium, the magnetization vector is aligned with $\vec{B}_0$, typically aligned along the *z*-axis, therefore no measurable precession is occurring. In order to measure an FID, the vector must be tilted into the *x*-*y* plane. This is accomplished through the use of radiofrequency (RF) pulses within the coil, thereby creating a small magnetic field, $\vec{B}_1$. This small magnetic field along the *x*-(or *y*-) direction oscillates at or near the Larmor frequency of the specific nuclei. While $\vec{B}_1$ is much smaller than $\vec{B}_0$, under this resonance conditions the net spin magnetization can be moved away from the $\vec{B}_0$, as desired. The net magnetization vector will then precess about $\vec{B}_1$ with a frequency denoted as $\vec{\omega}_1$. When the $\vec{B}_1$ field is removed the spins will once again precess about the $\vec{B}_0$.

Although the vector can be used to describe the behavior of the spins under single pulse RF excitation, or during simple pulse sequences, such an approach is inadequate to describe the spin evolution during more complex experiments. In general, a more advanced, quantum-mechanical treatment is needed.

The Quantum Mechanics of NMR

Although the vector model can help to understand the basics of NMR, it has its limitations. To describe the behavior of a coupled spin system or explain the functioning of a complicated pulse sequence, a fundamental understanding of the quantum mechanics of NMR is essential. As a starting point, it must be remembered that spectroscopy examines the transitions between states corresponding to different energy levels. In the quantum mechanics treatment the total energy of the system is found through the Hamiltonian operator $\hat{H}$. When the system can be described by a time-independent Hamiltonian, its allowed energy levels can be found by solving the Schrödinger equation, $\hat{H}\Psi = E\Psi$, where Ψ is the eigenfunction representing the stationary state.

The Nuclear Spin Hamiltonian

The Hamiltonian operator of a nuclear spin can be written as a sum of the following terms

$$\hat{H}_{NMR} = \hat{H}_0 + \hat{H}_{CS} + \hat{H}_D + \hat{H}_J + \hat{H}_Q \qquad (1\text{-}3)$$

where $\hat{H}_0$ is the Zeeman interaction Hamiltonian, $\hat{H}_{CS}$ is the chemical shielding Hamiltonian, $\hat{H}_D$ is the dipolar coupling Hamiltonian, $\hat{H}_J$ is the *J*-coupling Hamiltonian and $\hat{H}_Q$ is the quadrupolar Hamiltonian. Each term will now be discussed individually.

The Zeeman Interaction

The dominant interaction in NMR is the Zeeman effect, which arises from the interaction of the spin system with the external magnetic field. This results in the difference in population of spin levels that is exploited in NMR spectroscopy. The Zeeman Hamiltonian can be written as:

$$\hat{H}_0 = -\gamma\hbar\hat{\mathrm{I}}_z \cdot \vec{\mathrm{B}}_0 = \hat{\mu} \cdot \vec{\mathrm{B}}_0 \,. \tag{1-4}$$

For non-interacting spin-1/2 nuclei, the solution of the corresponding Schrödinger equation yields two energy values, separated by the Larmor frequency with the corresponding eigenstates denoted as α and β. Most NMR experiments can be described using the so-called high-field approximation. Under this condition, the Zeeman part of $\hat{H}_{NMR}$ is dominant, thereby allowing all other interactions in equation (1-3) to be treated as perturbations. The effect of these interactions on the NMR spectra can be estimated as first-order corrections to the Zeeman energies. These perturbations are extremely important in the determination of chemical structure and the environment of the molecule, as described in more detail below.

Chemical Shielding

NMR has unique sensitivity to the local atomic-scale environment. The nuclear spins not only interact with the external magnetic field $\vec{\mathrm{B}}_0$, but also the local fields created by the surrounding nuclei and electrons. In particular, the electrons create their own secondary magnetic field, which opposes $\vec{\mathrm{B}}_0$, thereby having a shielding effect on the nuclei relative to those with no electron density. The chemical shielding Hamiltonian

can be represented by:

$$\hat{H}_{CS} = -\gamma\hbar\hat{\vec{I}} \cdot \boldsymbol{\sigma} \cdot \vec{B}_0 \qquad (1\text{-}5)$$

where $\boldsymbol{\sigma}$ is a second-rank tensor, also known as the chemical shift tensor. In general, this tensor is not spherically symmetric and its effect is therefore sensitive to its alignment with respect to $\vec{B}_0$. As a second rank tensor, chemical shift is typically represented by a 3x3 matrix, which is most easily defined in the principal axis frame (PAF), where the matrix is diagonal. This leads to a shift tensor which can be visualized by an ellipsoid centered on a nucleus (Figure 3). In the principal axis frame the three principal values are often expressed as isotropic chemical shift, $\sigma_{iso} = \frac{1}{3}(\sigma_{xx}^{PAF} + \sigma_{yy}^{PAF} + \sigma_{zz}^{PAF})$; the anisotropy of interaction, $\Delta = \sigma_{zz}^{PAF} - \sigma_{iso}$; and the asymmetry, $\eta = (\sigma_{xx}^{PAF} - \sigma_{yy}^{PAF})/\sigma_{zz}^{PAF}$, which describe the shielding tensor.

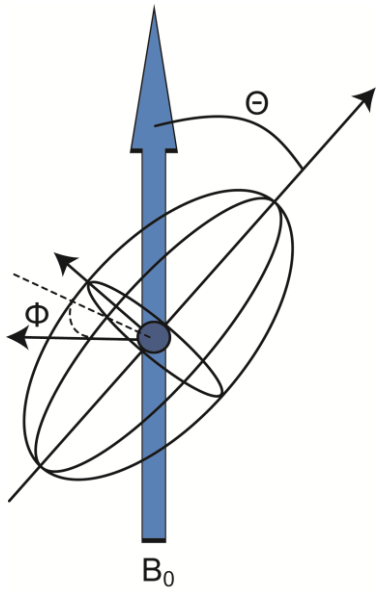

Figure 3. A representation of the ellipsoid principal axis frame shielding tensor shown with respect to B_0.

If the $\vec{B}_0$ is oriented along the *z*-axis, the Hamiltonian becomes

$$\hat{H}_{CS} = -\frac{\gamma\hbar}{2\pi}\hat{I}_z \cdot \sigma_{zz}^{lab} \cdot B_0. \quad (1\text{-}6)$$

We can now use Schrodinger's equation to determine the first order energy contributions of the two spin states. The spectral frequency contribution from chemical shielding ω_{CS} can be calculated as the transition energy between these two levels:

$$\omega_{CS} = -\gamma\sigma_{zz}^{lab}B_0 = \omega_0\sigma_{zz}^{lab} \quad (1\text{-}7)$$

in the laboratory frame. We can represent this frequency with respect to the principal axis frame as

$$\omega_{CS}(\theta,\phi) = -\frac{1}{2}\omega_0\sigma_{zz}^{PAF}(3\cos^2\theta - 1)$$

$$= -\omega_0\sigma_{iso} - \frac{1}{2}\omega_0\Delta(3\cos^2\theta - 1 + \eta\sin^2\theta\cos 2\phi) \quad (1\text{-}8)$$

where θ and ϕ are the polar angles represented in Figure 3. In powder samples, all orientations of θ and ϕ are random and their resulting contributions yield anisotropically broadened spectra, referred to as powder patterns. Manipulation of these angles with respect to $\vec{B}_0$ eventually gave rise to the concept of magic angle spinning (MAS), which is discussed in more detail in section 4.

Note that the total spectral frequency is $\omega = \omega_0 + \omega_{CS}$. Of course when referring to the chemical shift in spectra the absolute value is not generally used, instead the reported chemical shifts are typically referenced with respect to a standard, typically in parts-per million (ppm). In the case of ^{1}H, ^{13}C, and ^{29}Si, trimethylsilane (TMS) is often used as the reference compound.

Dipolar Coupling

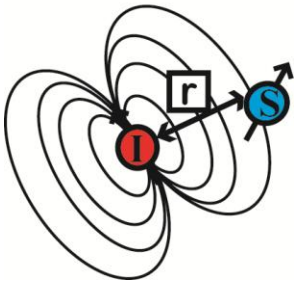

Figure 4. The magnetic field from spin I affects the environment of a neighboring spin S, over the distance $\vec{r}$ which is related to the strength of this dipolar interaction.

Unlike the chemical shift, where an electron-induced magnetic field leads to a shift of the resonance frequency, dipolar coupling depends on the field from the neighboring nuclei (Figure 4). This effect is often called "direct dipole-dipole coupling" or "through-space dipolar coupling". While this dipolar interaction averages to zero in liquids due to molecular tumbling it is important to note that this is not the case in solids. In fact, this interaction can be the major cause of line broadening in a solid sample. The interaction Hamiltonian between two spins, I and S, can be written as:

$$\widehat{H}_D = -\left(\frac{\mu_0}{4\pi}\right)\gamma_I\gamma_S\hbar\left(\frac{\vec{I}\cdot\vec{S}}{r^3} - \frac{3(\vec{I}\cdot\vec{r})(\vec{S}\cdot\vec{r})}{r^5}\right) = -2\,\hat{\vec{I}}\cdot D\cdot\hat{\vec{S}} \qquad (1\text{-}9)$$

where S is the second spin and the source of the local field at spin I, $\vec{r}$ is the distance between the spins, and D is the dipolar coupling tensor. The dipolar coupling tensor, which is always axially symmetric, has principal values of -d/2, -d/2 and d, where d, the dipolar coupling constant, can be written as:

$$d = \frac{\hbar\mu_0}{4\pi}\frac{1}{r^3}\gamma_I\gamma_S. \qquad (1\text{-}10)$$

In the case of a homonuclear spin pair, spins I and S represent the same type of nuclei ($\gamma_I = \gamma_S$) and the homonuclear dipolar coupling Hamiltonian can be written as

$$\hat{H}_D^{homo} = -\mathrm{d} \cdot \frac{1}{2}(3\cos^2\theta - 1)(3\hat{\mathrm{I}}_z\hat{\mathrm{S}}_z - \hat{\vec{\mathrm{I}}} \cdot \hat{\vec{\mathrm{S}}}) \quad (1\text{-}11)$$

where θ is the angle between the I-S vector and $\vec{B}_0$. In the heteronuclear case spins, I and S are different ($\gamma_I \neq \gamma_S$). Since the precession of spin S is no longer at or near the resonance frequency of spin I, the Hamiltonian for the heterogeneous case can be simplified to

$$\hat{H}_D^{hetero} = -\mathrm{d}(3\cos^2\theta - 1)\hat{\mathrm{I}}_z\hat{\mathrm{S}}_z. \quad (1\text{-}12)$$

J-Coupling

In contrast to the through-space nature of the dipolar coupling, indirect coupling or *J*-coupling, is a through-bond effect. This interaction arises from the effect of bonding electrons on the local field experienced at the nucleus, thus allowing the exploration of chemical structure. *J*-coupling is not averaged by isotropic motion, therefore it can be easily observed in solution state spectra (*i.e.,* the multiplet structure commonly observed in solution NMR). In solids, however, the *J*-coupling is typically small in comparison to the other interactions and is often obscured due to broadening. As such, the *J*-coupling term was largely ignored in SSNMR until recent advances in fast MAS and homonuclear decoupling allowed the *J*-coupling to be exploited in solids spectra, as further described in section 5 and chapters 2 and 3. The *J*-coupling Hamiltonian can be represented as:

$$\hat{H}_J = -J_{IS}\hat{\mathrm{I}}_z\hat{\mathrm{S}}_z \quad (1\text{-}13)$$

where J_{IS} is the *J*-coupling constant. Note that the *J*-Hamiltonian does not depend on the magnetic field. Thus, J_{IS} is typically reported in Hertz (Hz).

Quadrupolar Coupling

The last of the internal Hamiltonians in equation (1-3) is one that will not be of significance in this work, but is important to acknowledge nonetheless. Nuclei with spins greater than ½, which constitute about 70% of all NMR-active nuclei, possess a non-spherical distribution of the electric charge and thus a non-zero quadrupole moment. The strength of quadrupolar interaction is determined by the magnitude of the nuclear quadrupole moment and the strength of the local electric field gradient created at the nuclear site. We can represent the quadrupolar coupling as:

$$\hat{H}_Q = \frac{eQ}{6I(2I-1)\hbar}\,\vec{\hat{I}} \cdot V \cdot \vec{\hat{I}} \tag{1-14}$$

where e is the electric charge of a proton, Q is the quadrupole moment, and V is the electric field gradient tensor.

Radiofrequency Pulses

The previous sections discussed interactions that are intrinsic to the nuclear spins. As mentioned earlier, NMR spectroscopists use sequences of RF pulses to manipulate various parts of the spin Hamiltonians. These RF pulses introduce an oscillating magnetic field, $\vec{B}_1$ which, in turn, introduces a time-dependence to the spin system, and therefore mixes the Zeeman states. The time-dependent Schrödinger equation must be used, along with a time-dependent spin wavefuntion. The RF Hamiltonian for an on-resonance RF pulse can be represented as

$$\hat{H}_{RF} = -\gamma\hbar(\hat{I}_z\vec{B}_0 + \hat{I}_x\vec{B}_1\cos(\omega_{RF}t)). \tag{1-15}$$

This section introduced the Hamiltonian operators commonly associated with NMR. Next we will discuss how we can exploit some of these terms to yield better resolved spectra in the solid state.

Magic Angle Spinning (MAS)

Mathematical Representations

The chemical shift and dipolar Hamiltonians have a notable similarity in their dependence on the orientation of the chemical shift tensor and internuclear vector, respectively, with respect to $\vec{B}_0$, in the form of $1/2(3\cos^2\theta-1)$. This orientational term vanishes under isotropic motion, which leads to a lack of anisotropic broadening in solution state NMR. In the 1950s [3] a way to effectively reduce this broadening in solids was demonstrated by spinning the sample at the so-called magic angle, a technique now commonly referred to as magic angle spinning (MAS).

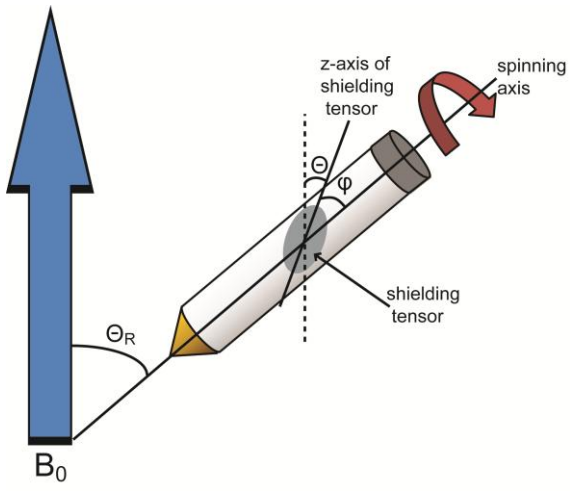

Figure 5. A diagram depicting MAS in the laboratory frame with a randomly oriented shielding tensor.

It can be shown that spinning the sample about any given axis leads to the following average value of the anisotropic term:

$$\langle 3\cos^2\theta - 1\rangle = \frac{1}{2}(3\cos^2\theta_R - 1)(3\cos^2\varphi - 1) \qquad (1\text{-}16)$$

where θ_R is the angle between the spinning axis and $\vec{B}_0$, and φ is the angle between the z-axis of the shielding tensor and the spinning axis. The experimenter has control over θ_R, whereas, θ and φ will vary for each nucleus in a powder. Manipulation of the spinning axis such that θ_R is equal to 54.74° causes the anisotropic average to vanish (*i.e.,* $3\cos^2\theta$-1=0) and therefore leads to substantially narrowed lines when the spinning speed is faster than the static linewidth.

Advantages of Fast MAS

In many of my studies, fast MAS, considered to be any MAS rate above 25 KHz, has been utilized to reap some of its many benefits, as will be detailed in this section [4]. Current maximum spin rates are as high as 110 kHz [5-6]. Despite the tiny rotor size required by faster spinning probes, the sensitivity per scan compensates, to a large extent, for the much smaller sample amount, as shown in Figure 6 [7].

One of the advantages of fast MAS is the removal of spinning sidebands. In the spectra acquired at MAS rates smaller than the inhomogeneous linewidth, the spinning sidebands appear on both sides of the isotropic peak, lowering the sensitivity and needlessly polluting the spectra.

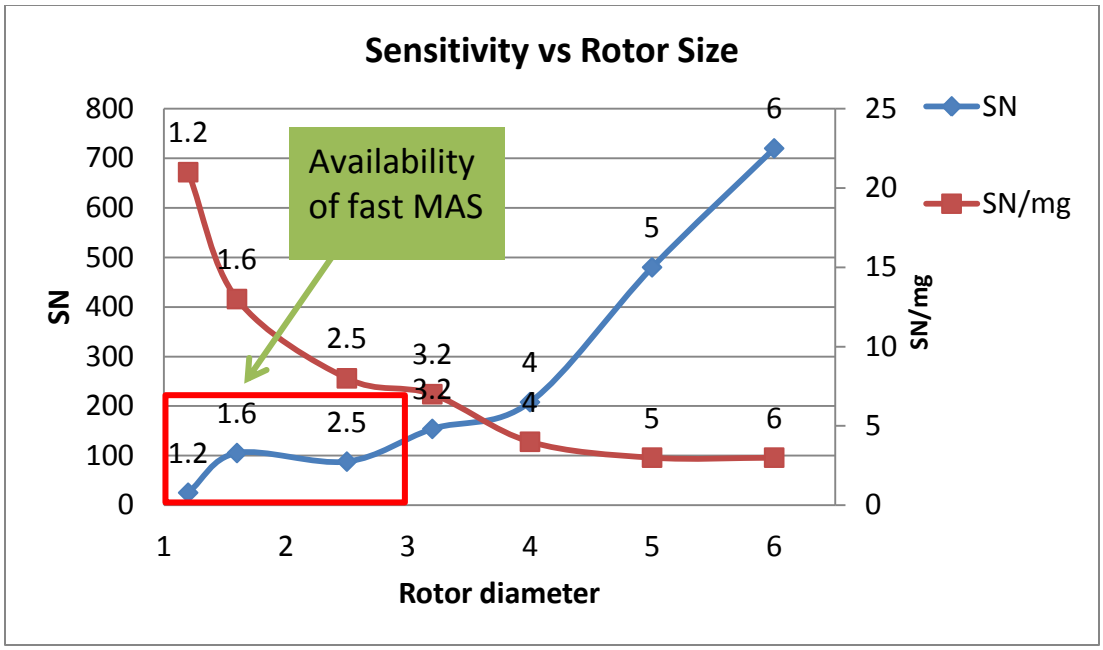

Figure 6. The overall sensitivity and sensitivity per milligram of sample are compared across different rotor sizes.

Another benefit of ultrafast spinning is associated with heteronuclear decoupling. Heteronuclear dipolar coupling can cause broadening in spectra, which can be removed by various RF decoupling sequences. At slow spinning speeds, these sequences require the use of very high RF power to be effective. Under fast MAS, however, lower power RF pulses can be used effectively to decouple the system, which decreases the sample heating and risk to the probe circuitry [8-9].

Finally, fast MAS proved to be fully compatible with the RF sequences for homonuclear decoupling. For more than two decades, highly resolved spectra of strongly coupled high-gamma nuclei, such as ^{1}H and ^{19}F, could be only obtained by combining RF homonuclear decoupling schemes with MAS at slow rate. It has recently been demonstrated that some of the modern RF homonuclear decoupling schemes, such as

phase-modulated Lee Goldberg (PMLG) and frequency-modulated LG (FMLG), work surprisingly well under MAS at 40+ kHz [10], leading to resolution that could not be achieved using traditional approaches. The homonuclear decoupling of spins under such conditions has also been reported to increase the transverse dephasing time for a spin echo (T_2' relaxation) [11-12]. These benefits of fast MAS have allowed for the use of sequences that were previously unavailable in solids, some of which will be described in the following section.

Methods

Cross Polarization

One commonly applied method in SSNMR is cross-polarization (CP)MAS [13]. CPMAS exploits the heteronuclear dipolar coupling to transfer polarization between nuclear spin pairs, typically consisting of an abundant spin I with a high gyromagnetic ratio, such as ^{1}H or ^{19}F, and a dilute, low- γ S spin, such as ^{13}C or ^{15}N. One of the major benefits of CPMAS is that the recycle delay is governed by the abundant nuclei, which generally relax faster than dilute nuclei, thus leading to higher acquisition rates and shorter overall experimental times. In addition, the more favorable Boltzmann distribution factor associated with the high-γ nucleus is transferred to the dilute spins, thereby enhancing the signal obtained per scan.

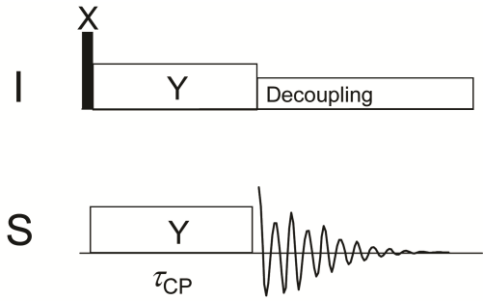

Figure 7. The pulse sequence for a typical CPMAS experiment with heteronuclear decoupling during acqusition.

The basic CPMAS sequence is shown in Figure 7. First, a 90° pulse is applied at or near the frequency of the I-spins, flipping the I-magnetization onto the *x*-*y* plane. This is followed by a contact pulse (or sequence of pulses) at the I-frequency, which effectively spin-locks the magnetization along the *y*-direction. Simultaneously a similar pulse is applied to the S-channel. If the corresponding B_1 fields are properly adjusted in both channels, fulfilling the so-called Hartmann-Hahn matching condition [14], the polarization of I nuclei can be transferred to S-spins via the dipolar coupling interactions. The matching condition under fast MAS is explored in chapter 2 of this thesis. The duration of cross-polarization (τ_{CP}) can be varied in order to provide information about the internuclear distances and local molecular dynamics. Following the polarization transfer, the signal is acquired in the S-channel, while heteronuclear decoupling is applied to I-spins, to reduce line broadening from heteronuclear interactions. This technique will be used frequently throughout the studies in this thesis to examine a variety of functionalities.

INEPT

The development of fast MAS has led to the availability of new sequences that were previously only used in NMR of liquids. One of these sequences, which was not available at slow MAS rates, is insensitive nuclei enhanced by polarization transfer, or INEPT [15]. In this sequence the magnetization is transferred between nuclei via the weak *J*-coupling. In order for the relaxation to not destroy the signal, a combination of fast MAS and strong homonuclear decoupling (such as PMLG) is needed.

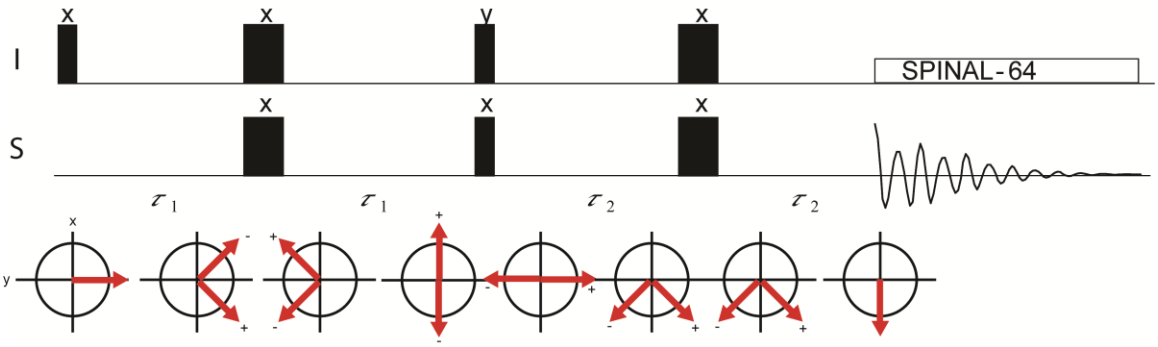

Figure 8. The 1D refocused INEPT (INEPTR) sequence with spinal heteronuclear decoupling during acquisition.

In Figure 8 the so-called refocused INEPT (INEPTR) sequence is shown. Initially a 90° pulse flips I-magnetization to the *x*-*y* plane and then a delay, τ_1, is implemented in which the spins can precess. This delay is optimized when it is 1/4*J*. A 180° pulse is then used to flip the spins to the mirror image positions. The same τ_1 delay is then followed by a 90° pulse. This pulse effectively moves the I-magnetization to the *z*-axis, and rotates the S-magnetization. A new delay, τ_2, is introduced, which is optimal at 0.3/*J*. A 180° refocussing pulse is applied to deter interference from the chemical shift. The τ_2 delay then allows the S-spins to refocus and the spectrum can then be acquired under

heteronuclear decoupling at the I-spin frequency. Since this method relies on magnetization transfer using *J*-coupling, it is often referred to as "through-bond". This method of magnetization transfer combined with indirect detection (next section) and ^{1}H homonuclear decoupling (PMLG) allows for the measurement of through-bond 2D spectra, as will be shown in chapters 2 and 3 of this thesis.

Indirect Detection

Another of the methods previously unavailable at slow MAS rates is heteronuclear single quantum coherence (HSQC) spectroscopy, in which a 2D spectrum is acquired by detection on the high-gamma nuclei. Historically the detection of ^{1}H during t_2 was undesirable in solids due to excessive line broadening, which required the use of RF homonuclear decoupling during detection. However, thanks to sufficient line narrowing by fast MAS alone, 2D spectra can be obtained via ^{1}H detection. This can lead to a large sensitivity advantage g, given by:

$$g \propto \left(\frac{\gamma_H}{\gamma_S}\right)^{3/2}\left(\frac{W_S}{W_H}\right)^{1/2} \quad (1\text{-}17)$$

where γ_H is the gyromagnetic ratio of ^{1}H, γ_S is the gyromagnetic ratio of spin S, W_S is the observed linewidth of S spins, and W_H is the observed linewidth of ^{1}H spins. This can lead to large enhancements for low-gamma nuclei, especially in cases where the ^{1}H linewidth is relatively narrow. Ishii and Tycko first reported a significant gain in sensitivity for the detection of ^{15}N enriched peptides via ^{1}H and this technique has since been shown in a variety of other systems including naturally abundant ^{13}C systems [16-20].

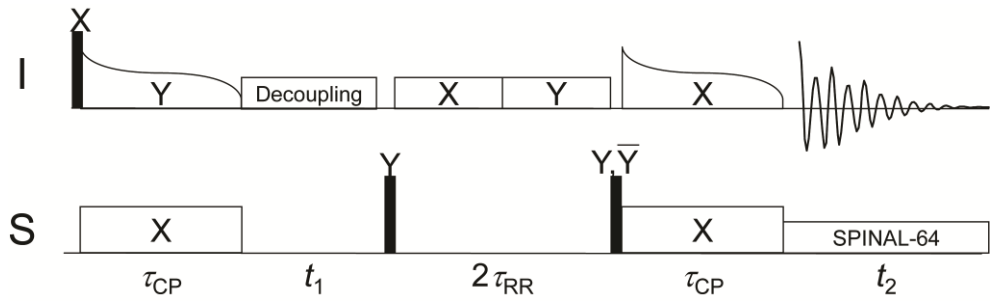

Figure 9. The pulse sequence for indirect detection with CP transfers.

The CP-CP indirectly detected pulse sequence is shown in Figure 9. This sequence first applies tangentially ramped CP to generate I-magnetization. This magnetization evolves during t_1 under I-spin heteronuclear decoupling and is subsequently stored along the *z*-axis for a period of $2\tau_{RR}$, during which time the uncorrelated I-magnetization is destroyed using the so-called rotary recoupling [21]. S-magnetization is then transferred back to the I-spins using another tangentially ramped CP. The decay of I-magnetization is then measured during t_2 with heteronuclear decoupling at the S-spin frequency. This sequence, along with a similar one which uses INEPT as the second magnetization transfer [12], will be used to collect 2D spectra in the following chapters.

References

[1] E.M. Purcell, H.C. Torrey, and R.V. Pound, Phys. Rev. 69 (1946) 37-38.

[2] F. Bloch, W.W. Hansen, and M. Packard, Phys. Rev. 69 (1946) 127-127.

[3] E.R. Andrew, A. Bradbury, and R.G. Eades, Nature 182 (1958) 1659-1659.

[4] A. Samoson, Extended Magic-Angle Spinning. in: D.M. Grant, and R.K. Harris, (Eds.), Encyclopedia of Nuclear Magnetic Resonance, John Willy & Sons, Chinchester, 2002, pp. 59-64.

[5] T. Kobayashi, K. Mao, P. Paluch, A. Nowak-Król, J. Sniechowska, Y. Nishiyama, D.T. Gryko, M.J. Potrzebowski, and M. Pruski, Angewandte Chemie International Edition 52 (2013) 14108-14111.

[6] Y. Nishiyama, Y. Endo, and T. Nemoto, 53rd ENC, Miami, FL, USA, 2012.

[7] A.R. Palmer, D. Rice, S. Hafner, and M. Cormos, Varian Report, 2007.

[8] M. Ernst, M.A. Meier, T. Tuherm, A. Samoson, and B.H. Meier, J. Am. Chem. Soc. 126 (2004) 4764-4765.

[9] S.P. Brown, X.X. Zhu, K. Saalwächter, and H.W. Spiess, J. Am. Chem. Soc. 123 (2001) 4275-4285.

[10] M. Leskes, S. Steuernagel, D. Schneider, P.K. Madhu, and S. Vega, Chem. Phys. Lett. 466 (2008) 95-99.

[11] B. Alonso, and D. Massiot, J. Magn. Reson. 163 (2003) 347-352.

[12] K. Mao, J.W. Wiench, V.S.-Y. Lin, and M. Pruski, J. Magn. Reson. 196 (2009) 92-95.

[13] A. Pines, M.G. Gibby, and J.S. Waugh, J. Chem.Phys. 59 (1973) 569-590.

[14] S.R. Hartmann, and E.L. Hahn, Phys. Rev. 128 (1962) 2042-2053.

[15] G.A. Morris, and R. Freeman, J. Am. Chem. Soc. 101 (1979) 760-762.

[16] Y. Ishii, and R. Tycko, J. Magn. Reson. 142 (2000) 199-204.

[17] B. Reif, and R.G. Griffin, J. Magn. Reson. 160 (2003) 78-83.

[18] E.K. Paulson, C.R. Morcombe, V. Gaponenko, B. Dancheck, R.A. Byrd, and K.W. Zilm, J. Am. Chem. Soc. 125 (2003) 15831-15836.

[19] V. Chevelkov, K. Rehbein, A. Diehl, and B. Reif, Angew. Chem. Int. Ed. 45 (2006) 3878-3881.

[20] J.W. Wiench, C.E. Bronnimann, V.S.Y. Lin, and M. Pruski, J. Am. Chem. Soc. 129 (2007) 12076-12077.

[21] T.G. Oas, R.G. Griffin, and M.H. Levitt, J. Chem. Phys. 89 (1988) 692.

CHAPTER 2: SOLID-STATE NMR STUDIES OF FOSSIL FUELS USING ONE- AND TWO-DIMENSIONAL METHODS AT HIGH MAGNETIC FIELD

A paper published in *Energy & Fue*ls, **26**, 4405-4412 (**2012**)

Stacey M. Althaus[†‡], *Kanmi Mao*[§], *Gordon J. Kennedy*[§], *Marek Pruski*[†‡]

[†] U.S. DOE Ames Laboratory, Iowa State University, Ames, IA 50011, USA

[‡] Department of Chemistry, Iowa State University, Ames, IA 50011, USA

[§] ExxonMobil Research and Engineering Co., 1545 Route 22E, Annandale, NJ 08801, USA

Abstract

We examine the opportunities offered by recent advancements in solid-state NMR methods, which increasingly rely on the use of high magnetic fields and fast magic angle spinning (MAS), in the studies of coals and other carbonaceous materials. The sensitivity of 1D and 2D experiments tested on several Argonne Premium Coal Samples is only slightly lower than that of traditional experiments performed at low field magnetic fields in large MAS rotors, since higher receptivity per spin and the use of ^{1}H detection of low-gamma nuclei can make up for most of the signal loss due to the small rotor size. The advantages of modern SSNMR methodology in these studies include improved

resolution, simplicity of pulse sequences, and the possibility of using *J*-coupling during mixing.

1. Introduction

The ever increasing need to optimize conversion of heavy fossil fuel resources into useful products in an environmentally benign and cost effective manner requires detailed understanding of the molecular structure and the reactivities [1]. One of the most powerful analytical methods for studying insoluble carbonaceous materials in bulk is solid-state nuclear magnetic resonance (SSNMR) spectroscopy, which for over three decades has been used as the primary source of information about concentrations of various carbon and hydrogen functionalities [2-11]. Numerous early investigations have suggested that the quantitative (to within a few %) ^{13}C intensities in coals could be best measured at low magnetic field, B_0 of 4.7 T or less, under slow magic angle spinning (MAS), at rates of 10 kHz or less, using variable-contact time cross-polarization (CP) or direct-polarization (DP) MAS experiments [4-10]. Specifically, it was accepted that the seemingly conflicting requirements of using MAS rates that exceed ^{13}C chemical shift anisotropies (CSAs), yet do not interfere with the CP process, could be best met under such conditions. Secondly, the inhomogeneously broadened lines in coals scale linearly with B_0, which partly negates the resolution and sensitivity advantage of a higher field. Lastly, the high-resolution ^{1}H NMR studies of coals using combined rotation and multiple-pulse spectroscopy (CRAMPS) were also carried out under low-field/slow-MAS conditions [8,12-13].

The continuous development of stronger magnets, more sensitive probes, higher spinning speeds, innovative pulse sequences and improved computational tools has led to

dramatic progress in SSNMR spectroscopy. Indeed, the availability of spectrometers operating at high magnetic field strengths brought about steady improvement in sensitivity and resolution. Recent advances in ultrafast MAS technology [14], which allow for sample spinning at 40-80 kHz [14-16], opened new opportunities for advancing multidimensional SSNMR experiments. The impact of fast MAS relies on excellent sensitivity per spin, great flexibility in using the radiofrequency (RF) magnetic fields, efficient CP transfer, increased frequency range of the indirect dimension in rotor-synchronized experiments, and elimination of the spinning sidebands at high magnetic fields or in the presence of large CSAs. In addition, fast MAS by itself or in combination with RF pulse sequences (CRAMPS) can be used to eliminate the strong ^{1}H-^{1}H homonuclear dipolar couplings at high magnetic fields [14,17]. This results in new opportunities for CP-based (through-space) and INEPT-based (through-bond) two-dimensional (2D) heteronuclear correlation (HETCOR) spectroscopy, e.g. using pulse sequences similar to single quantum correlation (HSQC) experiments [16,18-19]. In particular, under fast MAS it became possible to enhance the sensitivity of HETCOR NMR by detecting the nuclei with low gyromagnetic ratios (referred to as low-γ or X nuclei) indirectly via more sensitive, high-γ ^{1}H nuclei (the so-called indirect, or ^{1}H-detection) [15-18,20-21]. The sensitivity ratio between the indirect [X{^{1}H}-t_1-^{1}H{X}-t_2] and direct [^{1}H-t_1-X{^{1}H}-t_2] schemes depends (among other factors) on the gamma ratio of ^{1}H and X nuclei as $(\gamma_H/\gamma_X)^{3/2}$, which for X = ^{13}C equals 8. These multidimensional techniques are similar to those developed in solutions, demonstrating the gradual convergence of solid-state and solution NMR.

However, in spite of the extraordinary surge in applications of these new SSNMR tools in chemistry, materials science, and biology, the studies of coals and other carbonaceous materials are still carried out using the protocols established in the 1980s [3-10]. Although several groups have since performed ^{13}C and ^{1}H NMR studies at higher fields (e.g. 9.4 T) and applied spectral editing techniques [22-25], to the best of our knowledge the "low-field" criteria for the quantitative ^{13}C NMR characterization of coals have not been critically challenged.

The objective of this study is to demonstrate that modern SSNMR methodology based on fast MAS at high magnetic field can enable quantitative structural studies of coals and other carbonaceous materials with good sensitivity, improved resolution, and in multiple dimensions. First, we explore the prospects offered by fast MAS ($\nu_R \geq 40$ kHz) at $B_0 = 11.7$ and 14.1 T for acquiring sideband-free ^{13}C CPMAS and DPMAS NMR spectra. The optimization and testing of these experiments is carried out on standard Argonne Premium Coal Samples [26] and a brown coal. Second, the sensitivities, line shapes and structural parameters of coals obtained at high magnetic field are compared with those measured under low-field condition ($B_0 = 4.7$ T and $\nu_R = 8$ kHz) and with the existing literature data [4-10]. Finally, the 2D ^{1}H-^{13}C HETCOR spectra of Argonne Premium Coals are obtained using indirect detection and fast MAS.

2. Experimental Section

2.1 Coals

Argonne Premium Coal Samples were obtained from the Premium Coal Sample Program at Argonne National Laboratory [26]. The samples, size -100 mesh, used in this study include: Wyodak-Anderson (WYO), Illinois #6 (ILL), Pocahontas #3 (POC), Blind

Canyon (BCS), and North Dakota Beulah-Zap (NDBZ). Brown coal (Peres-oben) from the upper part of the former Peres Mine (now Schleenhain Mine) in the former East Germany (Lippendorf, Saxony) was obtained from Professor D. Michel.

2.2 NMR Measurements

The 14.1 T studies were carried out at Ames Laboratory using a Varian NMR System 600 MHz spectrometer equipped with a 1.6-mm FastMAS™ triple resonance probe. The 11.7 T 1D ^{13}C CPMAS studies were carried out at ExxonMobil Research and Engineering using a Varian 500 MHz *InfinityPlus*® spectrometer equipped with a similar 1.6-mm FastMAS™ triple resonance probe. Experiments performed at high field include 1D ^{13}C CPMAS, 1D ^{13}C DPMAS and 2D ^{1}H-^{13}C HETCOR, both indirectly and directly detected. The indirectly detected experiment followed the earlier reported ^{13}C{^{1}H}-t_1-^{1}H{^{13}C}-t_2 scheme [15,21], using a tangentially ramped ^{1}H CP pulse to transfer magnetization to ^{13}C and tangentially ramped ^{13}C CP pulse or INEPT to transfer polarization back to ^{1}H. SPINAL-64 heteronuclear decoupling was used during evolution (t_1) or detection (t_2) periods and in 1D experiments, as appropriate [27]. The relaxation losses during the INEPT transfer were minimized by using phase modulated Lee-Goldburg (PMLG) homonuclear ^{1}H-^{1}H decoupling [16,19,28]. PMLG decoupling was also used during the evolution period in the directly detected [^{1}H-t_1-^{13}C{^{1}H}-t_2] HETCOR experiment. Low-field ^{13}C CPMAS spectra were obtained at ExxonMobil Research and Engineering using a Chemagnetics 200 MHz spectrometer (4.7 T) equipped with a 5-mm double resonance probe.

The experimental parameters are shown in figure captions using the following notation: ν_R denotes the MAS rate, τ_{CP} the mixing time during CP, $\nu_{RF}(^{1}H)$ and $\nu_{RF}(^{13}C)$

the magnitudes of RF magnetic fields at ^{1}H and ^{13}C frequencies, τ_{RR} the rotary resonance recoupling time, τ_{PMLG} the pulse length for PMLG decoupling, τ_1 the INEPT delay for creation of antiphase magnetization, τ_2 the INEPT delay used to refocus the magnetization, Δt_1 the increment of t_1 during 2D acquisition, τ_{RD} the recycle delay, NS the number of scans, and AT the total acquisition time. A Lorentzian line broadening of 150 Hz of was applied during processing of all spectra. The ^{1}H and ^{13}C NMR chemical shifts are externally referenced to TMS at δ_C and δ_H = 0 ppm.

3. Results and Discussion

3.1 Sensitivity, Resolution, and CP Efficiency under Fast MAS

To compare ^{13}C CPMAS sensitivity and resolution, spectra of Argonne Premium Coals were obtained at MAS rates of ν_R = 8 kHz at 4.7 T, ν_R = 41.7 kHz at 14.1 T (Figure 1) and ν_R = 40 kHz at 11.7 T (Figure 2). The remaining experimental parameters were optimized to maximize the sensitivity at each field.

An evaluation of the average signal to noise ratio (S/N) in the spectra in Figure 1 and 2 reveals that at 4.7 T the S/N is higher only by a factor of 1.5 - 2 per scan compared to 14.1 T and 11.7 T. In spite of the sample amount being almost 20 times larger (150 mg versus 8 mg) in the 5-mm rotor, this intensity ratio is not unexpected. Indeed, at a constant magnetic field, the relative sensitivities measured for sideband-free DPMAS spectra in 5-mm and 1.6-mm Varian rotors are approximately 4.5 : 1. As noted above, the ^{13}C spectra of coals are inhomogeneously broadened, thus the sensitivity is expected to increase linearly with B_0. Since the B_0 values used in our experiments differ by a factor of 3 (14.1 T) and 2.5 (11.7 T), we should expect sensitivity ratios of (4.5/3) : 1 ≅ 1.5 : 1 and (4.5/2.5): 1 ≅ 1.8 : 1. This is very close to what has been observed in our CPMAS

spectra, which further suggests that the efficiency of cross-polarization was not diminished under the conditions used in our fast MAS experiments (more on this, see below).

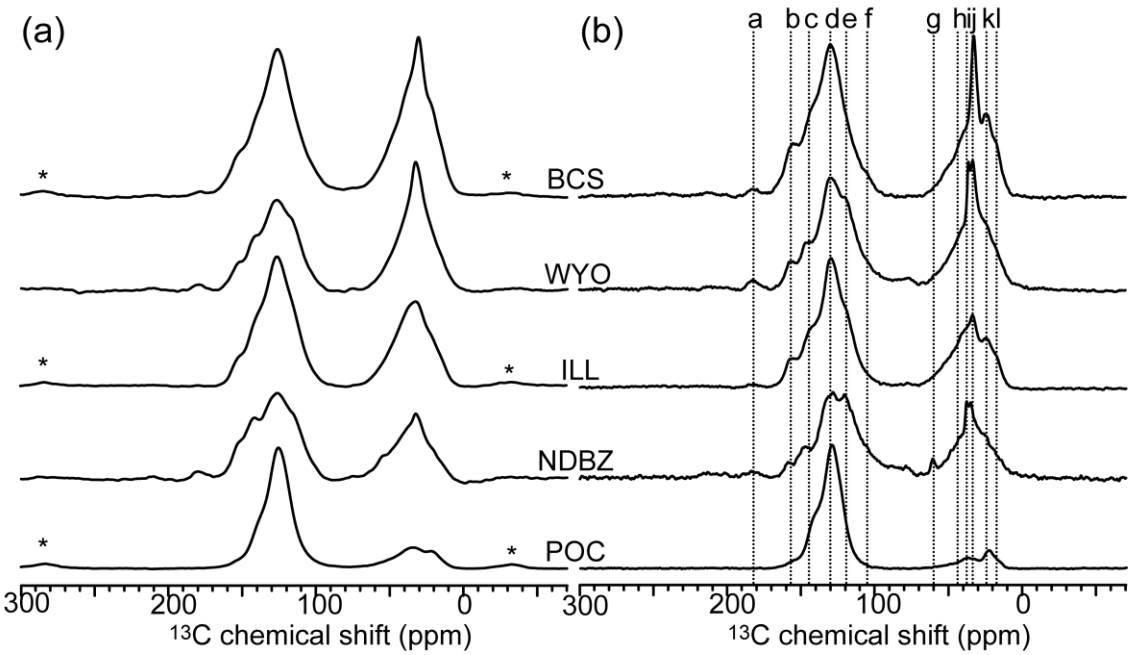

Figure 1. ^{13}C CPMAS spectra of Argonne Premium Coals obtained at 4.7 T (a), and 14.1 T (b). Other experimental parameters were as follows: (a) ν_R = 8 kHz, τ_{CP} = 2 ms, $\nu_{RF}(^1H)$ = 71.4 kHz during CP and 71.4 kHz during heteronuclear decoupling, $\nu_{RF}(^{13}C)$ = 71.4 kHz during CP, τ_{RD} = 2 s, NS = 14400, and AT = 8 h; (b) ν_R = 41.7 kHz, τ_{CP} = 2 ms, $\nu_{RF}(^1H)$ = 58 kHz during CP and 11 kHz during heteronuclear decoupling, $\nu_{RF}(^{13}C)$ = 100 kHz during CP, τ_{RD} = 1 s (which sufficed for full relaxation of magnetization), NS = 28800, and AT = 8 h. The dashed lines represent resolved peaks denoted as explained in the paper and the stars (*) represent the spinning sidebands.

In spite of the sensitivity penalty, the high field/fast MAS spectra offer numerous advantages, as already noted. For example, the 14.1 T spectra in Figure 1b and 11.7 T spectra in Figure 2a are better resolved within both aromatic and aliphatic regions as compared to the low-field spectra in Figure 1a, which shows that the line broadening is not purely inhomogeneous. The shoulders at δ_C = ~15-25 ppm (due to methyl groups, labeled 'k' and 'l' in Figure 1b) are easier to separate from the backbone methylene resonances (lines 'i','j') at δ_C = ~35 ppm and aliphatic carbons bonded to oxygen at δ_C = ~50-90ppm (lines 'f' 'g') in the 14.1 T spectra. Similarly the bands centered at δ_C = ~182 ('a'), 157 ('b'), 146 ('c'), 130 ('d'), and 120 ('e') ppm, nominally associated with carboxyl, phenolic, alkyl substituted aromatic, non-protonated aromatics, and protonated aromatics (including bridgehead) structural groups [9], respectively, are more clearly resolved at 11.7 and 14.1 T. The increased resolution of these individual resonances at higher field under fast MAS allows for better recognition of specific functional groups in coal spectra and can lead to a more accurate measure of average structural parameters. We also note that the lineshape observed for the low rank coal (Wyodak-Anderson) is visibly changed at various fields. At least two factors can contribute to the observed differences. First, the spectra of this coal shown in Figure 1 were acquired with τ_{CP} = 2 ms, whereas one taken at 11.7 T (Figure 2a) corresponds to τ_{CP} = 2.5 ms, which favors the aromatic intensity. The differences may be also due to the level of oxygen and moisture exposure in the studied samples. The coals were not packed in an air free environment, thus the degree of contamination may vary depending on the time of exposure to ambient atmosphere. Paramagnetic oxygen and moisture are known to decrease proton relaxation times T_1 and $T_{1\rho}$, which can result in distortions of CPMAS

spectra [8,29]. This effect increases with decreasing coal rank, and thus should be most pronounced for the Wyodak-Anderson coal. The sensitivity and resolution will be discussed later in the context of 2D spectra.

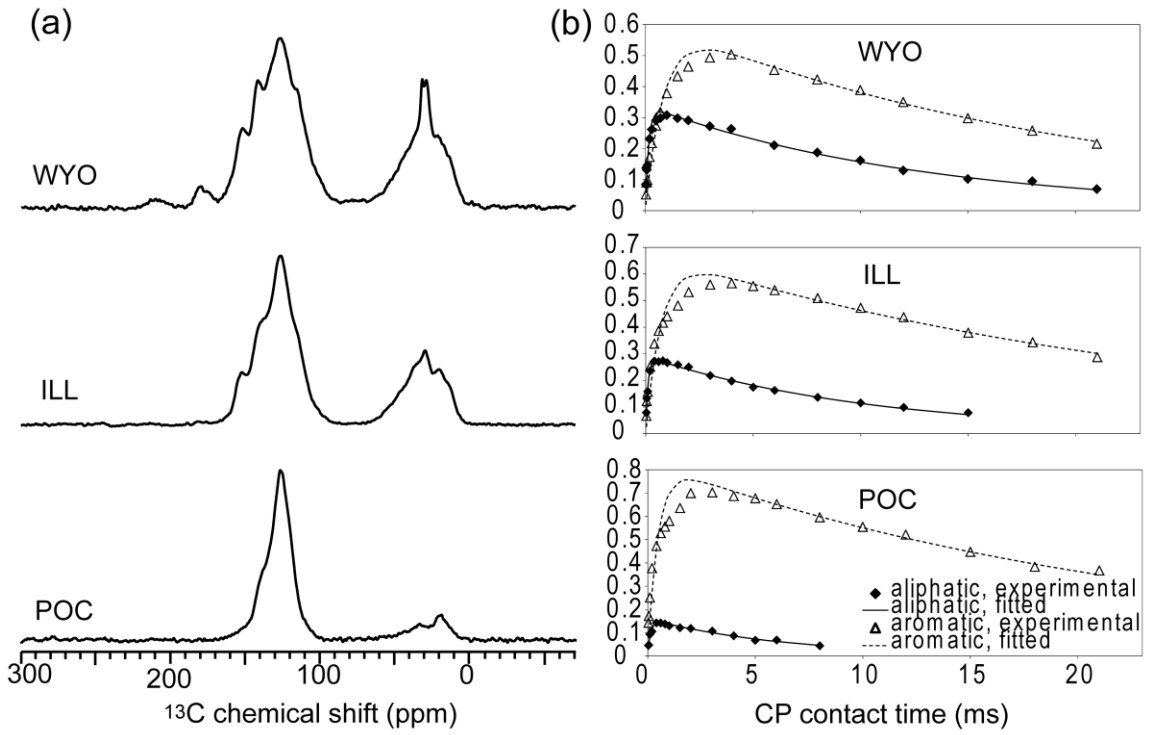

Figure 2. ^{13}C CPMAS spectra of Argonne Premium Coals obtained at 11.7 T (a) and normalized VCT experimental intensities and curves of best fit to Equation 1 (b). Other experimental parameters were as follows: ν_R = 40 kHz, $\nu_{RF}(^1H)$ = 60 kHz during CP and 10 kHz during heteronuclear decoupling, $\nu_{RF}(^{13}C)$ = 100 kHz during CP, τ_{RD} = 1 s. In (a), τ_{CP} = 2.5 ms, NS = 24000, 12000, and 8000, and AT = 6.8, 3.4, and 2.3 h for Wyodak-Anderson, Illinois #6 and Pocahontas #3 coals, respectively. In (b), 20 different τ_{CP} ranging from 0.3 to 21 ms were used for each sample. For aliphatic carbons long τ_{CP} data was excluded due to low sensitivity.

To address concerns about the efficiency of the CP process under fast MAS, we measured the so-called Hartmann-Hahn [30] matching curve for aliphatic and aromatic bands of Illinois #6 coal (Figure 3). The measurement was carried out at 40 kHz MAS using a tangentially ramped ^{1}H RF field with average strength $\nu_{RF}(^{1}H) = 95$ kHz, while varying the $\nu_{RF}(^{13}C)$ value of rectangular ^{13}C pulse between 20 and 180 kHz. Meier and co-workers recently described an efficient low-power approach to CP under fast MAS at $n = 0$ Hartmann-Hahn matching condition ($| \nu_{RF}(^{1}H) - \nu_{RF}(^{13}C) | = n\nu_R$, with $n = 0$), which utilizes the second-order cross terms between homo- and heteronuclear dipolar couplings [31]. The use of low RF power (e.g., $\nu_{RF}(^{1}H) = \nu_{RF}(^{13}C) \approx 10$ kHz), can be particularly useful in temperature-sensitive samples. However, the heteronuclear polarization transfer under such conditions is very sensitive to the resonance offset (band selective). In addition, such a CP mechanism is ineffective in the absence of ^{1}H-^{1}H dipolar interactions, where only the *J*-coupling mediated polarization transfer is possible [31]. Under the high-power conditions used here, it is important to avoid the undesired recoupling conditions $\nu_{RF}(^{1}H)/\nu_R = k$, which can accelerate the decay of spin-locked ^{1}H magnetization. At $k = ½$ (the so-called HORROR condition) the recoupling involves the ^{1}H-^{1}H homonuclear dipolar interactions, but at $k = 1$ it also includes the heteronuclear dipolar couplings and ^{1}H CSA. At $k = 2$ only the last two interactions are recoupled, while the higher order effects can be expected at $k = 1/4$, 1/3 and 3/2 [31-32]. By using $\nu_{RF}(^{1}H) = 95$ kHz and $\nu_R = 40$ kHz MAS we should have avoided these complications.

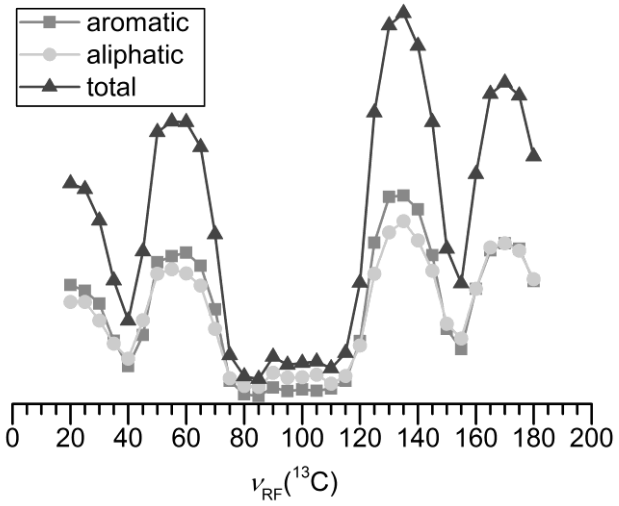

Figure 3. The Hartmann-Hahn matching curves measured for Illinois #6 coal at B_0 = 14.1 T, using ν_R = 40 kHz and tangentially ramped ^{1}H CP pulse centered at $\nu_{RF}(^1H) \cong 95$ kHz.

As expected[33-34], the most effective Hartmann-Hahn matches in Figure 3 can be seen at $n = \pm 1$ and ± 2. Although the observed sidebands are narrower than those measured for coals at 2.35 T [35], the CP process at 40 kHz MAS remains quite robust. Indeed, a deviation of ±2 kHz from the 'exact' Hartmann-Hahn match does not result in measurable drop of the CP efficiency. Furthermore, the matching patterns are very similar for both the aliphatic and aromatic regions of the spectrum.

3.2 Quantification.

Quantification of the aromatic region in coals is very important to determine coal's age, rank and caloric value [36]. Reliability of quantification of chemical functionalities in coals and similar carbonaceous materials has been largely debated since the first publication in the area [4-10]. Herein, carbon aromaticity, f_a, was measured

under fast MAS (ν_R = 40 kHz) at 11.7 T for selected coals (Wyodak-Anderson, Illinois #6 and Pocahontas #3) by measuring the CPMAS spectra with variable contact time τ_{CP} (VCT), following the previously described procedure [9]. The areas $M(\tau_{CP})^i$ (where i = AL, AR for aliphatic or aromatic, respectively) of the aliphatic (down-frequency from 90 ppm) and aromatic (up-frequency from 90 ppm) regions were calculated as a function of τ_{CP} for each coal to determine the initial magnetizations M_0^i, relaxation time constants ($T_{1\rho}^i$) and cross-polarization time constants (T_{CH}^i), using the formula[2]

$$M(\tau_{CP})^i = M_0^i e^{-\tau_{CP}/T_{1\rho}^i}[1 - e^{(1-T_{CH}^i/T_{1\rho}^i)(-\tau_{CP}/T_{1\rho}^i)}]. \quad (1)$$

The aromaticity, f_a, can be determined as

$$f_a = M_0^{AR}/(M_0^{AL} + M_0^{AR}). \quad (2)$$

The f_a values measured in this study using the VCT method (Figure 2) are compared in Table 1 with those obtained earlier by several research groups at 2.35 T. The agreement between our results and those previously obtained is excellent. The relaxation time constants ($T_{1\rho}$) and cross-polarization time constants (T_{CH}) for the aliphatic and aromatic carbons are summarized in Table 2. These data represent only the average T_{CH}^i and $T_{1\rho}^i$ values measured for aliphatic and aromatic bands. It is well known that wide distributions of relaxation parameters exist in coals due to heterogeneity of chemical environments, differences in mobility of various structural motifs and the presence of paramagnetic centers. Even the average values depend on the sample treatment and experimental conditions used during the measurements (e.g., compare data in rows 3 and 4 of Table 1) [6,8,10].

Table 1. Aromaticity Values for Argonne Premium Coals

Method of f_a Measurement (reference)	Wyodak-Anderson	Blind Canyon	Beulah-Zap	Illinois #6	Pocahontas #3
VCT-11.7 T (this study)[a]	0.66	NA	NA	0.71	0.84
VCT-2.35 T (ref. [7])[b]	0.63	0.63	0.67	0.72	0.86
VCT-2.35 T (ref. [8])[c]	0.65	0.64	0.66	0.70	0.83
VCT-2.35 T (ref. [8])[d]	0.60	0.63	0.58	0.70	0.86
VCT-2.35 T (ref. [9])[e]	0.63	0.65	0.61	0.72	0.86
VCT-2.35 T (ref. [10])[f]	0.65	NA	0.70	0.72	0.86
2ms-4.7 T (this study)	0.51	0.55	0.62	0.60	0.83
2ms-14.1 T (this study)	0.59	0.62	0.58	0.67	0.86
3ms-2.35 T (ref. [10])	0.64	NA	0.68	0.72	0.85
DPMAS-14.1 T (this study)	NA	0.72	NA	0.75	0.88
DPMAS-2.35 T (ref. [10])	0.66	NA	0.74	0.72	0.89
DPMAS-2.35 T (ref. [7])	0.75	0.67	0.76	0.75	0.90

Sample treatment: [a] packed into MAS rotors in the laboratory directly from the vials in which the coals were shipped, spun under dry air; [b] vacuum dried before packing; [c] as-received, packed under He atmosphere, spun in sealed glass NMR tubes; [d] air dried after exposure to ambient conditions for several months, spun in air-tight rotors; [e] packed and spun under dry nitrogen in air-tight rotors, [f] dried under vacuum at 80 °C, spun in air-tight rotors.

Table 2. Average $\boldsymbol{T_{CH}^{i}}$ and $\boldsymbol{T_{1\rho}^{i}}$ Values Measured for Argonne Premium Coals

Coal (11.7 T)	T_{CH}^{AL} (ms)	$T_{1\rho}^{AL}$ (ms)	T_{CH}^{AR} (ms)[a]	$T_{1\rho}^{AR}$ (ms)[a]
Wyodak-Anderson	0.15	13.0	0.85	20.5
Illinois #6	0.10	10.7	0.73	24.0
Pocahontas #3	0.13	6.3	0.48	23.7

[a] To obtain the most accurate values of aromaticities, we followed the procedure described by Smernik et al.[37] $T_{1\rho}^{AR}$ was determined by fitting the selected τ_{CP} range (4 – 21 ms) to a simple exponential decay; T_{CH}^{AR} was obtained by a full fit to Equation 1 while keeping $T_{1\rho}^{AR}$ fixed.

Also shown in Table 1 are the aromaticities evaluated by using the M_0^i values obtained for a single contact time τ_{CP} = 2 ms (i.e., from the spectra in Figure 1) and at τ_{CP}

= 3 ms by Muntean and Stock [10]. Here, the discrepancy between various data sets is more significant, as expected, especially for low rank coals.

In principle, DPMAS spectra (Figure 4) should give the most accurate aromaticity value of coals since there is no bias associated with ^{1}H proximity. Although direct-polarization is not the preferred method for excitation due to long recycle delays and low sensitivity per scan, the aromaticity values from the present study show very good agreement with the existing data obtained at low fields (Table 1) [7-10].

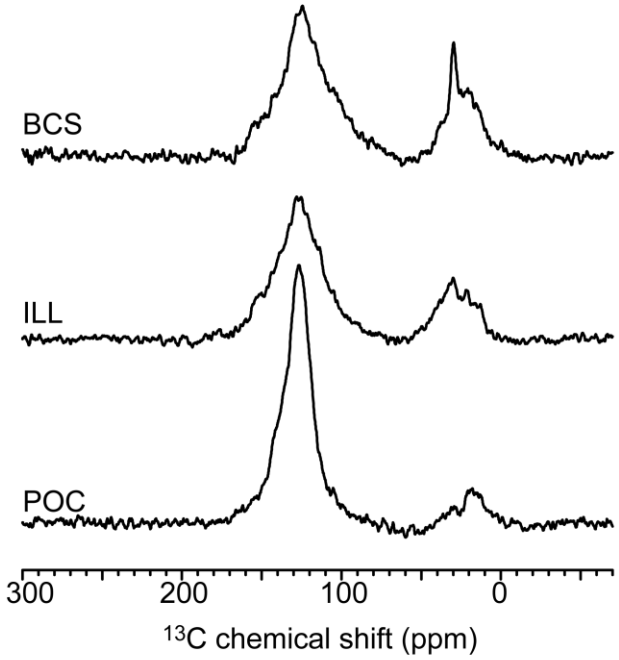

Figure 4. ^{13}C DPMAS spectra of Blind Canyon, Illinois #6 and Pocahontas #3 coals acquired at 14.1 T with ν_R = 40 kHz, $\nu_{RF}(^{13}C)$ = 100 kHz, $\nu_{RF}(^{1}H)$ = 10 kHz during heteronuclear decoupling, τ_{RD} = 60 s, NS = 1000, 1600 and 1000, and AT = 17 h, 27 h and 17 h, respectively.

These data suggest that quantitative structural studies of complex carbonaceous materials are indeed possible under fast MAS at high magnetic field with the same level

of confidence as those studies done with much slower MAS at much lower magnetic fields. The higher resolution obtained at fast MAS, combined with the use of relaxation time constants ($T_{1\rho}$) and cross-polarization time constants (T_{CH}) for the aliphatic and aromatic carbons determined from the VCT CPMAS experiments, facilitate a semi-quantitative comparison of the spectra in Figure 1. For example, the methyl and methylene contents (lines 'l', 'k', 'j', and 'i') of these coals systematically decrease as the rank increases. Similarly, the amount of heteroatom substituted species (lines 'a', 'b', and 'g') decrease with maturity and the substituted aromatics (line 'c') increase with maturity. The relative intensities of these spectral features can be used to calculate many of the structural parameters described by Solum *et al*. [9] Again, the structural parameters from the present study (Table 3) show good agreement with those reported earlier for the same coals at lower magnetic fields [7-10].

Table 3. Structural Parameters for Argonne Premium Coals from Solid-State ^{13}C NMR Measurements at 11.7 T under 40 kHz MAS

	Structural parameters[a]						
Coal (11.7 T)	f_a	f_{al}	f_a^C	$f_{a'}$	f_a^P	f_a^S	f_{al}^0
Wyodak-Anderson	0.66	0.34	0.04	0.62	0.07	0.16	0.05
Illinois #6	0.71	0.29	0.01	0.71	0.06	0.18	0.03
Pocahontas #3	0.84	0.16	0.00	0.84	0.03	0.17	0.01

[a] The structural parameters are defined as in reference 9: f_a is given by Equation (1); f_{al} represents fraction of aliphatic carbons, $f_{al} = 1 - f_a$; f_a^C – carbonyl carbons ($\delta_C > 165$ ppm); $f_{a'}$ – carbons in the aromatic rings, $f_{a'} = f_a - f_a^C$; f_a^P – phenoxyl/phenolic functionalities (δ_C = 150-165 ppm); f_a^S – alkyl-substituted aromatic carbons (δ_C = 135-150 ppm); and f_{al}^O – aliphatic carbons bonded to oxygen (δ_C = 50-90 ppm).

However, the estimation of aromatic cluster size from ^{13}C NMR spectra requires a measure of the bridgehead carbons. The accepted low-field protocol uses a combination of a dipolar dephasing experiment [38], which allows for the distinction of protonated (f_a^H) and nonprotonated (f_a^N) aromatic carbons, with integrals obtained from selected chemical shift ranges. For example, the amount of bridgehead carbons (f_a^B) is quantified as $f_a^B = f_a^N - f_a^P - f_a^S$, where f_a^P = phenoxyl/phenolic (δ_C = 165-150 ppm) and f_a^S = alkyl-substituted aromatic carbons (δ_C = 150-135 ppm). A requirement of this experiment [38], namely that the dephasing time (typically in the 50-100 μs range) be much shorter than one rotor period to avoid rotational recoupling, can be easily met under the lower ν_R rates used at low B_0. However, under fast MAS conditions (ν_R = 40 kHz) the 25 μs rotor period is too short to effectively apply dipolar dephasing. Thus, alternate spectral editing techniques for the distinction of protonated and nonprotonated carbons need to be applied or developed for fast MAS conditions [39]. An alternate spectral editing technique for the evaluation of the fraction of aromatic carbon in bridgehead positions under fast MAS conditions, and its use to evaluate the average cluster size in Argonne Premium Coals are described in two separate studies [40-41].

3.3 Two-Dimensional Analysis.

Although NMR studies of coals and other carbonaceous materials have been mostly carried out using 1D ^{13}C and ^{1}H techniques, several studies utilizing 2D HETCOR measurements were also reported. The main challenge in these experiments lies in overcoming the ^{1}H-^{1}H homonuclear dipolar interactions, such that the carbon functionalities dispersed along the ^{13}C dimension can be associated with recognizable aliphatic and aromatic ^{1}H species. Zilm and Webb reported the first $^{13}C\{^{1}H\}$ HETCOR

spectrum of a coal (Illinois #6) at 2.35 T using the ^{1}H-t_1-^{13}C{^{1}H}-t_2 scheme with MREV-8 homonuclear (CRAMPS) decoupling during t_1 [13]. The same general scheme was applied by Wilson *et al*. to study a series coals from Australia and North America at relatively high field (9.4 T), except that they used BLEW-12 sequence for ^{1}H-^{1}H decoupling during t_1, the windowless WIM-24 ^{13}C{^{1}H} cross-polarization scheme and the TOSS sequence for the removal of spinning sidebands [24]. A very similar pulse sequence was used by Bronnimann *et al*., who recorded a 2D ^{13}C{^{1}H} HETCOR spectrum of Beulah-Zap coal at 4.4 T [12]. Recently, Mao *et al*. published an extensive study of structural features of a bituminous coal using a series of advanced solid-state NMR measurements, including 2D HETCOR at 9.4 T [25]. These studies clearly demonstrated the potential of 2D HETCOR techniques for structural analysis of coals and related materials.

As already explained in the introduction, the advent of fast MAS enabled the implementation of indirect detection of insensitive nuclei in solids via protons. Indeed, we recently reported the first such spectra of a coal, including the HSQC-type measurement of correlations mediated through chemical bonds via *J*-couplings, which were generated using the refocused INEPT sequence [16]. The indirectly detected through-space spectrum of Beulah-Zap coal is shown in Figure 5. In spite of the small sample size, we were able to acquire the ^{1}H-detected 2D spectrum of this sample in one day. Beulah-Zap is a lignite, low rank coal, which is made apparent by the presence of strong aliphatic resonances in both the ^{1}H and ^{13}C dimensions. The resolution in the ^{1}H dimension appears to be better than previously obtained for the same coal at a lower field [12], which suggests that incomplete removal of homonuclear dipolar interactions at ν_R =

41.7 kHz does not influence the resolution in coals due to strong inhomogeneous contribution to line broadening.

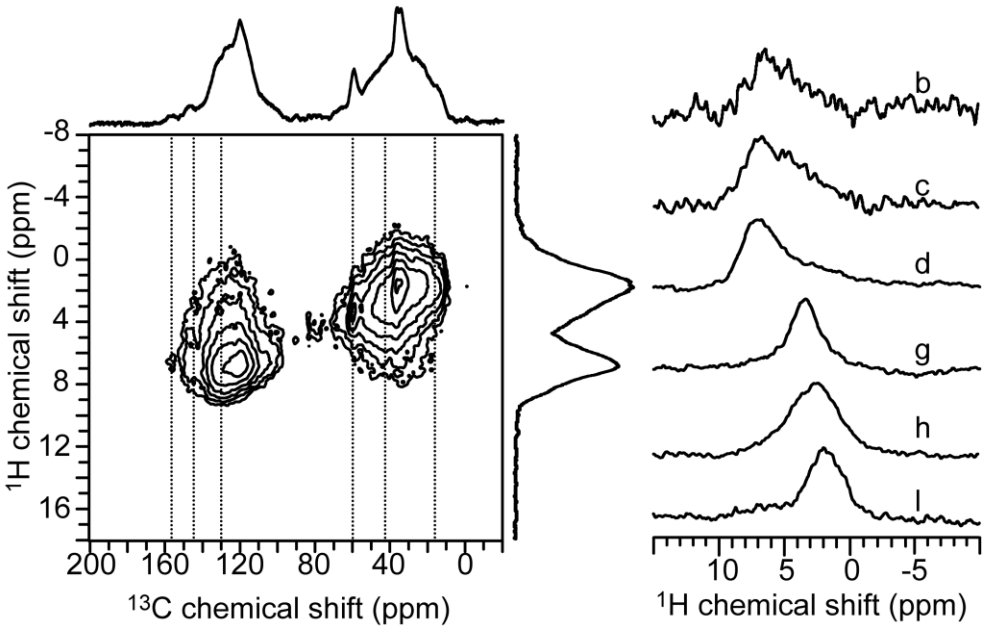

Figure 5. 2D indirectly detected $^1H\{^{13}C\}$ through-space spectrum of Beulah-Zap acquired using the following parameters: ν_R = 41.7 kHz, τ_{CP} = 0.5 ms, $\nu_{RF}(^1H)$ = 60 kHz during CP and 12 kHz during heteronuclear decoupling, $\nu_{RF}(^{13}C)$ = 102 kHz during CP and 10 kHz during heteronuclear decoupling, τ_{RR} = 24 ms, Δt_1 = 24 μs, τ_{RD} = 1 s, NS = 400, and AT = 23.5 h. Cross sections in the ^{1}H dimension were taken at points correlating to the dashed lines in Figure 1 and are labeled accordingly.

A pair of through-space and through-bond 2D HETCOR spectra of a brown coal (Peres-oben) is shown in Figure 6. This coal is also classified as a lignite and exhibits a wide variety of functional group correlations. Examination of the cross sections in these spectra allows for better recognition of the functional groups and, in the case of CP-based spectra, the spatial proximities between different functionalities. For instance, it is clear

in Figure 6a that the aliphatic hydrogen at 2 ppm is also close to the aromatic and carboxyl carbons in this coal. Intensities of ^{1}H-^{13}C correlations measured as a function of τ_{CP} can be used to obtain more detailed insights. Such correlations are clearly missing in the INEPT-based spectrum, which reveals only the connectivities through a single C-H bond. In addition, the polarization transfer via INEPT is less efficient than CP. This is due to the decoherence of ^{13}C and ^{1}H transverse magnetizations during τ_1 and τ_2, respectively, which is slowed down, but not completely eliminated, by the combination of fast MAS and PMLG decoupling.

Finally, we examined the relative sensitivity and resolution offered by the indirect detection scheme versus the ^{13}C-detected measurements performed both with and without homonuclear ^{1}H-^{1}H decoupling during the evolution time t_1 (in this case using a non-supercycled PMLG5 sequence) [16]. The spectra of Blind Canyon coal shown in Figure 7a and b demonstrate the benefits of using the indirect detection: the sensitivity ratio per scan in $^{1}H\{^{13}C\}$ and $^{13}C\{^{1}H\}$ spectra exceeds 3 : 1, which translates to experimental time saving of roughly 10. The spectra in Figures 7b and c further demonstrate that under MAS at 41.7 kHz the use of PMLG decoupling has no measurable effect on ^{1}H resolution in coals (note that the signal-to-noise ratio in Figure 7c is lower due to shorter experimental time; the sensitivity per scan is very similar to Figure 7b).

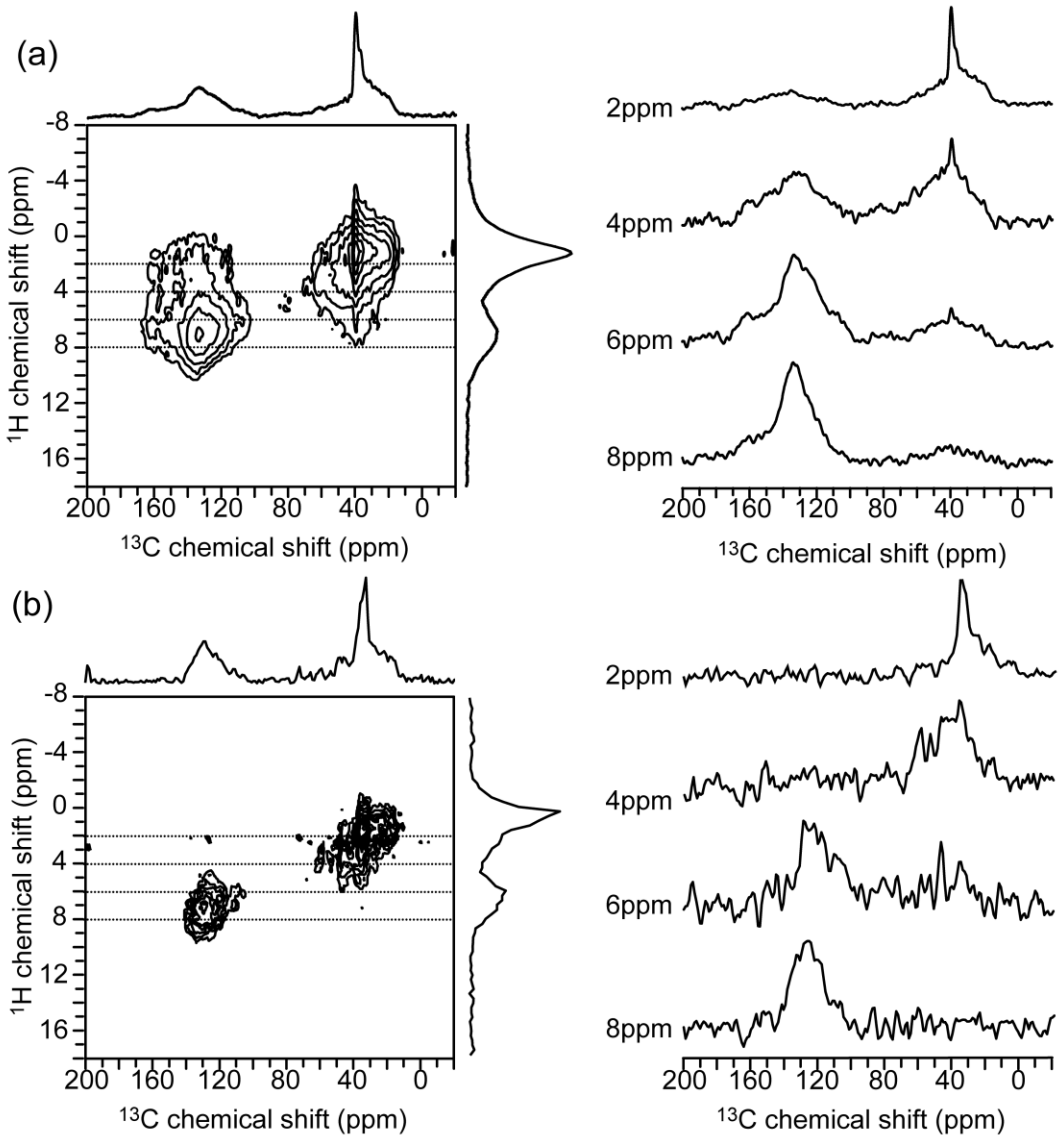

Figure 6. 2D indirectly detected through-space (a) and through-bond (b) ^{1}H{^{13}C} spectra of brown coal. Spectrum (a) was acquired using the following parameters: ν_R = 41.7 kHz, τ_{CP} = 3 ms, $\nu_{RF}(^1H)$ = 68 kHz during CP and 12 kHz during heteronuclear decoupling, $\nu_{RF}(^{13}C)$ = 110 kHz during CP and 10 kHz during heteronuclear decoupling, τ_{RR} = 24 ms, Δt_1 = 24 μs, τ_{RD} = 1 s, NS = 400, and AT = 23 h. The same conditions were used to measure spectrum (b), where the delays during INEPT were $\tau_1 = \tau_2$ = 0.72 ms, NS = 1100, and AT = 68 h. ^{13}C cross sections are shown at δ_H = 2, 4, 6, and 8 ppm.

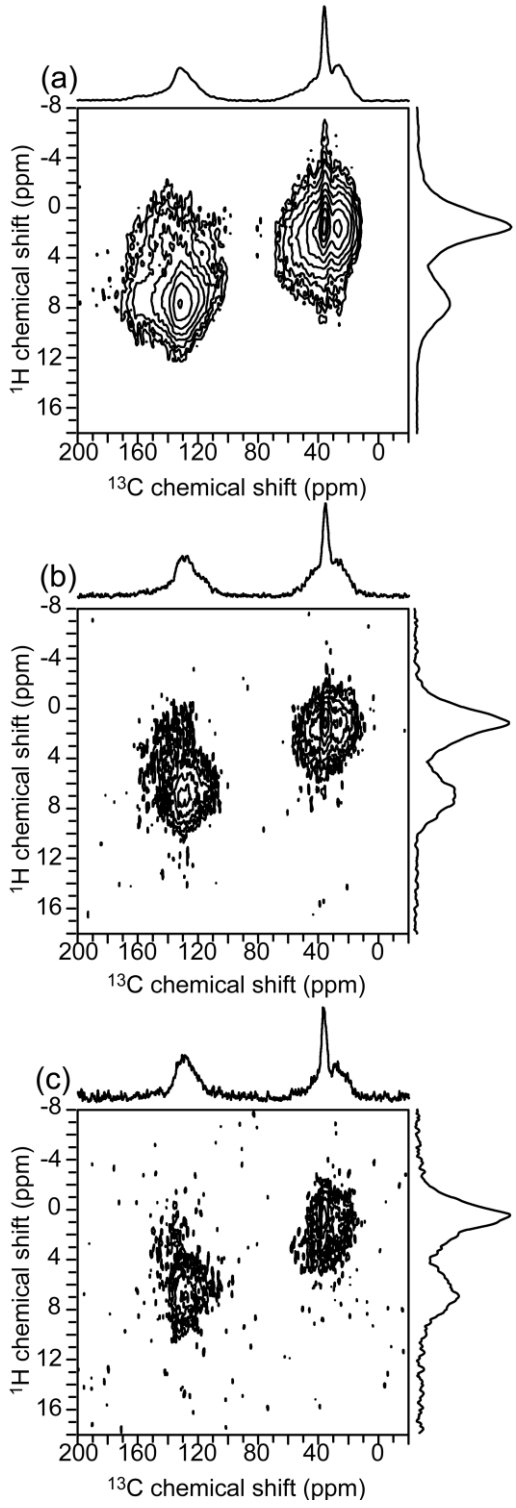

Figure 7. (a) 2D indirectly detected $^{1}H\{^{13}C\}$ spectrum of Blind Canyon coal acquired using the parameters given in caption to Figure 5. (b) 2D directly detected $^{13}C\{^{1}H\}$

spectrum of Blind Canyon coal acquired with homonuclear ^{1}H-^{1}H PMLG decoupling during t_1 using τ_{PMLG} = 15 μs, Δt_1 = 105 μs, NS = 256, and AT = 15 h. Other experimental parameters are given in caption to Figure 5. (c) The same ^{13}C{^{1}H} spectrum acquired without homonuclear ^{1}H-^{1}H PMLG decoupling (NS = 96 and AT = 4.5 h).

4. Conclusions

Through the use of recent advancements in SSNMR, such as fast MAS and indirect detection, coals can be studied at higher fields than previously believed practical. This allows for sensitive and quantitative study of coal aromaticity and structure, despite the inherently broad linewidth. These advances also enable the detection of 2D coal spectra in a timely manner. Examination of ^{1}H-^{13}C correlations can provide valuable information about the functional groups of coals, as well as the overall structure.

The sensitivity of 1D and 2D experiments is only marginally lower than that of traditional low field/slow MAS methods, because better S/N per spin and the use of ^{1}H detection compensate for most of the signal loss due to the small rotor size. Further improvements can be expected at even higher magnetic fields. In several respects, the proposed experiments are easier to implement and optimize. For example, the use of fast MAS eliminates the need for using CRAMPS in coals. Similarly, there is no necessity for suppression of the spinning sidebands, which improves the quantitative reliability of spectral intensities. Additional mixing protocols, such as INEPT, can be implemented to distinguish through-bond correlations from interactions through-space. The use of indirect detection can also be considered in coal research for the study of other insensitive nuclei, such as ^{15}N. Traditional methods to determine structural parameters in coals,

especially for distinguishing bridgehead carbons, are revisited in the context of high-field studies in separate publications [40-41].

5. Acknowledgment

At the Ames Laboratory, this research was supported by the U.S. Department of Energy, Office of Basic Energy Sciences, Division of Chemical Sciences, Geosciences, and Biosciences. The Ames Laboratory is operated for the U.S. Department of Energy by Iowa State University under Contract No. DE-AC02-07CH11358. The authors thank Dr. J. W. Wiench, Dr. T. Kobayashi, and Mr. D. Griffin for experimental assistance and Dr. S. R. Kelemen and Professor D. Michel for providing the Argonne Premium and brown coal samples, respectively. The continued support of ExxonMobil Research and Engineering, in particular Dr. P. A. Stevens, Dr. S. P. Rucker and Dr. T. Barckholtz, are gratefully acknowledged.

6. References

[1] Basic Research Energy Needs: Catalysis for Energy, the U.S. Department of Energy Basic Energy Sciences Workshop, 2007.

[2] M. Mehring, Principles of High Resolution Nmr in Solids, Springer-Verlag, New York, 1983.

[3] C.A. Fyfe, Solid State Nmr for Chemists, C.F.C. Press, Guelph, Canada, 1984.

[4] H.L. Retcofsky, and R.A. Friedel, Anal. Chem. 43 (1971) 485-487.

[5] M.J. Sullivan, and G.E. Maciel, Anal. Chem. 54 (1982) 1606-1615.

[6] C.E. Snape, D.E. Axelson, R.E. Botto, J.J. Delpuech, P. Tekely, B.C. Gerstein, M. Pruski, G.E. Maciel, and M.A. Wilson, Fuel 68 (1989) 547-60.

[7] J.A. Franz, R. Garcia, J.C. Linehan, G.D. Love, and C.E. Snape, Energy Fuels 6 (1992) 598-602.

[8] L. dela Rosa, M. Pruski, D. Lang, B. Gerstein, and P. Solomon, Energy Fuels 6 (1992) 460-8.

[9] M.S. Solum, R.J. Pugmire, and D.M. Grant, Energy Fuels 3 (1989) 187-193.

[10] J.V. Muntean, and L.M. Stock, Energy Fuels 5 (1991) 765-767.

[11] D.E. Axelson, Solid State Nuclear Magnetic Resonance of Fossil Fuels Multiscience, Montreal, Canada, 1985.

[12] C.E. Bronnimann, C.F. Ridenour, D.R. Kinney, and G.E. Maciel, J. Magn. Reson. 97 (1992) 522-534.

[13] K.W. Zilm, and G.G. Webb, Fuel 65 (1986) 721-724.

[14] A. Samoson, T. Tuherm, J. Past, A. Reinhold, T. Anupõld, and I. Heinmaa, Top. Curr. Chem. 246 (2005) 15-31.

[15] J.W. Wiench, C.E. Bronnimann, V.S.-Y. Lin, and M. Pruski, J. Am. Chem. Soc. 129 (2007) 12076-12077.

[16] K. Mao, and M. Pruski, J. Magn. Reson. 201 (2009) 165-74.

[17] M. Leskes, P.K. Madhu, and S. Vega, J. Magn. Reson. 199 (2009) 208-213.

[18] K. Mao, J.W. Wiench, V.S.-Y. Lin, and M. Pruski, J. Magn. Reson. 196 (2009) 92-95.

[19] B. Elena, A. Lesage, S. Steuernagel, A. Böckmann, and L. Emsley, J. Am. Chem. Soc. 127 (2005) 17296-17302.

[20] D.H. Zhou, G. Shah, C. Mullen, D. Sandoz, and C.M. Rienstra, Angew. Chem., Int. Ed. 48 (2009) 1253-1256.

[21] Y. Ishii, and R. Tycko, J. Am. Chem. Soc. 122 (2000) 1443-1455.

[22] X.L. Wu, S.T. Burns, and K.W. Zilm, J. Magn. Reson. 111 (1994) 29-36.

[23] J.Z. Hu, M.S. Solum, C.M.V. Taylor, R.J. Pugmire, and D.M. Grant, Energy Fuels 15 (2001) 14-22.

[24] M.A. Wilson, J.V. Hanna, K.B. Anderson, and R.E. Botto, Org. Geochem. 20 (1993) 985-999.

[25] J.-D. Mao, A. Schimmelmann, M. Mastalerz, P.G. Hatcher, and Y. Li, Energy Fuels 24 (2010) 2536-2544.

[26] K.S. Vorres, Energy Fuels 4 (1990) 420-426.

[27] B.M. Fung, A.K. Khitrin, and K. Ermolaev, J. Magn. Reson. 142 (2000) 97-101.

[28] E. Vinogradov, P.K. Madhu, and S. Vega, Chem. Phys. Lett. 329 (2000) 207-214.

[29] R.A. Wind, A. Jurkiewicz, and G.E. Maciel, Energy Fuels 68 (1989) 1189-1197.

[30] S.R. Hartmann, and E.L. Hahn, Phys. Rev. 128 (1962) 2042-2053.

[31] A. Lange, I. Scholz, T. Manolikas, M. Ernst, and B.H. Meier, Chem. Phys. Lett. 468 (2009) 100-105.

[32] I. Scholz, B.H. Meier, and M. Ernst, J. Chem. Phys. 127 (2007) 204504.

[33] E.O. Stejskal, J. Schaefer, and J.S. Waugh, J. Magn. Reson. 28 (1977) 105-112.

[34] F. Engelke, T. Kind, D. Michel, M. Pruski, and B.C. Gerstein, J. Magn. Reson. 95 (1991) 286-298.

[35] M. Pruski, L. dela Rosa, and B.C. Gerstein, Energy Fuels 4 (1990) 160-165.

[36] R. Gupta, Energy Fuels 21 (2007) 451-460.

[37] R.J. Smernik, and J.M. Oades, Geoderma 96 (2000) 101-129.

[38] S.J. Opella, and M.H. Frey, J. Am. Chem. Soc. 101 (1979) 5854-5856.

[39] J.-D. Mao, and K. Schmidt-Rohr, Environ. Sci. Technol. 38 (2004) 2680-2684.

[40] K. Mao, G.J. Kennedy, S.M. Althaus, and M. Pruski, Solid State Nucl. Magn. Reson. 47–48 (2012) 19-22.

[41] K. Mao, G.J. Kennedy, S.M. Althaus, and M. Pruski, Energy Fuels 27 (2013) 760-763.

CHAPTER 3: INDIRECTLY DETECTED HETERONUCLEAR CORRELATION SOLID-STATE NMR SPECTROSCOPY OF NATURALLY ABUNDANT ^{15}N NUCLEI

A paper published in *Solid State Nuclear Magnetic Resonance,* 57–58, 17-21 (2014).

Stacey M. Althaus[‡†], *Kanmi Mao*[‡†], *John A. Stringer*[§], *Takeshi Kobayashi*[†], *Marek Pruski*[‡†]

[‡] U.S. DOE Ames Laboratory, Ames, IA 50011-3020, USA

[†]Department of Chemistry, Iowa State University, Ames, IA 50011-3020, USA

[§]Agilent Technologies, 900 South Taft, Loveland, CO 80537, USA

Abstract

Two-dimensional indirectly detected through-space and through-bond ^{1}H{^{15}N} solid-state NMR experiments utilizing fast magic angle spinning (MAS) and homonuclear multipulse ^{1}H decoupling are evaluated. Remarkable efficiency of polarization transfer can be achieved at a MAS rate of 40 kHz by both cross-polarization and INEPT, which makes these methods applicable for routine characterizations of natural abundance solids. The first measurement of 2D ^{1}H{^{15}N} HETCOR spectrum of natural abundance surface species is also reported.

1. Introduction

Nitrogen is an important element for spectroscopists due to its ubiquitous presence in organic, catalytic, and biological compounds. Two NMR active isotopes of nitrogen, ^{14}N and ^{15}N, have potential for spectroscopic investigation; however, both have shortcomings and neither has become apparent as the predominant in solid-state (SS)NMR. Detection of ^{14}N, despite a high natural abundance of 99.6%, is challenging due to the integer spin ($I = 1$) and the resulting first order quadrupolar broadening (often in excess of 1 MHz), which is detrimental to both sensitivity and resolution. The quadrupolar parameters and chemical shift data can be determined from the analysis of static ^{14}N powder patterns or state-of-the-art magic angle spinning (MAS) spectra obtained under carefully controlled rotor orientation (to ~0.001°) and ultrastable spinning rate (to ~0.1Hz) [1-2]. The acquisition of high quality wideline ^{14}N spectra can be further assisted by the use of pulse sequences featuring broadband excitation, multiecho refocusing (using quadrupolar Carr-Purcell-Meiboom-Gill protocol, referred to as QCPMG [3]) and piecewise acquisition schemes [4-5]. Although such spectra can uniquely provide both electric field gradient and chemical shift tensor parameters, simulations become difficult for complex materials containing multiple nitrogen environments. Recently, two-dimensional (2D) heteronuclear (HETCOR) sequences have been developed wherein detection of the ^{14}N signal occurs indirectly via neighboring spin 1/2 nuclei (^{13}C [6-7] and ^{1}H [8-11]). These sequences have used precise magic angle setting and rotor synchronization during evolution time (t_1) to average the first order quadrupolar broadening to zero. ^{1}H detected ^{14}N 2D spectra can be collected with high sensitivity [8-9] despite the low efficiency of polarization transfer. The resulting ^{14}N

resonance frequencies depend upon isotropic chemical shifts, quadrupolar induced shifts, and anisotropic contributions due to scaled-down second-order quadrupolar interaction. Isotropic chemical shifts can be determined by separating both contributions, which becomes challenging for unknown compounds.

Notwithstanding the low natural abundance (0.4%), ^{15}N NMR has the advantage of providing direct access to chemical shift information without interference from quadrupolar effects. For the last three decades, 2D ^{1}H-^{15}N HETCOR NMR spectra in solution have been measured using the so-called indirect detection via the high-γ ^{1}H nuclei, primarily using heteronuclear single quantum coherence (HSQC) and heteronuclear multiple quantum coherence (HMQC) schemes, to overcome the sensitivity issues without isotope enrichment [12-14]. In solids however, such approaches were until recently impractical because of the inherently broad ^{1}H linewidth. Indeed, the first natural abundance ^{1}H-^{15}N solid-state spectra of medium-sized organic molecules (tripeptides) used a ^{15}N-detected MAS-*J*-HMQC scheme with frequency switched Lee Goldburg (FSLG) ^{1}H homonuclear decoupling [15]. The indirectly detected measurements were initially implemented by perdeuteration of peptides and proteins to enhance the resolution in the ^{1}H dimension under moderate MAS rates ($\nu_R \leq 30$ kHz) and used dipolar (through-space) cross-polarization (CP) during mixing. This led to sensitivity gain by a factor of 5 to 7 in the 2D and 3D ^{1}H{^{15}N} spectra of ^{15}N-enriched samples [16-19]. In similar experiments, coherent transfers of dipolar polarization have been implemented at $\nu_R = 30$ kHz utilizing the sequences of rotor-synchronized π pulses [20-21]. The REDOR-type recoupled polarization transfer (REPT) method has been used in the ^{1}H-^{15}N-^{1}H experiments on ^{15}N-enriched isocytosine derivatives [20]. Remarkably, a related

experiment with TEDOR-type magnetization transfer yielded 2D HETCOR spectra, as well as N-H bond length information, in natural abundance L-histidine [21].

The availability of ultrafast MAS, currently with frequencies of up to 110 kHz [22-25], and the resulting boost in ^{1}H resolution, facilitated further development of multidimensional correlation schemes. Studies have demonstrated that the small rotor volume (<10 μL) is largely offset by excellent sensitivity per spin and have highlighted other advantages of very fast MAS, including the flexibility in using RF power (e.g., high power for excitation and low power for heteronuclear decoupling) [26-27], reduced transverse T_2' relaxation [28-29], increased spectral width in rotor-synchronized experiments, and efficient cross-polarization [30-32]. Indeed, 2D HETCOR spectra of naturally abundant biomolecular solids were obtained using the HSQC-type ^{1}H-^{15}N-^{1}H experiments based on double-transfer CP-CP scheme, where MAS alone provided adequate resolution in ^{1}H dimension [33]. It has been further demonstrated that through-bond transfers originally developed for solutions can be exploited in these experiments to probe partially mobile surface-bound molecules in mesoporous organic-inorganic hybrid materials [29], where the X $\rightarrow$ ^{1}H step (in this case X = ^{13}C) utilized refocused INEPT (INEPTR). Fast MAS played a critical role during INEPTR by reducing the magnetization losses due to T_2' relaxation. This method was extended to fully rigid solids [34] by using ^{1}H-^{1}H homonuclear decoupling during INEPTR [35], which proved efficient under fast MAS [36].

It is somewhat surprising that despite these favorable results the measurements of correlation spectra involving natural abundance ^{15}N species have not become common practice. Herein, we demonstrate that the sensitivity enhancement achieved via indirect

detection made it possible, if not routine, to measure CP-based ^{15}N-^{1}H HETCOR spectra of several samples, including organically functionalized mesoporous silica. Additionally, we report the first 2D INEPT-based spectra of solids under natural ^{15}N abundance and compare the efficiencies of through-space and through-bond polarization transfers.

2. Experimental

2.1. Sample Preparation

Natural abundance samples of *N*-formyl-l-methionyl-l-leucyl-l-phenylalanine-OMe (MLF) and L-Histidine HCl H_2O were purchased from Fluka (Sigma-Aldrich). The corresponding ^{15}N-enriched sample of histidine was crystallized from aqueous solution at pH 4.5, which was adjusted by mixing appropriate volumes of 1M HCl and 1M NaOH, as described in reference [37]. 1,3,5 Trimethoxybenzene (TMOB) was purchased from Sigma-Alrich. The sample of 3-(3-phenylureido)propyl attached to the surface of mesoporous silica nanoparticles (PUP-MSN) was prepared by Dr. Hung-Ting Chen as described in an earlier paper [38]. Glycine with universally labeled ^{13}C and ^{15}N was purchased from Cambridge Isotope Laboratories (CIL).

2.2. NMR Measurements and Numerical Simulations

All experiments were performed at 14.1 T on a Varian 600-MHz NMR System spectrometer using a 1.6-mm FastMAS^{TM} T3 triple resonance probe operated at 599.6 MHz for ^{1}H, 150.8 MHz for ^{13}C, and 60.8 MHz for ^{15}N. The samples were packed in MAS zirconia rotors and spun at 40 kHz. The pulse sequences employed for 2D $^{1}H\{^{15}N\}$ with CP and INEPTR can be viewed in Fig. 1. These sequences utilize tangentially ramped $^{15}N\{^{1}H\}$ CP to generate initial ^{15}N magnetization, which evolves during t_1 under

low power SPINAL-64 [39] ^{1}H decoupling. The pulse following t_1 stores ^{15}N magnetization along the B_0 field; at the same time, the ^{1}H magnetization is eliminated using two long pulses with orthogonal phases and whose amplitudes satisfy the rotary resonance recoupling condition [40]. For the through-space sequence (Figure 1a), tangential CP is then used again to transfer ^{15}N magnetization back to ^{1}H, and the data is acquired in t_2 under ^{15}N SPINAL-64 decoupling. In the through-bond sequence (Figure 1b), the CP transfer is replaced with the INEPTR sequence of rotor-synchronized pulses to transfer magnetization back to ^{1}H nuclei. The PMLG$\bar{m}^{x}$ homonuclear ^{1}H-^{1}H decoupling sequence [41-42] is used during INEPTR transfer to prevent decoherence of ^{15}N and ^{1}H magnetizations during τ_1 and τ_2, respectively [34-35]. The phase cycles and optimization strategies were described in more detail in our earlier reports [34,43].

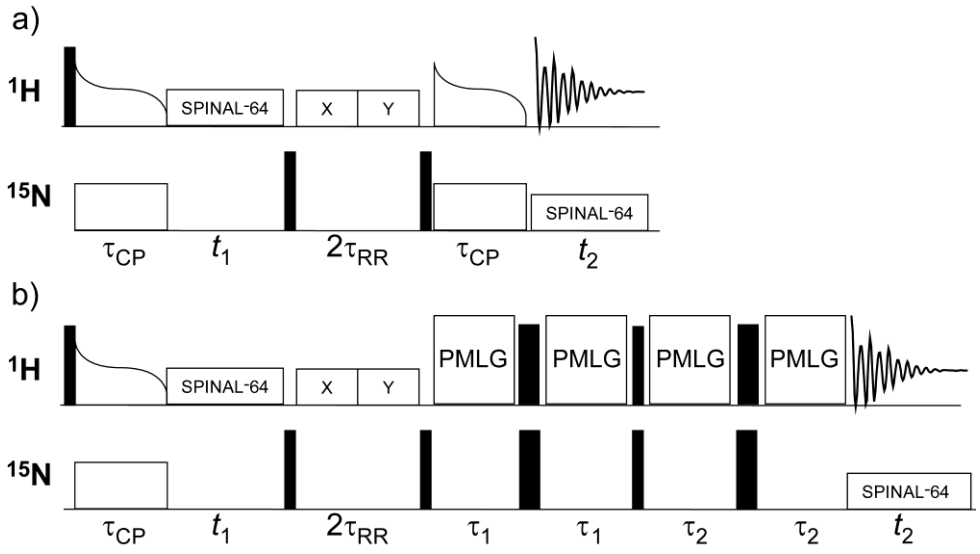

Figure 1. Pulse sequences for ^{1}H-detected HETCOR: (a) through-space with $^{15}\text{N} \rightarrow {}^{1}\text{H}$ transfer via CP and (b) through-bond with $^{15}\text{N} \rightarrow {}^{1}\text{H}$ transfer via INEPTR. States-TPPI was implemented in these experiments through phase switching of the first $\pi/2$ pulse on

the ^{15}N channel. States-TPPI was implemented in these experiments through phase switching of the first $\pi/2$ pulse in the ^{15}N channel.

The effect of heteronuclear dipolar coupling during INEPTR polarization transfer under our experimental conditions was studied using the SIMPSON simulation program [44]. The simulations were carried out for an isolated ^{1}H-^{15}N spin pair mimicking the δ_1-NH pair in histidine and for the aromatic ^{1}H-^{13}C spin pair of TMOB.

The experimental parameters are shown in figure captions using the following notation: ν_R is the MAS rate, ν_{RF}^{X} is the magnitude of the RF magnetic field applied to X nuclei, τ_{CP} is the CP contact time, τ_{RR} the is the rotary resonance recoupling time, τ_1 is the ^{15}N evolution period in INEPTR, τ_2 is the ^{1}H evolution period in INEPTR, Δt_1 is the increment of t_1 during 2D acquisition, τ_{RD} is the recycle delay, and AT is the total acquisition time of spectrum. The chemical shifts were referenced relative to ammonia (^{15}N) and tetramethylsilane (^{1}H and ^{13}C) via secondary references (glycine for ^{15}N and hexamethylbenzene for ^{1}H and ^{13}C). The data were acquired and processed using VnmrJ 2.2.C software.

3. Results and Discussion.

3.1. 2D $^{1}H\{^{15}N\}$ Spectra of MLF, Histidine and PUP-MSN.

2D ^{1}H{^{15}N} HETCOR spectra of MLF, acquired using CP (τ_{CP} = 1 ms) and INEPTR, are shown in Fig. 2. Both spectra were measured within hours and show three well-resolved resonances at around 126, 116 and 108 ppm. Following an earlier study by Griffin et al. [45] these resonances were assigned to Met, Leu and Phe residues shown on

top of the figure. The relative peak intensities in Fig. 2 are somewhat distorted by the skyline projection; however the ratios of integrated peak volumes for M, L and F are almost quantitative in both spectra. This is not surprising as the time constants that govern the CP dynamics (the relaxation time in the rotating frame, $T_{1\rho}$, and the ^{1}H-^{15}N dipolar coupling, D_{HN}) are expected to be uniform among these three sites. The J_{HN} values (~95 Hz) [46] and the INEPTR transfer efficiencies are similar as well.

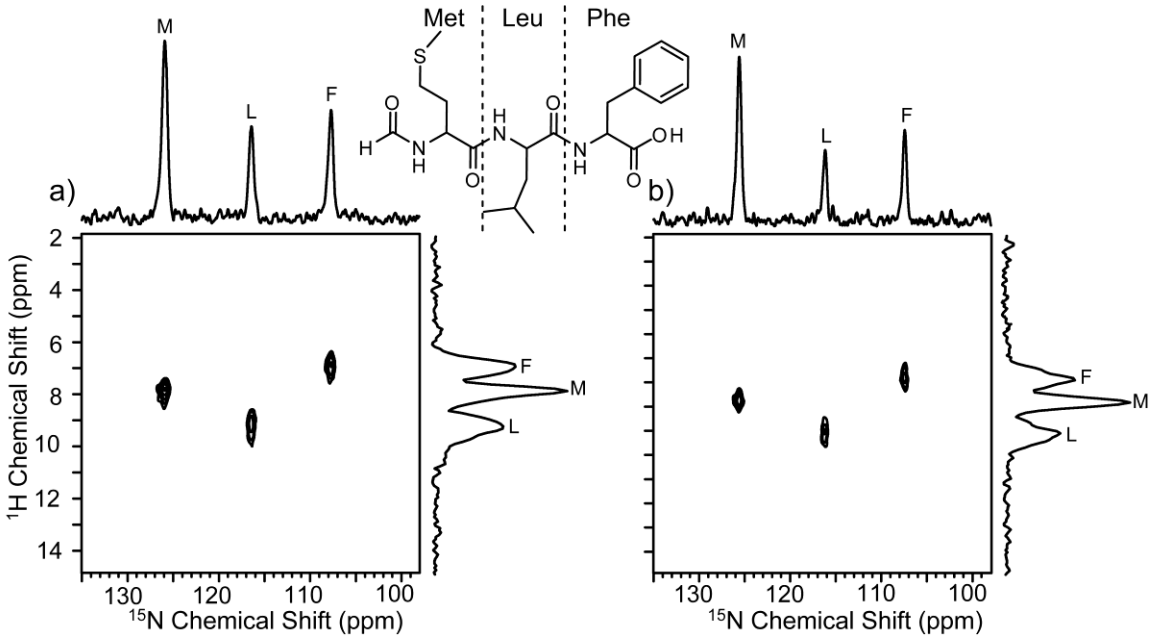

Figure 2. Through-space (a) and through-bond (b) spectra of MLF recorded with ν_R = 40 kHz, $\boldsymbol{\nu_{RF}^{H}}$ = 120 kHz during short pulses, $\boldsymbol{\nu_{RF}^{H}}$ = 60 kHz during tangent ramp CP, $\boldsymbol{\nu_{RF}^{N}}$ = 100 kHz during short pulses and CP, τ_{CP} = 1 ms, $\tau_1 = \tau_2$ = 2.5 ms, $\boldsymbol{\nu_{RF}^{H}}$ = 10 kHz and $\boldsymbol{\nu_{RF}^{N}}$ = 10 kHz during SPINAL-64 decoupling, τ_{RR} = 40 ms, and τ_{RD} = 2 s. The spectra were acquired in 245 rows with Δt_1 = 125 μs, using 16 scans per row in (a) (AT = 4.7 h) and 32 scans per row in (b) (AT = 9.5 h).

The corresponding spectra of histidine are shown in Fig. 3. Histidine, an essential amino acid and common participant in enzyme catalyzed reactions, has been thoroughly investigated using both ^{13}C and ^{15}N SSNMR [37,47-48]. The CP-based spectrum (Fig. 3a) has been acquired with a long contact time (τ_{CP} = 3 ms) and shows through-space correlations corresponding to the directly bound N-H pairs, as well as the interactions between the ring nitrogens (Nδ_1, Nε_2) and protons attached to the ring carbons δ_2 and ε_1. The observed ^{15}N and ^{1}H shifts agree exactly with those reported earlier for the cationic histidine with protonated imidazole ring [37]. In the INEPTR spectrum, as expected, the only observed correlations are those between directly bound N-H pairs. Note that in the CP spectrum the ratio of peak volumes δ_1-NH: ε_2-NH: $^{+}NH_3$ is again almost quantitative, whereas INEPTR yielded the volume ratio of approximately 1 : 2 : 1. The diminished intensity of the δ_1-NH and $^{+}NH_3$ peaks relative to ε_2-NH is mainly due to the difference in *J*-couplings at various sites within the molecule. Indeed, a 1D *J*-resolved spectrum of this sample, which we recorded under homonuclear PMLG decoupling (see Supporting Information for details) yielded J_{HN} = 115 Hz for ε_2-NH, J_{HN} = 90 Hz for δ_1-NH, and J_{HN} = 73 Hz for $^{+}NH_3$ (Fig. S1). The signal intensities during τ_1 and τ_2 are proportional to

$$I(\tau_i) \sim \sin(2\pi J_{HN} s_f \tau_i) exp(-\tau_i / 2T'_{2,i}), \quad (1)$$

where s_f is the scaling factor which determines the effective *J*-coupling (in the absence of ^{1}H-^{1}H decoupling s_f = 1, while application of PMLG leads to $s_f \approx 0.70$), and $T'_{2,1} = T_2'^{N}$ during τ_1 and $T'_{2,2} = T_2'^{H}$ during τ_2. Neglecting the relaxation terms, the intensity ratio in the spectrum in Fig. 3b should be roughly 1.5 : 2 : 1. Additional inaccuracies can be attributed to differences in T'_2 relaxation.

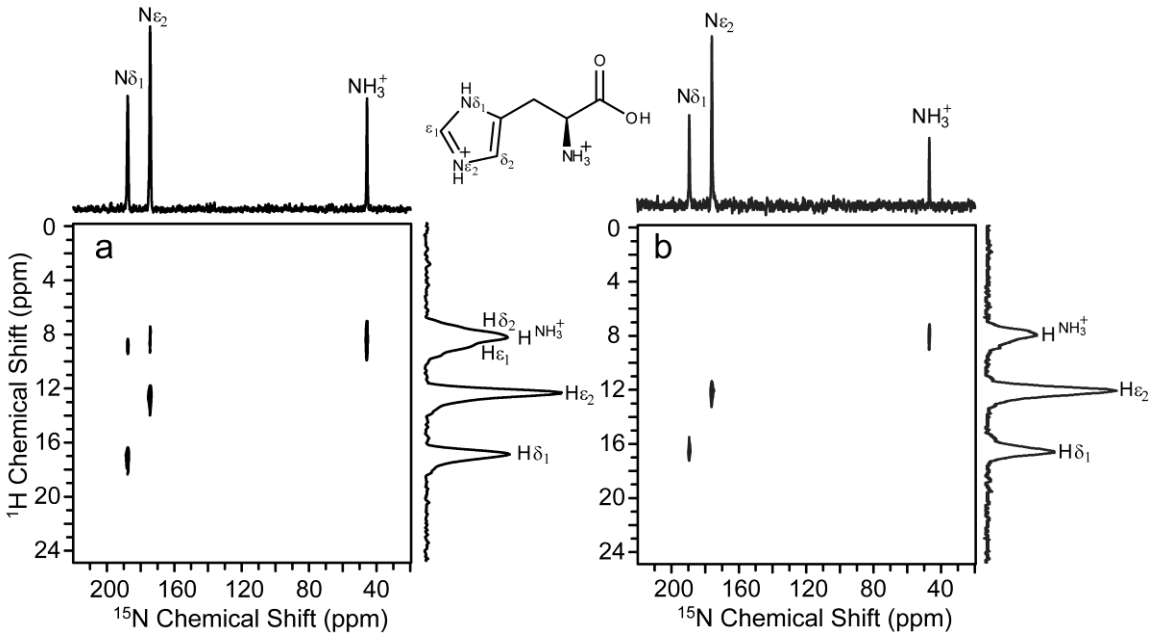

Figure 3. Through-space (a) and through-bond (b) spectra of histidine recorded with ν_R = 40 kHz, $\boldsymbol{\nu_{RF}^{H}}$ = 100 kHz during short pulses, $\boldsymbol{\nu_{RF}^{H}}$ = 70 kHz during tangent ramp CP, $\boldsymbol{\nu_{RF}^{N}}$ = 110 kHz during short pulses and CP, τ_{CP} = 3 ms, τ_1 = 2.5 ms, τ_2 = 2 ms, $\boldsymbol{\nu_{RF}^{H}}$ = 10 kHz and $\boldsymbol{\nu_{RF}^{N}}$ = 10 kHz during SPINAL-64 decoupling, τ_{RR} = 15 ms, and τ_{RD} = 4 s. The spectra were acquired in 410 rows with Δt_1 = 75 μs, using 4 scans per row in (a) (AT = 3.7 h) and 8 scans per row in (b) (AT = 7.5 h).

A 2D ^{1}H{^{15}N} CP HETCOR spectrum of PUP-MSN is shown in Fig. 4. Although the acquisition was lengthy (46 hours), this is to the best of our knowledge the first ^{15}N-^{1}H 2D spectrum of a natural abundance surface-bound species. Remarkably, the sample contained only 7 μmol of PUP (corresponding to ~3x10^{16} of ^{15}N spins), which is about an order of magnitude less than histidine or MLF studied in bulk. The spectrum of PUP-MSN exhibited considerable broadening in the ^{15}N dimension (~5 ppm) due to structural

disorder, which reduced the evolution time t_1. Our efforts to measure the corresponding through-bond spectrum of this sample were unsuccessful.

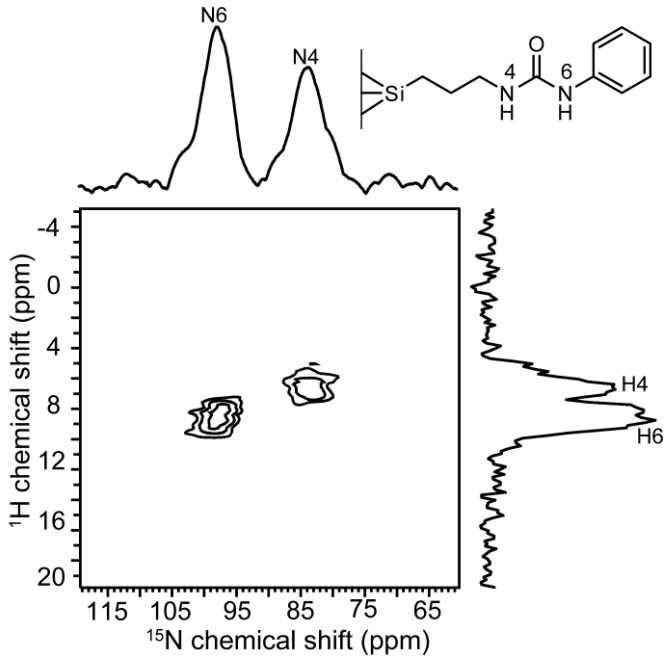

Figure 4. The spectrum of silica bound 3-(3-phenyl ureido) propyl groups recorded using the pulse sequence in Fig. 1a, with ν_R = 41.67 kHz, $\boldsymbol{\nu_{RF}^{H}}$ = 120 kHz during short pulses, $\boldsymbol{\nu_{RF}^{H}}$ = 60 kHz during tangent ramp CP, $\boldsymbol{\nu_{RF}^{N}}$ = 100 kHz during short pulses and CP, $\boldsymbol{\nu_{RF}^{H}}$ = 10 kHz and $\boldsymbol{\nu_{RF}^{N}}$ = 10 kHz during SPINAL-64 decoupling, τ_{CP} = 1 ms, τ_{RR} = 19.2 ms, 64 rows with Δt_1 = 48 μs, 1024 scans per row, τ_{RD} = 1.2 s, and AT = 46 h.

3.2. Sensitivity Gain

The sensitivity gain, *g,* offered by using indirect rather than direct detection of X nuclei can be approximated by [16]

$$g = \frac{(S/N)_{ID}}{(S/N)_{DD}} = \alpha \sqrt{\frac{\Delta\nu_X}{\Delta\nu_H}\frac{Q_H}{Q_X}}\left(\frac{\gamma_H}{\gamma_X}\right)^{3/2}, \qquad (2)$$

where α is a parameter that depends on the efficiency of polarization transfer(s) and acquisition conditions during t_1, $\Delta\nu_{H(X)}$ are the effective linewidths, and $Q_{H(X)}$ are the quality factors of the probe RF circuitry. The intrinsic sensitivity critically depends on the gyromagnetic ratios of both nuclei. Indeed, for H = ^{1}H and X = ^{15}N, the last term in Eq. 2 yields a value of 31. In solids, however, such high gains are unrealistic due to unfavorable $\Delta\nu_X/\Delta\nu_H$ ratio and losses sustained during H $\rightarrow$ X and X $\rightarrow$ H polarization transfers. Accordingly, the gains reported in the first HSQC-type experiments utilizing the CP - t_1 - CP - t_2 protocol were much lower [16,49]. Under our experimental conditions, the same scheme led to 15-fold increase in sensitivity, which corresponds to 225-fold improvement in time performance. This measurement was made using isotope-enriched glycine, because acquisition of natural abundance ^{15}N detected 2D spectrum of MLF, histidine or PUP-MSN would be prohibitively time consuming.

We also compared the sensitivity per scan between the CP-based and INEPTR-based experiments. The INEPTR method proved to be remarkably efficient, yielding in MLF 60-70% of the intensity obtained with the optimized ^{15}N $\rightarrow$ ^{1}H CP transfer. Similar efficiencies were obtained for histidine, although in this case uneven peak intensities were observed, mainly due to the abovementioned differences in coupling constants. Note that long range, through-space correlations can be suppressed in the CP spectra by limiting the contact time to less than 50 μs, however such a strategy considerably reduces the overall sensitivity. It follows from Eq. 1 that the loss of magnetization during INEPTR is attributable to decoherence of transverse ^{1}H magnetization during τ_2 ($T_2'^H$ relaxation) and, to a much lesser extent, ^{15}N magnetization during τ_1 ($T_2'^N$ relaxation). Although the use of fast MAS and PMLG$_m^{\bar{x}}$ decoupling reduces the relaxation losses, they

remain non-uniform, thereby contributing to quantitative inaccuracy. A detailed analysis of the effect of fast MAS and ^{1}H-^{1}H homonuclear RF decoupling on transverse relaxation has been reported in earlier studies of INEPT transfers between ^{1}H and ^{13}C [34-35].

We should also comment that the use of 1.6-mm rotor did not impose a penalty in terms of sensitivity when compared to a 3.2-mm rotor. Specifically, our tests indicated that the S/N ratio measured in direct polarization ^{13}C MAS experiment on hexamethylbenzene (HMB) using our Varian FastMAS^{TM} probe was only ~33 % lower than using the 3.2-mm Varian T3 probe under equivalent conditions (experiments were optimized back-to-back on the same spectrometer, with fully packed rotors, the same parameters during data acquisition and processing, etc.). Thus, in spite of three times smaller sample volume (8 μL vs. 22 μL) the signal loss is mostly offset by higher receptivity per spin. Further, as reported earlier [30-33,50], the CP process is very efficient under fast MAS, provided that the undesired recoupling conditions are avoided (i.e., $\nu_{RF}^{H}/\nu_R \neq$ ½, 1, 2) [51-52]. Still, we found it remarkable that a CPMAS spectrum of HMB acquired at ν_R = 40 kHz on a 1.6-mm probe showed a higher S/N ratio (by approximately 25 %) than one acquired at ν_R = 20 kHz on a 3.2-mm probe. The spectra and the experimental conditions used in these tests are reported in Supporting Information (Figs. S2 and S3).

3.3. Numerical Simulations of INEPTR Transfer

Numerical simulations were performed using SIMPSON software [44] to verify that the polarization transfer in our INEPTR experiments was governed by *J*-coupling

and not by heteronuclear dipolar interactions, as suggested in recent study [53]. Fig. 5 shows the simulated 1D $^{1}H \rightarrow {}^{15}N$ INEPTR spectra of a spin system consisting of isolated ^{1}H-^{15}N spin pairs corresponding to δ_1-NH in histidine. Accordingly, J_{HN} and D_{HN} were set to 90 Hz and 20.34 kHz [54]. Other parameters, given in the figure caption, were chosen in correspondence with the conditions used in our experiments. The simulations were performed assuming that D_{HN} coupling, J_{HN} coupling, or both D_{HN} and J_{HN} couplings are operable during τ_1 and τ_2. The resulting spectra demonstrate that the *J*-coupling is responsible for the polarization transfer during the INEPTR sequence under the conditions used in the present study, with dipolar coupling having a negligible effect.

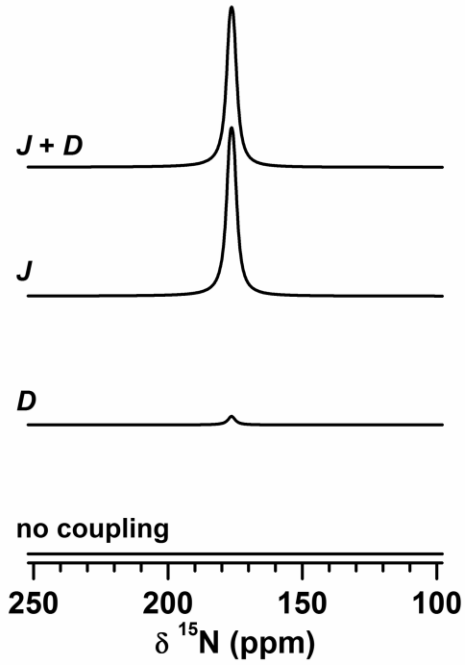

Figure 5. Simulated $^{1}H \rightarrow {}^{15}N$ INEPTR spectra with various coupling conditions, obtained for B_0 = 14.1 T, ν_R = 40 kHz, $\boldsymbol{\nu_{RF}^{H}}$ = 100 kHz, $\boldsymbol{\nu_{RF}^{N}}$ = 100 kHz, τ_1 = 2.5 ms, and τ_2 = 2.0 ms. The TPPM ^{1}H decoupling was applied during acquisition with $\boldsymbol{\nu_{RF}^{H}}$ = 100 kHz, π

pulse and $\Phi = \pm 25°$. The same results were obtained for τ_1 and τ_2 values that were not rotor-synchronized.

To further validate this result, we measured the evolution of the signal observed in 1D $^{1}H \rightarrow {}^{13}C$ INEPTR of TMOB (for the aromatic ring C-H pairs, where $D_{HC} = 22.5$ kHz and $J_{HC} = 160$ Hz (Fig. S4)) as a function of τ_1 and τ_2, both with and without PMLG decoupling (Figs. S5-S8). The evolution curves follow exactly the theoretically expected *J*-mediated evolution given in Eq. 1. A simulation using SIMPSON again confirmed that the contribution from dipolar coupling to the polarization transfer is negligibly small (Fig. S9).

4. Conclusion

The 2D $^{1}H\{^{15}N\}$ HETCOR spectra of natural abundance solids can be reliably measured by employing fast MAS, indirect detection, advances in ^{1}H-^{1}H homonuclear decoupling, and $^{15}N \rightarrow {}^{1}H$ polarization transfers via CP or INEPTR. The INEPTR scheme was shown to rely solely on *J*-couplings and proved more efficient in identifying through-bond correlations than the CP-based measurements with short contact time, which can be additionally affected by molecular motion. These through-space and through-bond correlation spectra can lead to a better understanding of the structures and conformations in a variety of systems in biology, materials science, medicine and catalysis. They can be also combined with ^{14}N SSNMR spectroscopy to obtain additional information about local symmetry and mobility.

5. Acknowledgments

This research was supported at the Ames Laboratory by the U.S. Department of Energy, Office of Basic Energy Sciences, under Contract No. DE-AC02–07CH11358. We thank Dr. Tommy Hung-Ting Chen for preparing the PUP-MSN material, and Prof. Mei Hong and Jonathan Williams for providing the sample of ^{15}N-enriched histidine.

6. References

[1] H.J. Jakobsen, H. Bildsøe, J. Skibsted, and T. Giavani, J. Am. Chem. Soc. 123 (2001) 5098-5099.

[2] H.J. Jakobsen, H. Bildsøe, J. Skibsted, and T. Giavani, J. Magn. Reson. 166 (2004) 262-272.

[3] F.H. Larsen, H.J. Jakobsen, P.D. Ellis, and N.C. Nielsen, J. Phys. Chem. A 101 (1997) 8597-8606.

[4] L.A. O'Dell, and R.W. Schurko, Phys. Chem. Chem. Phys. 11 (2009) 7069-7077.

[5] L.A. O'Dell, R.W. Schurko, K.J. Harris, J. Autschbach, and C.I. Ratcliffe, J. Am. Chem. Soc. 133 (2011) 527-546.

[6] S. Cavadini, A. Lupulescu, S. Antonijevic, and G. Bodenhausen, J. Am. Chem. Soc. 128 (2006) 7706.

[7] Z. Gan, J. Am. Chem. Soc. 128 (2006) 6040-6041.

[8] S. Cavadini, S. Antonijevic, A. Lupulescu, and G. Bodenhausen, J. Magn. Reson. 182 (2006) 168-172.

[9] Z. Gan, J.P. Amoureux, and J. Trébosc, Chem. Phys. Lett. 435 (2007) 163-169.

[10] A.S. Tatton, T.N. Pham, F.G. Vogt, D. Iuga, A.J. Edwards, and S.P. Brown, Mol. Pharmaceutics 10 (2013) 999-1007.

[11] A.L. Webber, S. Masiero, S. Pieraccini, J.C. Burley, A.S. Tatton, D. Iuga, T.N. Pham, G.P. Spada, and S.P. Brown, J. Am. Chem. Soc. 133 (2011) 19777-19795.

[12] L. Mueller, J. Am. Chem. Soc. 101 (1979) 4481-4484.

[13] G. Bodenhausen, and D.J. Ruben, Chem. Phys. Lett. 69 (1980) 185-189.

[14] A. Bax, R.H. Griffey, and B.L. Hawkins, J. Magn. Reson. 55 (1983) 301-315.

[15] A. Lesage, P. Charmont, S. Steuernagel, and L. Emsley, J. Am. Chem. Soc. 122 (2000) 9739-9744.

[16] Y. Ishii, and R. Tycko, J. Magn. Reson. 142 (2000) 199-204.

[17] B. Reif, and R.G. Griffin, J. Magn. Reson. 160 (2003) 78-83.

[18] E.K. Paulson, C.R. Morcombe, V. Gaponenko, B. Dancheck, R.A. Byrd, and K.W. Zilm, J. Am. Chem. Soc. 125 (2003) 15831-15836.

[19] V. Chevelkov, K. Rehbein, A. Diehl, and B. Reif, Angew. Chem. Int. Ed. 45 (2006) 3878-3881.

[20] I. Schnell, B. Langer, S.H.M. Söntjens, M.H.P. van Genderen, R.P. Sijbesma, and H.W. Spiess, J. Magn. Reson. 150 (2001) 57-70.

[21] I. Schnell, and K. Saalwächter, J. Am. Chem. Soc. 124 (2002) 10938-10939.

[22] L.-S. Du, A. Samoson, T. Tuherm, and C.P. Grey, Chem. Mat. 12 (2000) 3611-3616.

[23] A. Samoson, Extended Magic-Angle Spinning. in: D.M. Grant, and R.K. Harris, (Eds.), Encyclopedia of Nuclear Magnetic Resonance, John Willy & Sons, Chinchester, 2002, pp. 59-64.

[24] Y. Nishiyama, Y. Endo, T. Nemoto, H. Utsumi, K. Yamauchi, K. Hioka, and T. Asakura, J. Magn. Reson. 208 (2011) 44-48.

[25] Y. Nishiyama, Y. Endo, and T. Nemoto, 53rd ENC, Miami, FL, USA,, 2012.

[26] M. Ernst, M.A. Meier, T. Tuherm, A. Samoson, and B.H. Meier, J. Am. Chem. Soc. 126 (2004) 4764-4765.

[27] S.P. Brown, X.X. Zhu, K. Saalwächter, and H.W. Spiess, J. Am. Chem. Soc. 123 (2001) 4275-4285.

[28] B. Alonso, and D. Massiot, J. Magn. Reson. 163 (2003) 347-352.

[29] K. Mao, J.W. Wiench, V.S.-Y. Lin, and M. Pruski, J. Magn. Reson. 196 (2009) 92-95.

[30] M. Ernst, A. Detken, A. Böckmann, and B.H. Meier, J. Am. Chem. Soc. 125 (2003) 15807-15810.

[31] J. Trebosc, J.W. Wiench, S. Huh, V.S.Y. Lin, and M. Pruski, J. Am. Chem. Soc. 127 (2005) 7587-7593.

[32] S.M. Althaus, K. Mao, G.J. Kennedy, and M. Pruski, Energy Fuels 26 (2012) 4405-4412.

[33] D.H. Zhou, G. Shah, C. Mullen, D. Sandoz, and C.M. Rienstra, Angew. Chem. Int. Ed. 48 (2009) 1253-1256.

[34] K. Mao, and M. Pruski, J. Magn. Reson. 201 (2009) 165-174.

[35] B. Elena, A. Lesage, S. Steuernagel, A. Böckmann, and L. Emsley, J. Am. Chem. Soc. 127 (2005) 17296-17302.

[36] M. Leskes, S. Steuernagel, D. Schneider, P.K. Madhu, and S. Vega, Chem. Phys. Lett. 466 (2008) 95-99.

[37] S. Li, and M. Hong, J. Am. Chem. Soc. 133 (2011) 1534-1544.

[38] H.-T. Chen, B.G. Trewyn, J.W. Wiench, M. Pruski, and V.S.-Y. Lin, Top Catal 53 (2010) 187-191.

[39] B.M. Fung, A.K. Khitrin, and K. Ermolaev, J. Magn. Reson. 142 (2000) 97-101.

[40] T.G. Oas, R.G. Griffin, and M.H. Levitt, J. Chem. Phys. 89 (1988) 692.

[41] M. Leskes, P.K. Madhu, and S. Vega, J. Chem. Phys. 125 (2006) 124506.

[42] M. Leskes, P.K. Madhu, and S. Vega, Chem. Phys. Lett. 447 (2007) 370-374.

[43] K. Mao, and M. Pruski, J. Magn. Reson. 203 (2010) 144-149.

[44] M. Bak, J.T. Rasmussen, and N.C. Nielsen, J. Magn. Reson. 147 (2000) 296-330.

[45] C.M. Rienstra, L. Tucker-Kellogg, C.P. Jaroniec, M. Hohwy, B. Rief, M.T. McMahon, B. Tidor, T. Lozano-Perez, and R.G. Griffin, Proc. Natl. Acad. Sci. 99 (2002) 10260–10265.

[46] G.J. Martin, M.L. Martin, and J.-P. Gouesnard, ^{15}N-NNMR Spectroscopy, Springer Berlin Heidelberg, 1981.

[47] F. Hu, K. Schmidt-Rohr, and M. Hong, J. Am. Chem. Soc. 134 (2011) 3703-3713.

[48] Y. Wei, A.C. de Dios, and A.E. McDermott, J. Am. Chem. Soc. 121 (1999) 10389-10394.

[49] Y. Ishii, J.P. Yesinowski, and R. Tycko, J. Am. Chem. Soc. 123 (2001) 2921-2922.

[50] S. Laage, A. Marchetti, J. Sein, R. Pierattelli, H.J. Sass, S. Grzesiek, A. Lesage, G. Pintacuda, and L. Emsley, J. Am. Chem. Soc. 130 (2008) 17216-17217.

[51] A. Lange, I. Scholz, T. Manolikas, M. Ernst, and B.H. Meier, Chem. Phys. Lett. 468 (2009) 100-105.

[52] I. Scholz, B.H. Meier, and M. Ernst, J. Chem. Phys. 127 (2007) 204504.

[53] G.P. Holland, B.R. Cherry, J.E. Jenkins, and J.L. Yarger, J. Magn. Reson. 202 (2010) 64-71.

[54] A. Ramamoorthy, C.H. Wu, and S.J. Opella, J. Am. Chem. Soc. 119 (1997) 10479-10486.

Supporting Information

Measurement of J-resolved Spectra

The measurements of the *J*-couplings in histidine and 1,3,5 trimethoxybenzene (TMOB) in the solid state were performed on a Varian 600-MHz NMR System spectrometer using a 1.6-mm FastMAS^{TM} T3 triple resonance probe operated at 599.6 MHz for ^{1}H, 150.8 MHz for ^{13}C, and 60.8 MHz for ^{15}N. TMOB has sufficiently narrow lines under MAS at 40 kHz to allow the measurement of a *J*-resolved DPMAS spectrum without any ^{1}H RF decoupling (Fig. S4), which yielded J_{HC} = 160 Hz for the C-H ring pair. Histidine, on the other hand, required the use of PMLG ^{1}H homonuclear decoupling during acquisition of the ^{15}N signal [1-2]. A *J*-resolved ^{15}N CPMAS spectrum of ^{15}N-enriched histidine is shown in Fig. S1. Note that the use of PMLG did cause the *J*-couplings to be scaled by a factor of 0.65. This measurement led to *J*-couplings of J_{HN} = 115 Hz for ε_2-NH, J_{HN} = 90 Hz for δ_1-NH, and J_{HN} = 73 Hz for $^{+}NH_3$.

Comparison of Probe Sensitivity in ^{13}C DPMAS and CPMAS Measurements on Hexamethylbenzene (HMB)

The probes compared in this study were a 1.6-mm FastMAS^{TM} T3 triple resonance probe (rotor holds 8 μL of sample) and a 3.2-mm T3 triple resonance probe (rotor holds 22 μL). Both rotors were fully packed with HMB and experiments were preformed and processed with similar parameters, which are listed in the captions to Figs S2 and S3. The signal to noise ratios (S/N) were evaluated for the methyl resonance (17.3 ppm) of HMB, because it does not have any spinning sidebands in the spectra taken with both probes. The DPMAS measurements (Fig. S2) showed that the FastMAS probe has

approximately double the sensitivity of the 3.2-mm probe (S/N per μL of sample were 7.1 and 3.9, respectively). In the CPMAS measurement (Fig. S3) the corresponding numbers were 12 and 3.6, which shows that the overall sensitivity of FastMAS probe was superior despite the smaller rotor size.

Signal Intensity During INEPTR Transfer

The time evolution of INEPTR signal was investigated by examining the behavior of the protonated ring carbon in TMOB. The evolution curves of TMOB were measured by acquisition of 1D $^{1}H \rightarrow {}^{13}C$ INEPTR spectra with varying τ_1 or τ_2. The observed data exactly followed the theoretical curve (Eq. 1) with J_{HC} = 160 Hz (Figs. S5-S8). In all 1D INEPTR measurements the following parameters were used: ν_R = 40 kHz, ν_{RF}^{H} = 155 kHz, ν_{RF}^{C} = 100 kHz, ν_{RF}^{H} = 10 kHz during SPINAL-64 decoupling, τ_{RD} = 3 s, AT = 1 min per row. Other parameters are listed in the figure captions. Numerical simulations of this experiment were performed using SIMPSON [3] (Fig. S9). The results confirmed that the transfer is mediated by *J*-couplings with a negligible contribution from dipolar coupling.

References

[1] T. Terao, H. Miura, and A. Saika, J. Chem. Phys. 75 (1981) 1573-1574.

[2] T. Terao, H. Miura, and A. Saika, J. Magn. Reson. 49 (1982) 365-367.

[3] M. Bak, J.T. Rasmussen, and N.C. Nielsen, J. Magn. Reson. 147 (2000) 296-330.

Figures

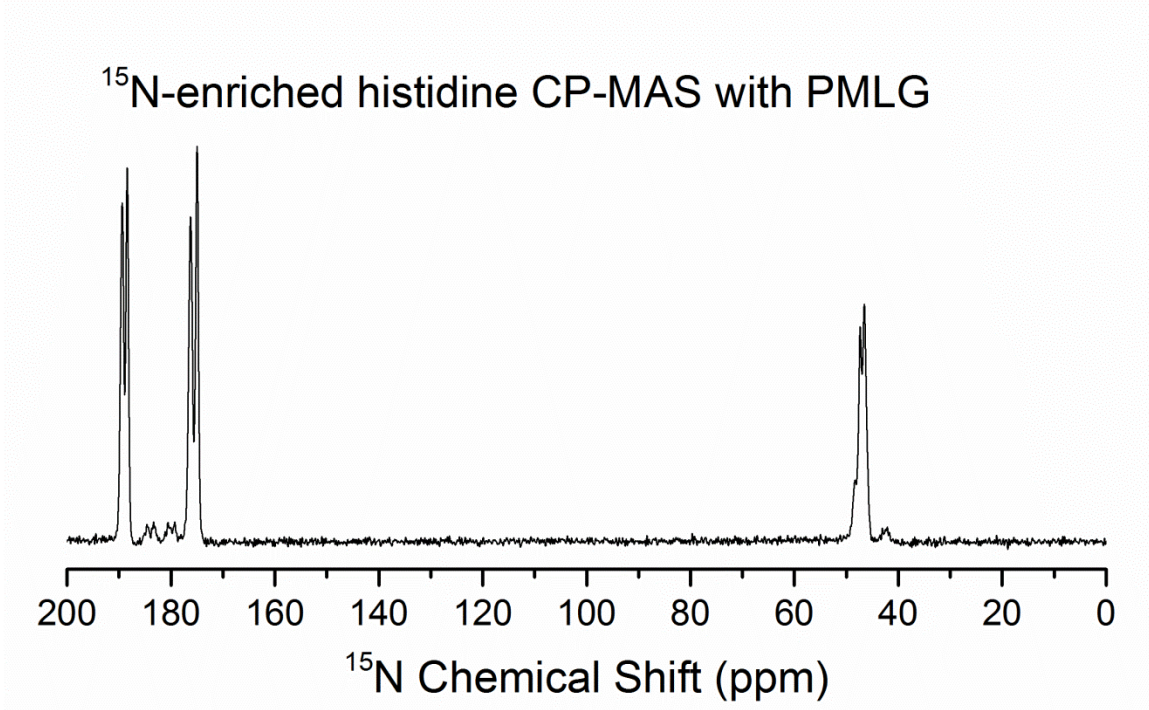

Figure. S1. CPMAS spectrum of ^{15}N-enriched histidine acquired with PMLG during acquisition: ν_R = 40 kHz, ν_{RF}^{H} = 70 kHz during tangent ramp CP, ν_{RF}^{C} = 110 kHz during CP, ν_{RF}^{H} = 155 kHz during PMLG decoupling, τ_{CP} = 3 ms, τ_{RD} = 4 s, and AT = 1 min.

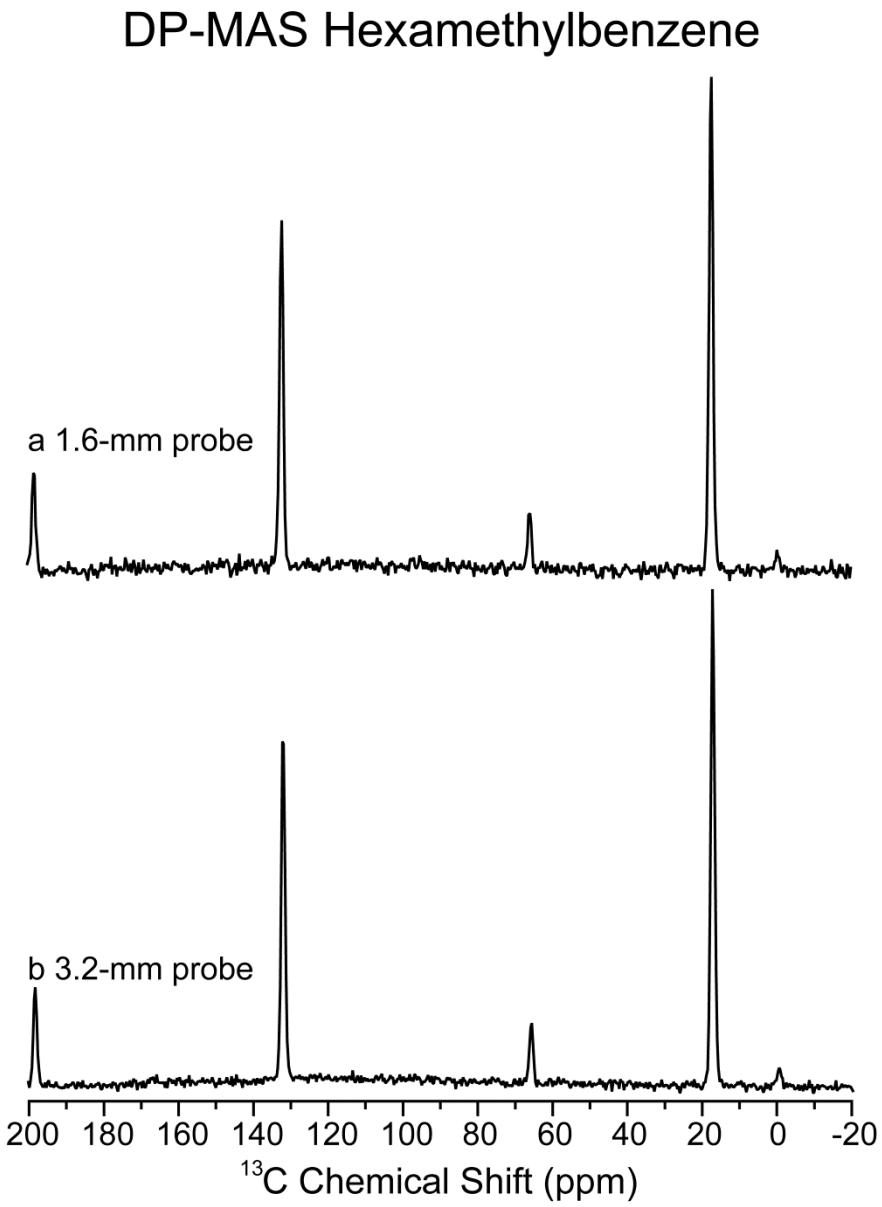

Fig. S2. DPMAS spectra of HMB were measured on (a) 1.6-mm probe and (b) 3.2-mm probe, using the following parameters: ν_R = 10 kHz, ν_{RF}^C = 100 kHz, ν_{RF}^H = 45 kHz during TPPM decoupling, τ_{RD} = 60 s, and AT = 2.1 hr. No line broadening was applied to the spectra.

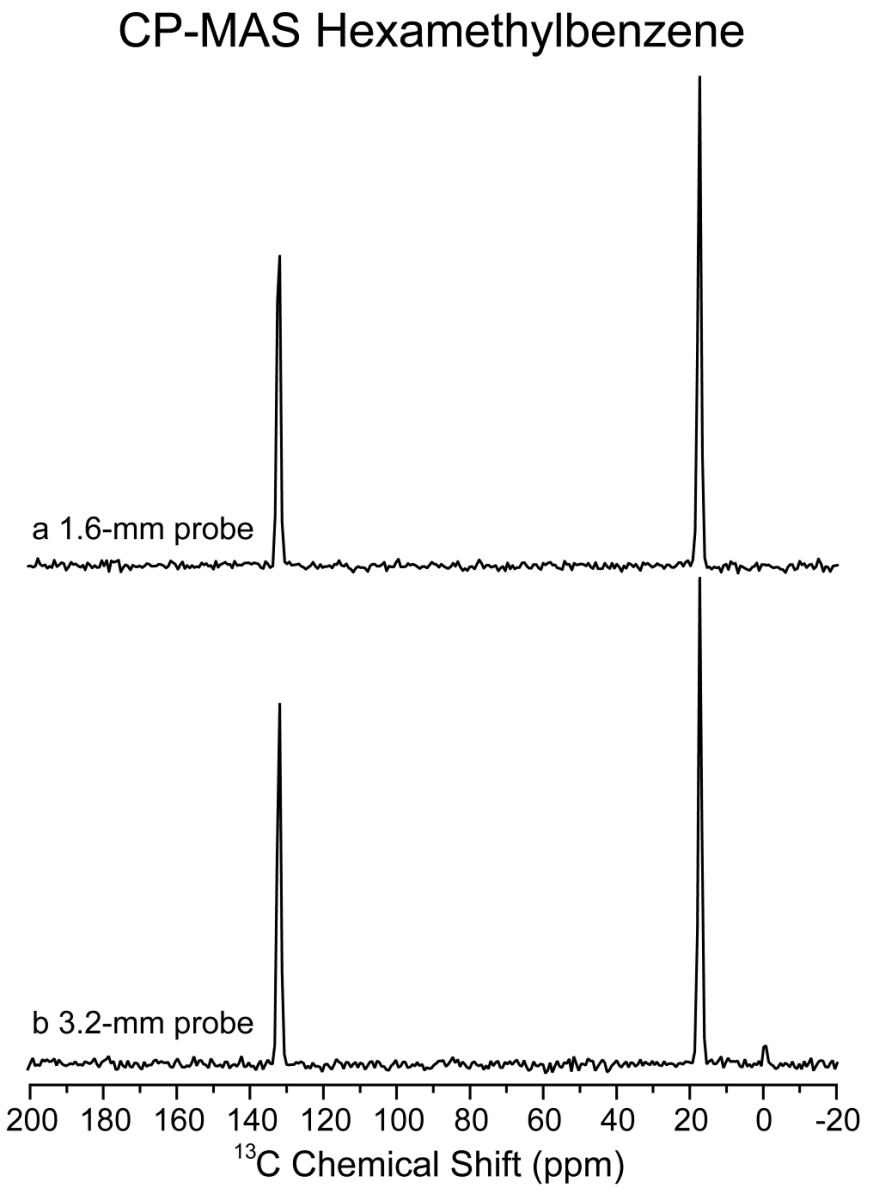

Fig. S3. CPMAS spectra were acquired on two different probes: (a) 1.6-mm probe: ν_R = 40 kHz, ν_{RF}^{H} = 60 kHz during tangent ramp CP, ν_{RF}^{C} = 100 kHz during CP, ν_{RF}^{H} = 10 kHz during SPINAL-64 decoupling, τ_{CP} = 7 ms, τ_{RD} = 5 s, AT = 1 min. (b) 3.2-mm probe: ν_R = 20 kHz, ν_{RF}^{H} = 80 kHz during tangent ramp CP, ν_{RF}^{C} = 60 kHz during CP, ν_{RF}^{H} = 80 kHz during SPINAL-64 decoupling, τ_{CP} = 7 ms, τ_{RD} = 5 s, and AT = 1 min. No line broadening was applied to the spectra.

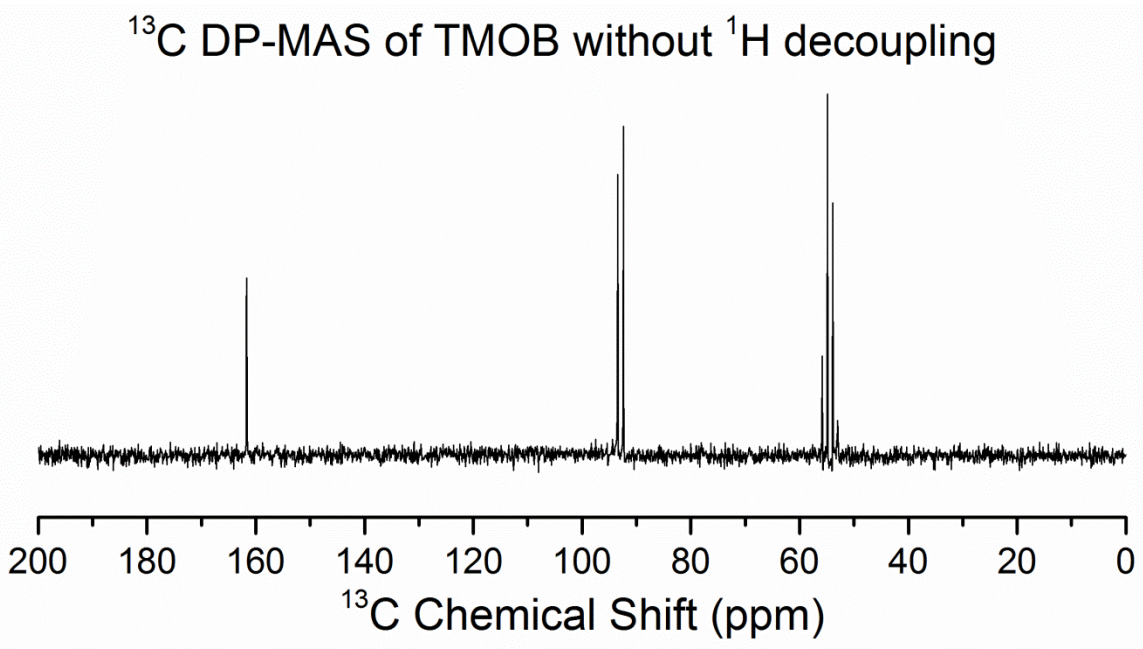

Fig. S4. *J*-resolved DPMAS spectrum of TMOB measured using the following parameters: $\nu_R = 40$ kHz, $\nu_{RF}^{C} = 100$ kHz, $\tau_{RD} = 3$ s, and $AT = 2$ min.

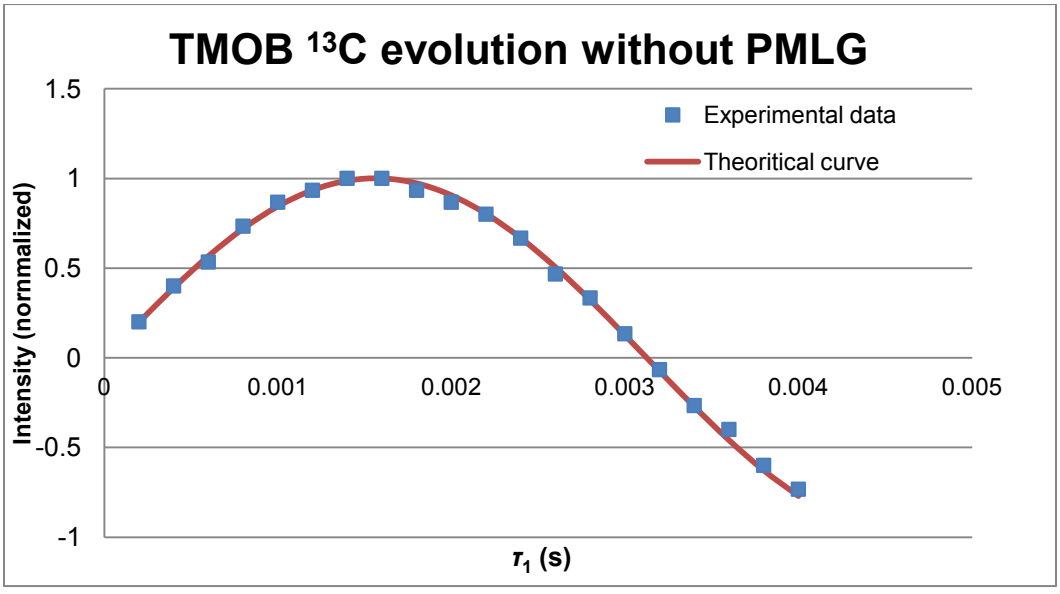

Fig. S5. The ^{13}C signal intensity in INEPTR without PMLG, where τ_1 is arrayed from 0.2 ms to 4 ms and $\tau_2 = 1.6$ ms. The blue squares (■) are experimental data and the red line is the theoretical curve (Eq. 1), where $s_f = 1$ and T_2' relaxation is negligibly slow.

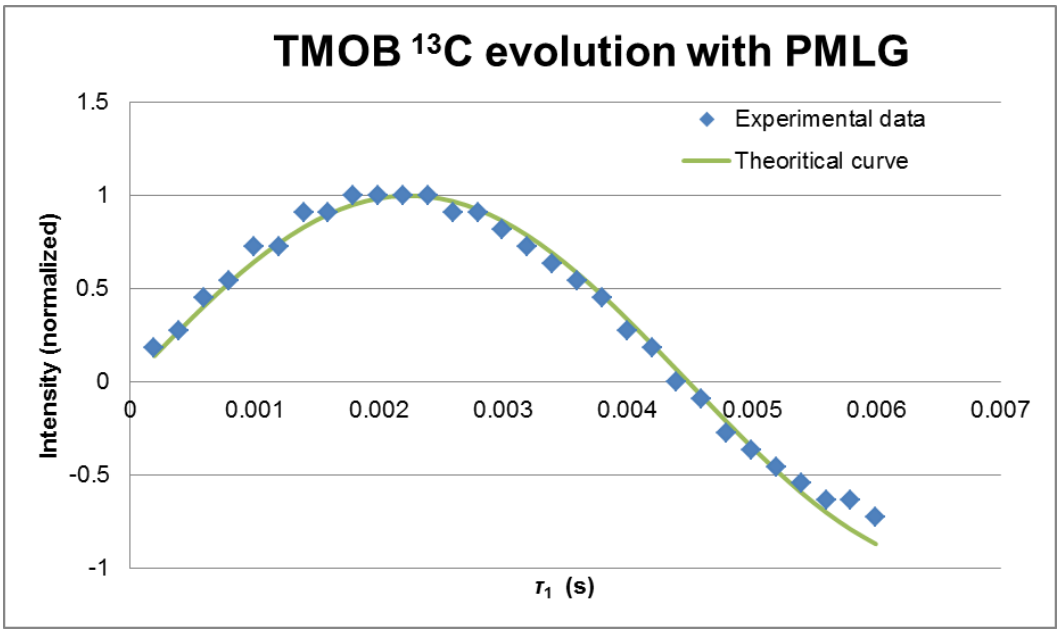

Fig. S6. The ^{13}C signal intensity in INEPTR with PMLG, where τ_1 is arrayed from 0.2 ms to 6 ms and $\tau_2 = 1.6$ ms. The blue squares (■) are experimental data and the green line is the theoretical curve (Eq. 1), where $s_f = 0.7$ and T_2' relaxation is negligibly slow.

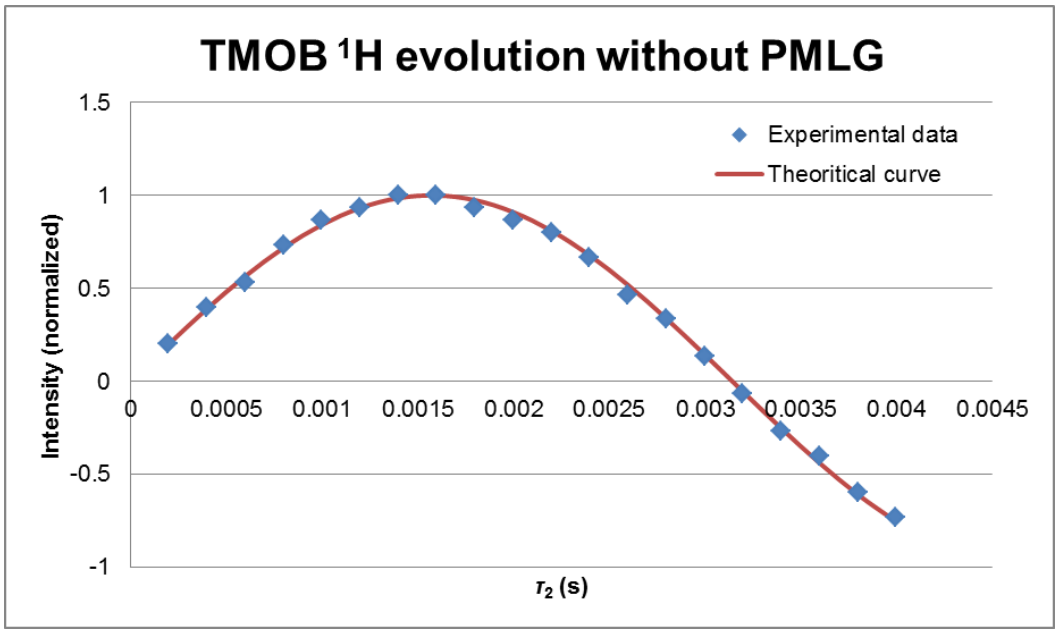

Fig. S7. The ^{1}H signal intensity in INEPTR without PMLG, where τ_1 =1.6 ms and τ_2 is arrayed from 0.2 ms to 4 ms. The blue squares (■) are experimental data and the red line is the theoretical curve (Eq. 1), where s_f = 1 and T_2' relaxation is negligibly slow.

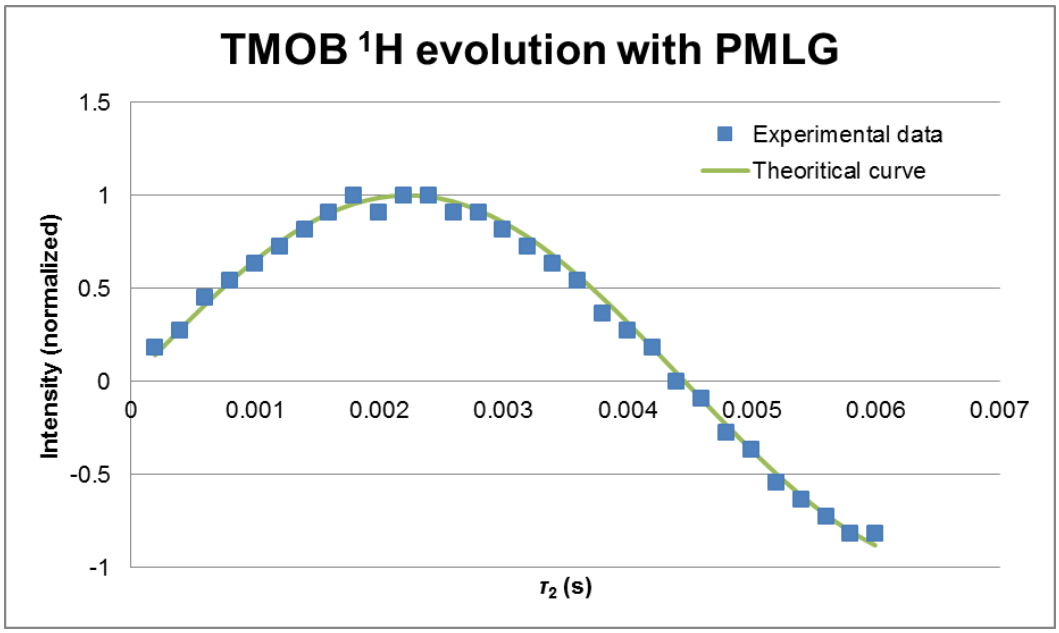

Fig. S8. The ^{1}H signal intensity in INEPTR with PMLG, where τ_1 =1.6 ms and τ_2 is arrayed from 0.2 ms to 6 ms. The blue squares (■) are experimental data and the green line is the theoretical curve (Eq. 1), where s_f = 0.7 and T_2' relaxation is negligibly slow.

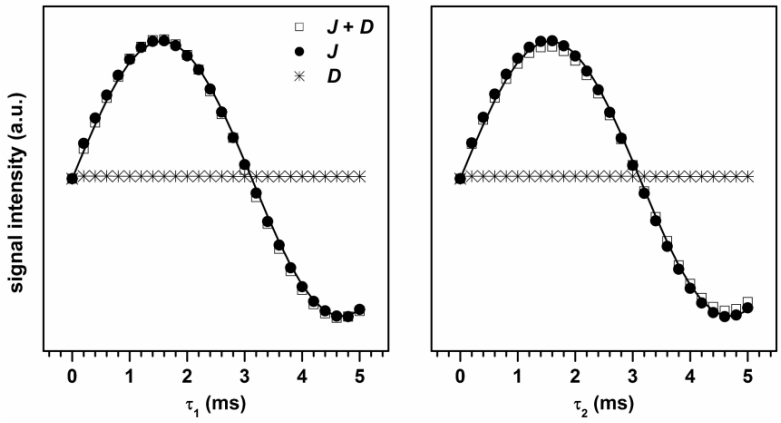

Fig. S9. Polarization transfer efficiencies via INEPTR for the CH model, as a function of (a) τ_1 delays with τ_2 = 1.6 ms and (b) τ_2 delays with τ_1 = 1.6 ms. The simulations were carried out under the following conditions: B_0 = 14.1 T, ν_{RF}^{H}=100 kHz, ν_{RF}^{N}=100 kHz. The effect of T_2' relaxation during the delay times was not taken into account.

CHAPTER 4: ALDOL CONDENSATION IN HETEROGENEOUS CATALYSIS: A MECHANISTIC STUDY

As adapted from previous publications: K. Kandel, S.M. Althaus, C. Peeraphatdit, T. Kobayashi, B.G. Trewyn, M. Pruski, and I.I. Slowing, *Journal of Catalysis* 291 (**2012**) 63-68 and K. Kandel, S.M. Althaus, C. Peeraphatdit, T. Kobayashi, B.G. Trewyn, M. Pruski, and I.I. Slowing, *ACS Catalysis* 3 (**2013**) 265-271

Abstract

The study of mesoporous silica nanoparticles (MSNs) by solid state NMR has been a large part of my graduate research. Although I will not describe all the different subjects I have worked on, I will present the study of aldol condensation via amine functionalized MSN that I completed alongside Kapil Kandel. This study is a good demonstration of how the combination of synthetic efforts and characterization techniques can lead to a better catalyst design. Specifically, characterization techniques are used to determine the root cause of the low activity of MSN functionalized with primary amines, namely the presence of an imine intermediate which results in substrate inhibition. Modification of the functional group to a secondary amine increases the catalysts' activity. A further increase in activity is seen upon changing the solvent from hexane to water; however, it also inhibits the activity rate in the secondary amine. The

cooperativity of the surface is also examined and shows the overall benefit of heterogeneous catalysis for the aldol condensation reaction.

1. Introduction

Heterogeneous catalysts are desirable in many reactions because of the ease of product separation and their reusability [1]. Unfortunately these catalysts often have inferior kinetics and selectivity in comparison to homonuclear catalysts, along with a more complex reaction mechanism. Understanding the exact pathway by which reactions take place can lead to improved performance. Mechanistic studies of heterogeneous catalytic systems involve examining and deconvoluting the roles of each individual component. Especially important is understanding the roles of support and the solvent [2-5]. Solid state NMR can be particularly useful in this endeavor.

In this chapter, cross-aldol condensation is examined, which is an important reaction for C-C bond formation [6-10]. Specifically the reaction between *p*-nitrobenzaldehyde (**PNB**) and acetone (Scheme 1) will be studied. In the homogenous environment this reaction can be catalyzed by strong acids/bases, through nucleophilic addition with enolization [11-12], and proline/ catayitic antibodies [13-14]. A variety of aminoalkyl based heterogeneous catalysts have been developed for this reaction [15-21]. While catalysis occurs in these systems, the efficiency is generally very low [17-18,20-24]. Previous studies have shown an increase in the catalytic activity by adding a secondary acidic group to the surface [20,22,25]. Although this bifunctionalized method was found to increase the activity, the low activity of the surface bound amine groups is yet to be explained.

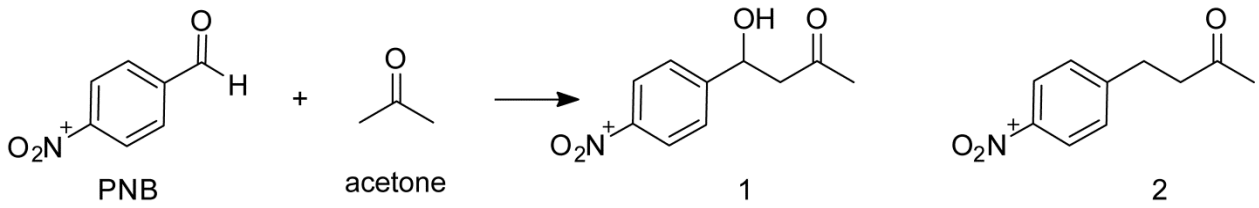

Scheme 1. The cross aldol condensation between *p*-nitrobenzaldehyde, **PNB**, and acetone

In homogenous catalysis, solvent selection is known to be important for the overall activity. The solvent effect has been less investigated in heterogeneous media [26]. The previously mentioned study by Davis and co-workers showed that the polarity of the solvent affected the reaction activity of the bifunctionalized systems for the aldol condensation between **PNB** and acetone [22]. They concluded that the polarity affected the acid-base equilibrium; more polar solvents interacted more strongly with the surface groups, thereby decreasing the activity. A report using carboxylic acid and primary amines bifunctionalized mesoporous silica supported these results using hexane and nonane as solvents [25].

In the following we will: (1) investigate the cause of low efficiency of the cross-aldol condensation catalyzed by the heterogeneous primary amine and eliminate the inhibition pathway by using a secondary amine, (2) investigate the critical effect of solvent on the catalytic activity, and (3) explain the cooperative effect between the amine groups and the support along with its role in improving the activity of the heterogeneous system with respect to its homogeneous counterpart.

2. Experimental

2.1 Samples

2.1.1 Materials

Cetyltrimethylammonium bromide (CTAB), mesitylene, *p*-nitrobenzaldehyde (**PNB**), hexamethyldisilazane (HMDS) and dimethyl sulfone (DMSO) were purchased from Sigma-Aldrich. Tetraethylorthosilicate (TEOS), 3-aminopropyl trimethoxysilane, [3-(Methylamino) propyl] trimethoxysilane and [3-(N, N-Dimethylamino) propyl] trimethoxysilane were purchased from Gelest. ^{13}C enriched acetone was purchased from Cambridge Isotope Laboratory. All reagents were used as received without further purification.

2.1.2 Synthesis of Smaller Pore MSNs

The synthesis of the MSN materials was done by Igor Slowing and Kapil Kandel as described in earlier references [27-29]. In brief, 1.0 g of CTAB (2.7 mmol) was dissolved in 480 g of nanopure water (26.7 mmol), then 3.5 mL of NaOH (2.0 M, 7.0 mmol) was added. This mixture was then heated at 80° C for 1 hr. 4.7 g of TEOS (23 mmol) was added dropwise to the solution, followed by the addition of 1 ml of 3-aminopropyl trimethoxysilane(5.7 mmol) (for AP-MSN) or 1 ml of [3-(N,N-Dimethylamino)propyl] trimethoxysilane (5.0 mmol)(for MAP-MSN). These solutions were then stirred vigorously for 2 hrs at 80° C and filtered to separate out MSN products. The filtered material was then washed with copious amounts of water and methanol and then dried under vacuum. To remove CTAB, a soxhlet extraction with methanol was done for 24 hrs and followed by overnight drying under vacuum. This method produced the smaller pore size samples, denoted as AP-MSN-2.8 and MAP-MSN-2.6, with pore sizes of 2.8 nm and 2.6 nm, respectively.

2.1.3 Synthesis of Larger Pore Samples

The pore expanded materials were prepared by Kapil Kandel as previous reported [27-29] with 1.73 g of mesitylene (14.4 mmol) added to the initial step. This resulted in the expanded pore material AP-MSN-3.6 and MAP-MSN-3.5, with pore sizes of 3.6 nm and 3.5 nm, respectively. DMAP-MSN-3.2 was also prepared with the use of 1.0 ml of the [3-(N, N-Dimethylamino) propyl] trimethoxysilane (4.6 mmol) added after TEOS.

2.1.4 Silylation

To block the silanol groups, 1.0 g of AP-MSN-3.6 or MAP-MSN-3.5 was suspended in 100 mL of hexane and hexamethyldisilane (HMDS) (10 mmol). This suspension was then refluxed for 24 hrs; the solid was filtered out, washed in triplicate with hexane, and dried overnight under vacuum.

2.2 Aldol Condensation Reaction

The aldol condensation was carried out in screw-cap vials. The catalyst was added to 1.5 mL of hexane to make a suspension containing 0.0117 mmol of amine group. In a separate vessel PNB (.39 mmol) was dissolved in acetone (1.5ml). These two solutions were then stirred together at 60° C for specified times and then cooled on ice to quench the reaction. The catalyst was removed by centrifugation and the yield of products was determined by ^{1}H NMR. The yield was determined based on the formation of the aldol **1** and the α,β-unsaturated carbonyl product **2**.

2.3 Solid-State NMR

Experiments were performed at 9.4 T on a Chemagnetics Infinity 400 Spectrometer equipped with a 5-mm MAS probe operated at 400.00 MHz (^{1}H) and 79.4 MHz (^{29}Si) and at 14.1 T on a Varian NMR System 600 spectrometer equipped with a 1.6-mm FastMAS^{TM} probe operated at 599.6 MHz (^{1}H) and 150.8 MHz (^{13}C). Identification of functional groups, intermediates, and reactant species was performed by ^{13}C cross polarization magic angle spinning (CPMAS) and direct polarization (DPMAS).

2.3.1 Parameters

The experimental parameters will be given below the spectra using the following notions: ν_R denotes the MAS rate, $\nu_{RF}(X)$ is the magnitude of the RF magnetic field at the frequency of X nuclei, τ_{CP} is the mixing time during CP, N_{CPMG} is the number of echoes acquired in Carr-Purcell-Meiboom-Gill (CPMG) experiment, τ_{CPMG} is the corresponding time interval between π pulses, τ_{RD} is the recycle delay, NS is the number of scans, and AT is the total acquisition time.

The chemical shifts of ^{29}Si, ^{13}C and ^{1}H are reported using the δ scale and are secondary referenced to tetramethylsilane (TMS) at 0 ppm.

2.3.2 Loading of Functional Groups

The loading of the functional groups (Table 1) was measured via ^{29}Si NMR using DPMAS experiment with CPMG refocusing [30]. The silicon functionalities found in mesoporous silica materials and their designations are shown in Figure 1. Q sites have

four bonds to oxygen, constituting the basic support structure. The T-sites, D-sites and M-sites are bound to one, two and three organic functional groups, respectively.

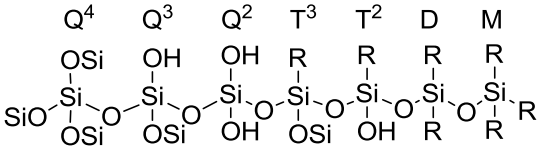

Figure 1. The ^{29}Si site designations for silicate materials, where R is an organic functional group.

Since the resonance frequencies of various silicon sites are known from numerous previous studies [31-33], the ^{29}Si DPMAS spectra (Figure 2) can be reliably deconvolved, even in highly amorphous samples with poorly resolved spectra. The resulting intensities can be used to evaluate the sample composition, which is typically given as $(SiO_2)_{100}(H_2O)_X(ORG)_Y$, where ORG is the functional group (either AP, MAP or DMAP), X is the amount of water in the sample, and Y is the amount of organic functional groups [33]. X and Y can be calculated by using the percentage of each site as:

$$X = \frac{1}{2}Q^3 + Q^2 + \frac{1}{2}T^2$$

$$Y = T^3 + T^2.$$

The molecular weight of the system is given by:

$$MW_{sample} = 100*60.0858 \text{ g/mol} + X*18 \text{ g/mol} + Y*MW_{org}$$

where MW_{org} is the molecular weight of the functional group. The loading of functional groups in mol/g of the sample can then be calculated by dividing the number of

functional sites (Y) by the molecular weight. To calculate the number of silanols in the sample, the amount of water must be doubled (2*X) and divided by the molecular weight. These calculations lead to the results in Table 1.

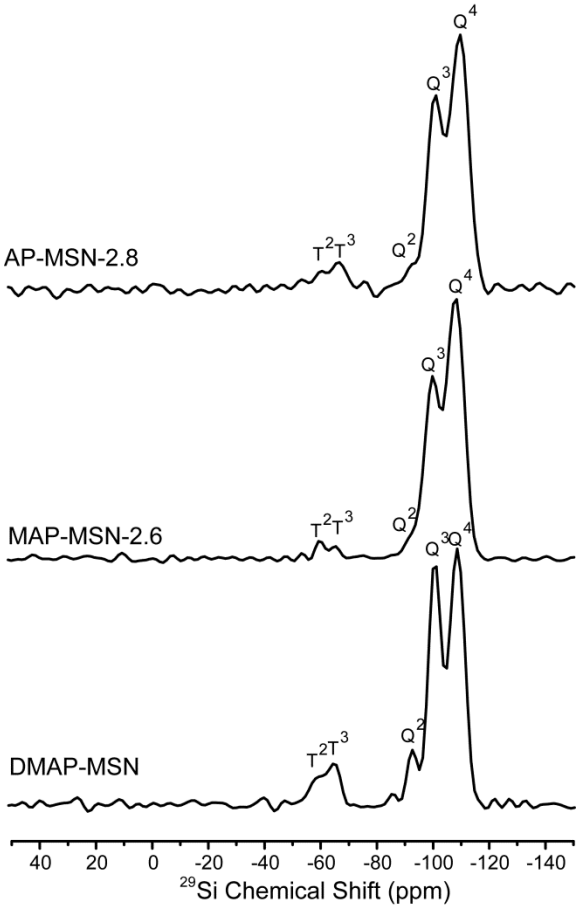

Figure 2. ^{29}Si DPMAS-CPMG spectra of AP-MSN-2.8, MAP-MSN-2.6 and DMAP-MSN obtained on a 400 MHz instrument. Parameters: ν_R = 10 kHz, ν_{RF}^{Si} = 50 kHz, ν_{RF}^{H} = 45 kHz, N_{CPMG} = 10, τ_{RD} = 300s, NS = 296, and AT = 25h. The corresponding spectra of AP-MSN-3.6 and MAP-MSN-3.5 are shown in Figure 10.

2.4 Other Characterization Methods.

The surface areas and pore size distributions were measured by nitrogen sorption isotherms in a Micromeritics Tristar 3000 using the Brunauer-Emmett-Teller (BET) and Barrett-Joyner-Halenda (BJH) calculation methods. The transmission electron microscopy (TEM) data was acquired on a Tecnai G2 F20 electron microscope operating at 200 kV and for the measurement a small amount of powder was sonicated in methanol for 15 min. Elemental analysis was performed in a Perkins Elmer 2100 Series II CHN/S Analyzer, with combustion and reduction temperatures of 925 °C and 640 °C, respectively, and with acetanilide as a calibration standard. A Rigaku Ultima IV diffractometer was used for small angle powder X-ray diffraction studies. The Fourier transform infrared (FT-IR) data was recorded on a Nicolet Nexus 470. A table of the results is shown below (Table 1).

3. Results and Discussion

3.1 Catalytic Activity –AP-MSN

The catalytic activities of 3-aminopropyl mesoporous silica with 2.8 nm pores (AP-MSN-2.8), 3-aminopropyl mesoporous silica with 3.6 nm pores (AP-MSN-3.6) and homogenous propylamine were measured and compared for the aldol condensation reaction between **PNB** and acetone at 60° C in hexane (Figure 3). Davis et al. [22] reported a fourfold activity increase when using an amine-functionalized MSN catalyst versus the homogenous amine catalyst. In the case of AP-MSN-2.8, only 2% conversion was measured after 2 hours, which was less than observed for propylamine (4.5% after 2 hrs). However, the AP-MSN-3.6 catalyst yielded a conversion of 47% in the same

reaction time. The 20-fold increase in the yield observed upon changing the pore size by less than 1 nm may suggest that restricted diffusion was responsible for the poor activity of AP-MSN-2.8. However, the reactants sizes (0.4 nm acetone, 0.6 nm PNB, and ~1 nm for the products) are small in comparison to the pore size, suggesting that other factors may contribute to the activity drop. Indeed, measurement of the reaction kinetics showed a strong inhibition of the reaction at high **PNB** concentrations (Figure 4). This suggests the formation of some type of PNB complex on the substrate that impedes the reaction.

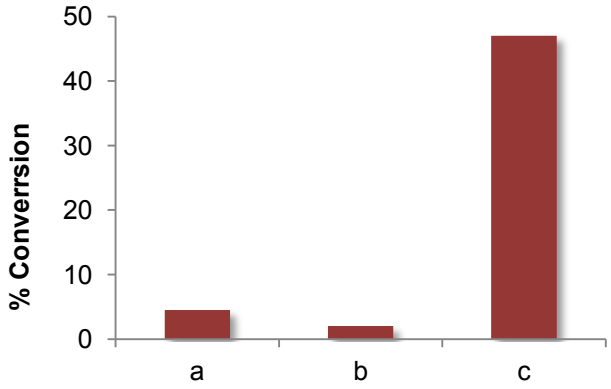

Figure 3. Catalytic activities are compared for: (a) homogeneous propylamine, (b) AP-MSN-2.8, and (c) AP-MSN-3.6.

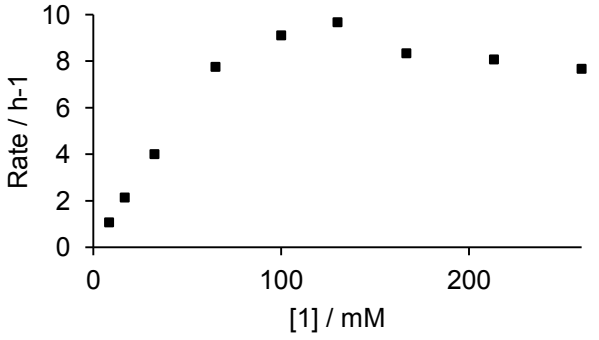

Figure 4. Effect of substrate concentration on the rate of AP-MSN-3.6 catalyzed cross-aldol condensation. The drop in rate at high concentrations of **PNB** suggests substrate inhibition of the reaction.

3.2 Detection of Stable Intermediate

The samples of AP-MSN-2.8 were further examined using a variety of techniques. The surface area and pore size were measured before and after the reaction by nitrogen isotherms. Although the surface area remained relatively constant (906 m^2/g vs. 894 m^2/g), the pore size dropped to 2 nm after reaction. Based on this result, as well as the reaction kinetics, it appears that a stable intermediate may have formed on the surface. It has been suggested that imine formation is possible (Scheme 2) [20], however no evidence of the Schiff base has been previously presented.

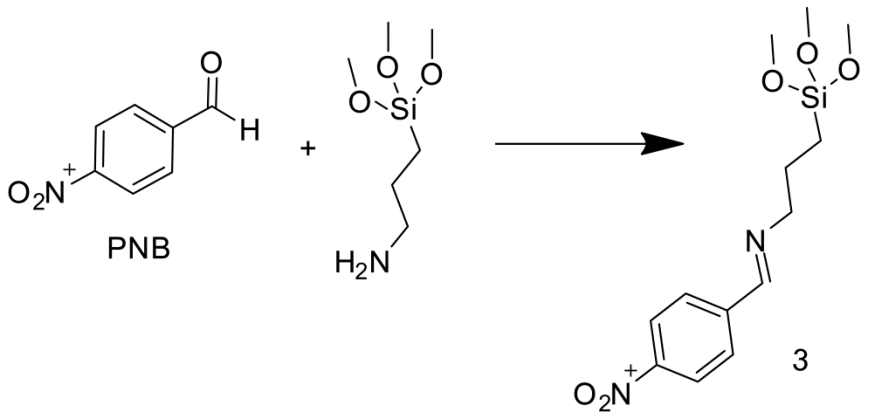

Scheme 2. The formation of an imine intermediate (stable Schiff base) between **PNB** and AP-MSN.

Our studies using SSNMR and infrared spectroscopy demonstrated that a stable imine intermediate indeed formed in AP-MSN catalysts. The ^{13}C CPMAS spectrum of AP-MSN-2.8 (Figure 5a) clearly indicates the presence of the intermediate imine Schiff base with **PNB**. We focus our attention on resonances ‘c’ and ‘d’ in AP-MSN-2.8 catalyst before and after the reaction (AP-MSN-2.8-before and AP-MSN-2.8-after, represented in Figure 5a by black and blue traces, respectively, in Figure 5a). Resonance ‘d’,

corresponding to the C=N carbon, occurs at 160 ppm and is unique to the imine intermediate, i.e. it is found in neither **PNB** nor AP-MSN alone. If the unreacted **PNB** were present after the reaction, a peak at 190 ppm for the carbonyl carbon would occur, which is not observed. Resonance 'c*' is C-3 in the imine intermediate and appears in the 'after' spectrum along with resonance 'c', C-3 in the amine, which has diminished in intensity. The presence of 'c*' and 'd' indicates a chemical transformation, as opposed to physiabsorption of **PNB**, while the presence of 'c' implies there is still some unreacted surface-bound amine left in the system. The infrared spectrum of AP-MSN-2.8 (Figure 5) shows the disappearance of the C=O stretching band of **PNB** (1706 cm^{-1}) and the appearance of a C=N (1646cm^{-1}) stretching band, confirming the findings from SSNMR. Elemental analysis was also used to compare the nitrogen content before and after the reaction, showing that approximately 70% of the surface-bound amines formed an imine, which is in agreement with the ^{13}C CPMAS ratio of 'c' to 'c*'(note, however, that the CPMAS spectrum is not strictly quantative). This imine group not only blocks the reaction sites, but it may also restrict diffusion due to its large size, on the order of 1 nm, explaining the drastic reduction in pore size to 2 nm.

3.3 Structural Modification –MAP-MSN and DMAP-MSN

We have demonstrated above that the formation of a stable imine intermediate in AP-MSN lead to a decrease in aldol activity. Therefore, in an attempt to increase the reaction activity, the AP group (primary amine) was exchanged for the MAP group (secondary modified amine). MAP-MSN should be incapable of forming a stable imine in hexane. Once again, catalysts with two different pore sizes, MAP-MSN-2.6 and MAP-MSN-3.5, were synthesized, yielding 2 hr conversions of 93% and 97%, respectively. In

this case no intermediate was measured after the reaction took place in hexane, as verified by SSNMR and infrared spectroscopies. No inhibition of the reaction kinetics was observed, and the rate constants were over 3 times larger than in the AP-MSN case.

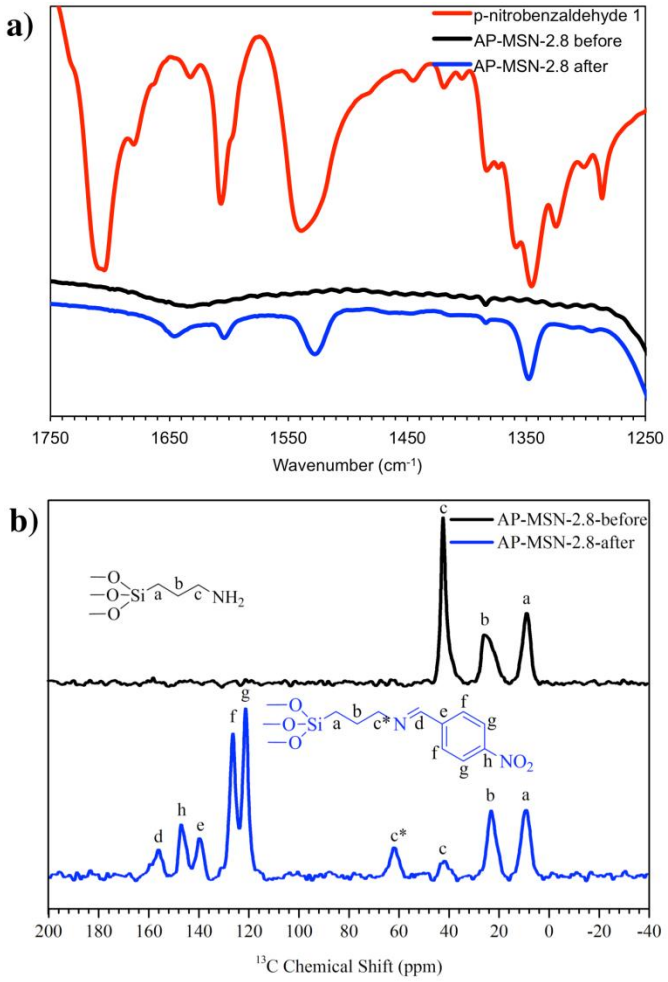

Figure 5. Infrared (a) and ^{13}C CPMAS NMR (b) spectra of AP-MSN-2.8 before (black) and after (blue) reaction with **PNB**. SSNMR parameters ν_R = 40 kHz, $\nu_{RF}(^{13}C)$ = 140 kHz, $\nu_{RF}(^{1}H)$ during CP = 60 kHz, $\nu_{RF}(^{1}H)$ during SPINAL-64 decoupling = 12 kHz, τ_{CP} = 3 ms, τ_{RD} = 2 s, NS = 26,400, and AT = 15 hrs. Infrared spectrum of **PNB** (red) is included as a reference. The formation of intermediate **3** is shown.

It is important to note that MAP-MSN is also more basic than the AP-MSN, and one mechanism by which aldol formation occurs is the enolate pathway under basic conditions. In order to test if the reaction was in fact being catalyzed by the enolate pathway, instead of the proposed enamine pathway, DMAP-MSN was synthesized and reacted under similar conditions. DMAP was chosen for its high pH and the unavailability of the enamine pathway. This reaction was not catalyzed, thereby showing that under these conditions the reaction does not proceed by enolation.

3.4 Solvent Effects

It is well known that the choice of solvents can play a large role in homogenous catalysis [34-36], whereas much less effort has been dedicated toward understanding of the involvement of solvents in heterogeneously catalyzed reactions [26,37]. The reactions described in the previous sections all used hexane as a solvent, leading to the formation of a stable imine intermediate in AP-MSN. We also found that this intermediate could regenerate the primary amine upon treatment with dilute HCl. This led to the concept that using water as a solvent may increase the activity of AP-MSN by no longer forming the inhibiting intermediate species.

AP-MSN-3.6 and MAP-MSN-3.5 were chosen to test this hypothesis. In AP-MSN-3.6, the conversion was nearly quantative within an hour and the rate constant increased 10-fold. In contrast, MAP-MSN-3.5 showed a 10-fold drop in the apparent rate constant. The possible causes of this dramatic reversal in behavior are further investigated below.

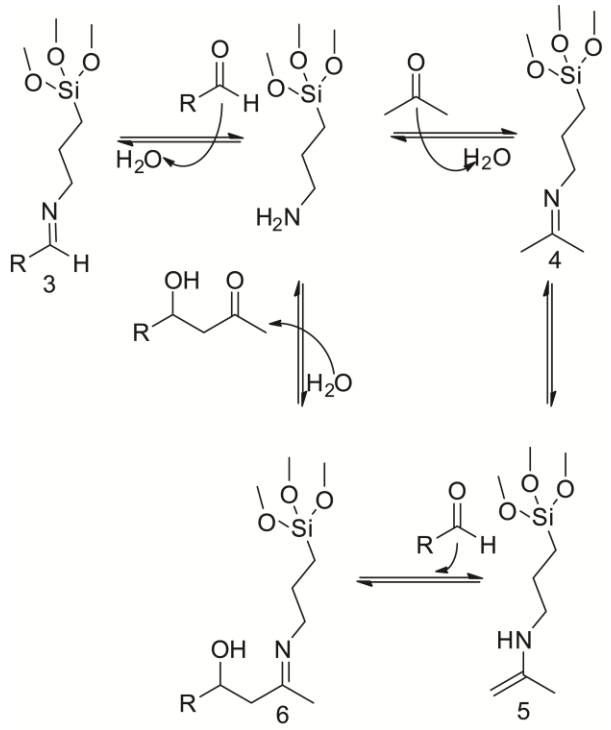

Scheme 3. Proposed aldol condensation cycle catalyzed by AP-MSN. R = *p*-nitrophenyl

3.4.1 Effects of Solvents on Equilibrium

In AP-MSN-3.6 in hexane, the reaction was inhibited by the formation of a stable Schiff-base; however, in the aqueous solution this Schiff-base may no longer be the favored intermediate. Scheme 3 shows that AP-MSN is capable of forming two different intermediates, **3** or **4**, in presence of acetone and **PNB**. We previously showed the formation of **3** via SSNMR, however **4** was not observed in the spectrum in hexane. To increase the sensitivity, ^{13}C enriched acetone was introduced to AP-MSN-3.6 in hexane and the formation of **4** was observed (Figure 6), in accordance with previously reported chemical shifts in similar compounds [38-39]. In a similar sample prepared with unlabeled acetone the presence of **4** was also detected, allowing the change in chemical shift of the functional group to be shown as well, confirming a chemical interaction

between acetone and catalytic sites. Water may play a role in the equilibrium shift to favor **4**, therefore leading to a higher conversion factor. The product distribution can provide insight into the reaction pathway equilibrium. According to Scheme 3, if the reaction takes place via **4**, the main product should be aldol **1**, which was indeed observed. In fact, the formation of **2** appears to occur sequentially after the formation of **1**, leading to the conclusion that formation of **2** occurs from the dehydration of **1**, as opposed to an alternate pathway.

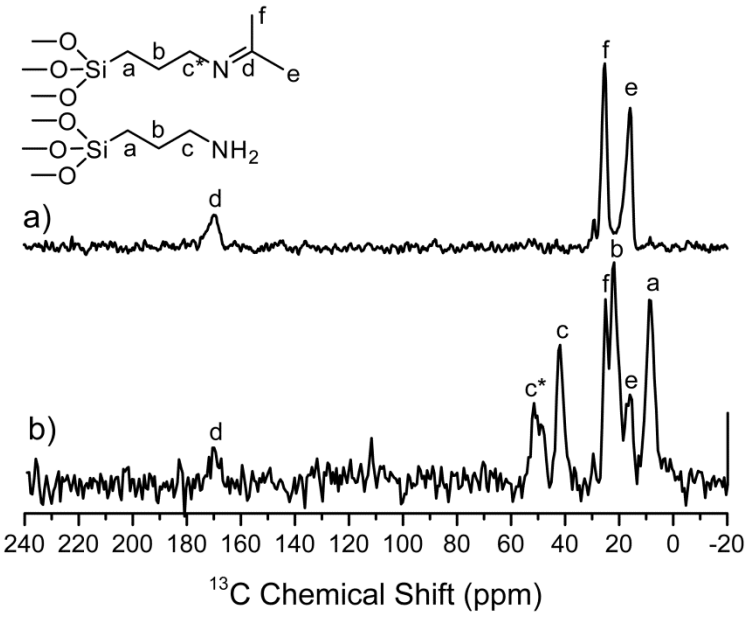

Figure 6. ^{13}C CPMAS SSNMR spectra of intermediate **4** in AP-MSN sample prepared in the hexane solution. The top spectrum (a) is ^{13}C isotope enriched acetone on AP-MSN-3.6 and the bottom spectrum (b) is natural abundance acetone with AP-MSN-3.6. The resonances c*, d, e and f are consistent with the existence of intermediate **4**. ^{13}C CPMAS Parameters ν_R = 40 kHz, $\nu_{RF}(^{13}C)$ = 62 kHz, $\nu_{RF}(^{1}H)$ during CP = 102 kHz, $\nu_{RF}(^{1}H)$

during SPINAL-64 decoupling = 12 kHz, τ_{CP} = 2 ms, τ_{RD} = 3 s, NS = 64 (a) and 10240 (b), and AT = 3 min (a) and 8.7 hrs (b).

Although MAP-MSN-3.5 in hexane did not form the inhibiting imine group; in aqueous solution the formation of a stable cationic iminium, intermediate **7**, is possible (Scheme 4). This intermediate would behave similarly to the inhibiting imine in AP-MSN, blocking the reaction sites and constraining diffusion in the pore. Previous studies reported the formation of iminium intermediates when secondary amines were used as catalysts for the aldol reaction [40-44]. Unfortunately the confirmation of **7** was not possible using our spectroscopic techniques, presumably due to the short lifetimes and relative instability of iminium intermediates.

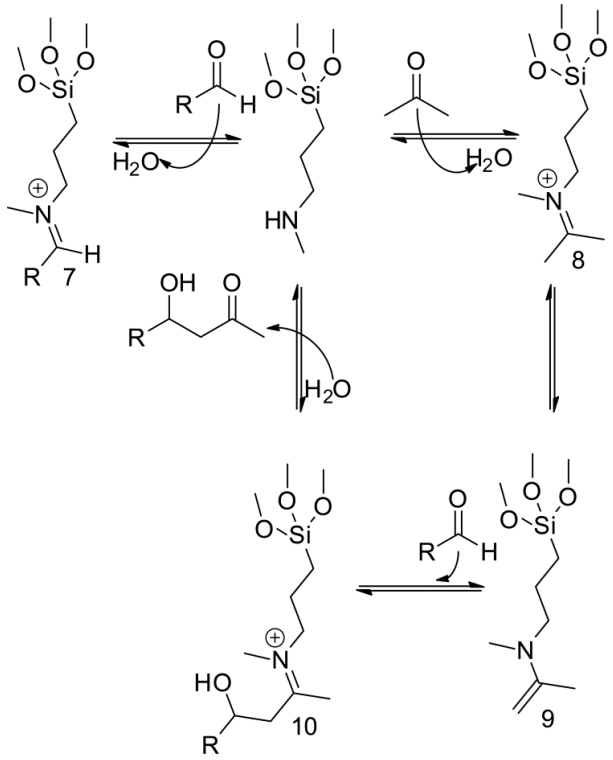

Scheme 4. Proposed aldol condensation cycle catalyzed by MAP-MSN in water. R = *p*-nitrophenyl.

3.4.2 Acidity

Water, a weak acid, may assist the reaction by hydrogen bonding with the carbonyl oxygen. The effect of solvent acidity was tested by measurement of the reaction activity in methanol, which has a very similar pKa to water. Both AP-MSN-3.6 and MAP-MSN-3.5 were slower to catalyze in methanol than in water or in aprotic acetonitrile (Figure 7). This implies that acidity was detrimental to the overall reaction, as opposed to being supportive.

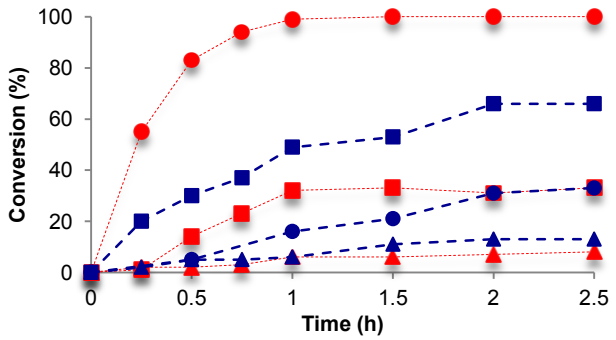

Figure 7. Effect of protic solvents on the rates of aldol reaction catalyzed by AP-MSN (red) and MAP-MSN (blue): water (circles) and methanol (triangles). The rate in polar aprotic acetonitrile (squares) is shown as a reference.

3.4.3 Polarity

The reaction kinetics in hexane and water were compared with those in dichloromethane (low polarity) and aprotic acetonitrile (polar) to examine the effect of solvent polarity on the reaction. In both AP-MSN-3.6 and MAP-MSN-3.5 the activity decreased with increasing polarity, with the exception of water (Figure 8). This implies that the polarity of water does not contribute to the increased activity; it should instead inhibit the reaction. This trend is similar to that found by Davis and coworkers, who

reported a decrease in reactivity of bifunctionalized material due to acid-base neutralization of the functional groups in polar solvents [22]. Neutralization of the surface-bound amine may occur in the system from interaction with nearby acidic silanols in polar solvents. The interaction between silanols and functional groups will be further investigated in the next section.

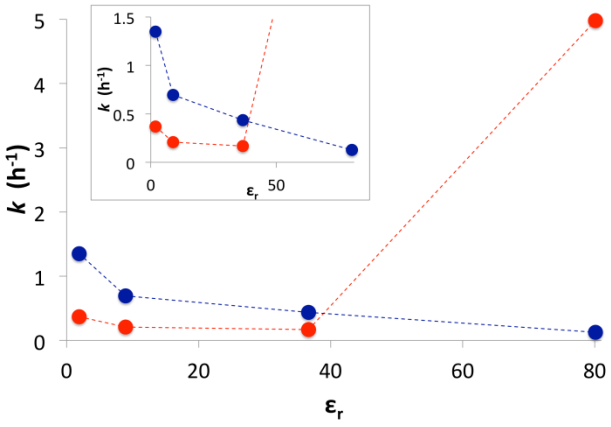

Figure 8. Rates of aldol reaction catalyzed by AP-MSN (red) and MAP-MSN (blue) in solvents of increasing dielectric constants: hexane ($\varepsilon_r = 1.89$), dichloromethane ($\varepsilon_r = 8.93$), acetonitrile ($\varepsilon_r = 36.64$) and water ($\varepsilon_r = 80.1$) [45]. Inset: same graph with the x-axis cut at 1.5 h^{-1} to show the details of the lower reaction rates.

3.5 Cooperative Effect of Silanol

The aldol reaction catalyzed by heterogeneous amine MSN catalysts had higher activity than the homogenous catalyst, with the exception of AP-MSN-2.8 in hexane. One explanation for the increased activity could be the cooperative role of the support. Previous research has shown that acidic secondary groups on the surface have lead to an increase in the overall reaction efficiency [20,22-24]. Acidic surface silanols have been shown to interact noncovalently with functionalized amines [46], and to participate in the

aldol condensation in a variety of organic solvents [28,47-52]. The ^{29}Si DPMAS spectra (Figure 2) confirm the presence of silanol groups on the surface, with the loadings given in Table 1.

The interaction of the reactant, acetone, with the silanols was examined by introducing ^{13}C enriched acetone to non-functionalized MSN. Carbonyl compounds are known to form hydrogen bonds with silica surfaces [23,53-58]. The ^{13}C DPMAS spectrum of enriched acetone on non-functionalized MSN (Figure 9), exhibits a resonance at 213 ppm for the carbonyl peak, which is shifted downfield in comparison to neat acetone (206 ppm). This downfield shift has previously been reported as an indication of hydrogen bonding with the silica surface [53,57-59]. The hydrogen bonding of reactants was further examined by addition of DMSO (a hydrogen bond acceptor) to the reaction of MAP-MSN-3.5 in hexane. The yield decreased from 97% to 55%, presumably due to the competition between DMSO and the reactants for hydrogen bonding surface sites. Hydrogen bonding may play two important roles: bringing the reactants in close proximity to the catalytic sites and contributing to the activation of nucleophilic attack. In the Zimmerman-Traxler model (Scheme 5) the silanol groups may assist by aligning the acetone and amine groups in a six-membered ring-like arrangement [60-61].

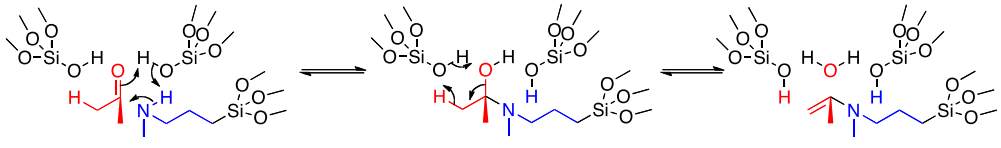

Scheme 5. Possible pathway of proton transfer assisted by silanol groups, the Zimmerman-Traxler model.

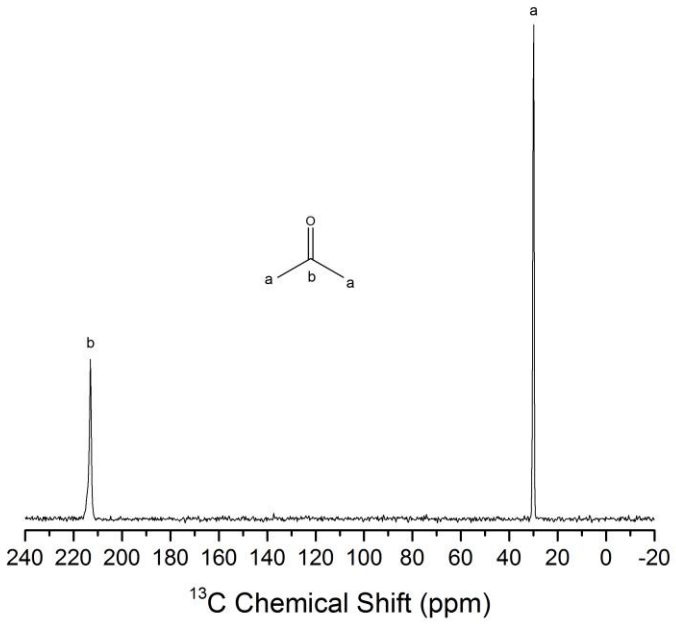

Figure 9. ^{13}C DPMAS spectrum of non-functionalized MSN w/^{13}C enriched acetone. The carbonyl carbon resonates downfield from neat acetone (~213 vs. 206 ppm), which indicates a hydrogen-bond between acetone and surface silanols. Parameters: ν_R = 40 kHz, ν_{RF}^{C} = 100 kHz, ν_{RF}^{H} for spinal decoupling = 12 kHz, τ_{RD} = 3 s, NS = 16, and AT ~ 1.3 min.

To examine the participation of silanol groups in the catalytic activity of AP-MSN-3.6 and MAP-MSN-3.5, both catalysts were treated with hexamethyldisilazane (HMDS) to cap the surface silanols. The number of silanols in the samples before and after treatment was measured via ^{29}Si NMR (Figure 10). In MAP-MSN-3.5 the number of silanols was reduced by 39% and the yield of the reaction in hexane dropped by 34%. In AP-MSN-3.6 the number of silanols decreased by 34%, and the reaction had a 10 time lower yield compared to the non-treated sample in water. The decrease in activity upon

silaytion shows that the silanol cooperative effect plays an important role in both solvents.

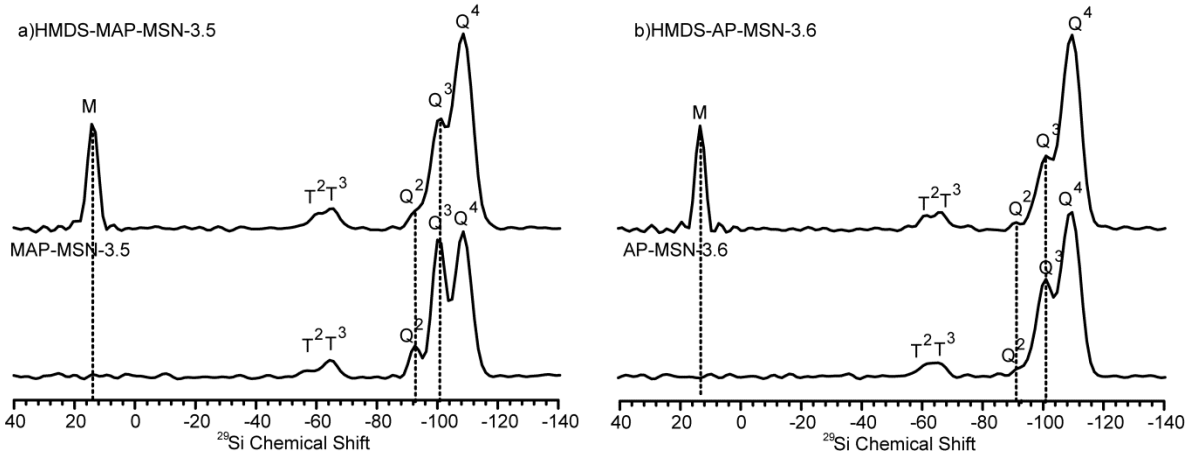

Figure 10. ^{29}Si DPMAS spectra of a) MAP-MSN-3.5 and b) AP-MSN-3.6 before (bottom) and after (top) blocking silanol groups with HMDS. Appearance of M sites due to the attached silane matches the decrease in the intensity of the Q_2 and Q_3 sites of the blocked groups. [62] Parameters: ν_R = 10 kHz, ν_{RF}^{Si} = 50 kHz, ν_{RF}^{H} = 45 kHz, N_{CPMG} = 10, τ_{RD} = 300s, NS = 296, and AT = 25h

The coopertivity of silanols in hexane was further investigated in MAP-MSN-3.5. To this end, non-functionalized MSN was added to homogenous N-methyl-propylamine and used to catalyze the reaction, leading to an increase in conversion, 51 %, compared to 10% without the MSN. A comparison of the effect of silanols and proximity can be seen in Figure 11, which shows an activity trend: MAP<MAP+MSN<MAP-MSN. This trend indicates that the proximity of the silanols to the catalyst is crucial. The proximity of the amine functional group and surface silanols has been previously discussed to be of importance in bringing the reactants together [46].

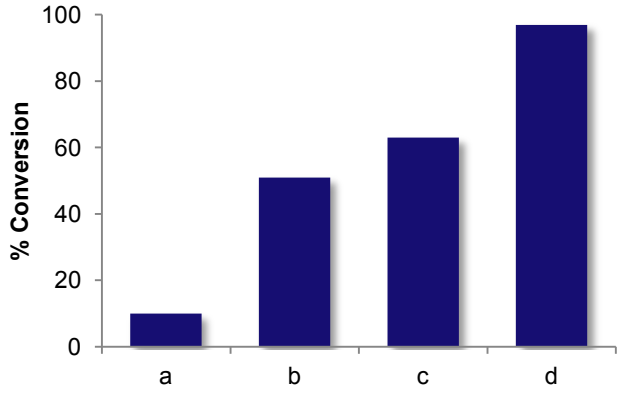

Figure 11. Effect of proximity between silanol and amine groups on the conversion of **PNB**. Catalytic activities are compared for: (a) homogeneous N-methyl-propylamine, (b) homogeneous N-methyl-propylamine + non-functionalized MSN, (c) silanol-passivated HMDS-MAP-MSN-3.5, and (d) heterogeneous MAP-MSN-3.5.

The surface silanols may offer another added benefit. Earlier it was mentioned that the aldol reaction may take place via the enolation pathway in basic conditions. The acidity of the silanols acts as a buffer to decrease the overall basicisty of the system, thereby allowing the enamine pathway. The pH values of the suspensions of AP-MSN-3.6 and MAP-MSN-3.5 in water were, 8.1 and 8.3, respectively, much more acidic than the free amines in water (pH>11).

4. Conclusion

In this study the aldol-condensation between *p*-nitrobenzaldehyde and acetone was examined in the presence of heterogeneous amine catalysts consisting of MSN

supports with varying pore sizes functionalized with primary and secondary amines (AP-MSN and MAP-MSN).

The low catalytic yield of AP-MSN in hexane was determined to be caused by the formation of a stable intermediate, shown spectroscopically by SSNMR for the first time, which blocked the catalytic sites and hindered molecular diffusion within the pores. The catalytic activity could be improved by chemically altering the primary amine to a secondary amine, MAP-MSN, thereby inhibiting the formation of a Schiff base, or by switching the solvent to water. The addition of water increased the activity of AP-MSN a factor of 10, but decreased the activity in MAP-MSN. This decrease may be due to the formation of an iminium intermediate on the surface. The increased activity of AP-MSN in water may be explained by a change in equilibrium of the formed intermediates.

The surface silanols were shown to assist the reaction in both hexane and water, leading to higher conversion rates compared to corresponding homogenously catalyzed reactions. The surface silanols boost activity by bringing the reactants near the amine catalysts, preparing the carbonyls for nucleophic attack, and acting as a buffer.

This chapter underlines the importance of mechanistic studies to improve the activity of catalyst in reactions. With an understanding of the environmental effects and the intrinsic behavior of the catalyst a rational design of the catalyst was accomplished, yielding a more active catalyst. An important next step would be to determine what effect, if any, the pore size and solvent choice have on diffusion.

5. Acknowledgment

This research was supported at the Ames Laboratory by the U.S. Department of Energy, Office of Basic Energy Sciences. Ames Laboratory is operated for the U.S. Department of Energy by Iowa State University under Contract No.DE-AC02-07CH11358.

6. References

[1] A. Corma, and H. Garcia, Topics in Catalysis 48 (2008) 8-31.

[2] F. Rodríguez-Reinoso, Carbon 36 (1998) 159-175.

[3] X. Yu, X. Yu, S. Wu, B. Liu, H. Liu, J. Guan, and Q. Kan, Journal of Solid State Chemistry 184 (2011) 289-295.

[4] C.M.A. Parlett, D.W. Bruce, N.S. Hondow, A.F. Lee, and K. Wilson, ACS Catalysis (2011) 636-640.

[5] J.N. Stuecker, J.E. Miller, R.E. Ferrizz, J.E. Mudd, and J. Cesarano, Industrial & Engineering Chemistry Research 43 (2003) 51-55.

[6] H. Hattori, Chemical Reviews 95 (1995) 537-558.

[7] K.K. Rao, M. Gravelle, J.S. Valente, and F. Figueras, Journal of Catalysis 173 (1998) 115-121.

[8] H. Matsuhashi, H. Miyazaki, Y. Kawamura, H. Nakamura, and K. Arata, Chemistry of Materials 13 (2001) 3038-3042.

[9] D. Tichit, B. Coq, S. Cerneaux, and R. Durand, Catalysis Today 75 (2002) 197-202.

[10] T.R. Gaydhankar, P.N. Joshi, P. Kalita, and R. Kumar, Journal of Molecular Catalysis A: Chemical 265 (2007) 306-315.

[11] M. Chatterjee, K. Matsushima, Y. Ikushima, M. Sato, T. Yokoyama, H. Kawanami, and T. Suzuki, Green Chemistry 12 (2010) 779-782.

[12] S. Mukherjee, J.W. Yang, S. Hoffmann, and B. List, Chemical Reviews 107 (2007) 5471-5569.

[13] B. List, R.A. Lerner, and C.F. Barbas III, Journal of the American Chemical Society 122 (2000) 2395-2396.

[14] S.M. Dean, W.A. Greenberg, and C.-H. Wong, Advanced Synthesis & Catalysis 349 (2007) 1308-1320.

[15] Sujandi, S.-E. Park, D.-S. Han, S.-C. Han, M.-J. Jin, and T. Ohsuna, Chemical Communications (2006) 4131-4133.

[16] S. Luo, J. Li, L. Zhang, H. Xu, and J.-P. Cheng, Chemistry – A European Journal 14 (2008) 1273-1281.

[17] S. Luo, X. Zheng, and J.-P. Cheng, Chemical Communications (2008) 5719-5721.

[18] T.M. Suzuki, M. Yamamoto, K. Fukumoto, Y. Akimoto, and K. Yano, Journal of Catalysis 251 (2007) 249-257.

[19] K.K. Sharma, and T. Asefa, Angewandte Chemie 119 (2007) 2937-2940.

[20] S. Shylesh, A. Wagner, A. Seifert, S. Ernst, and W.R. Thiel, Chemistry – A European Journal 15 (2009) 7052-7062.

[21] B. Liu, S. Wu, X. Yu, J. Guan, and Q. Kan, Journal of Colloid and Interface Science 362 (2011) 625-628.

[22] R.K. Zeidan, S.-J. Hwang, and M.E. Davis, Angewandte Chemie International Edition 45 (2006) 6332-6335.

[23] M. Wiesner, G.g. Upert, G. Angelici, and H. Wennemers, Journal of the American Chemical Society 132 (2009) 6-7.

[24] D.E. Purich, Enzyme Kinetics: Catalysis and Control, Elsevier, 2002.

[25] N. Solin, L. Han, S. Che, and O. Terasaki, Catalysis Communications 10 (2009) 1386-1389.

[26] C. Reichardt, and T. Welton, Solvent Effects on the Rates of Homogeneous Chemical Reactions, Solvents and Solvent Effects in Organic Chemistry, Wiley-VCH Verlag GmbH & Co. KGaA, 2010, pp. 165-357.

[27] I.I. Slowing, B.G. Trewyn, and V.S.Y. Lin, Journal of the American Chemical Society 129 (2007) 8845-8849.

[28] K. Kandel, S.M. Althaus, C. Peeraphatdit, T. Kobayashi, B.G. Trewyn, M. Pruski, and I.I. Slowing, Journal of Catalysis 291 (2012) 63-68.

[29] K. Kandel, S.M. Althaus, C. Peeraphatdit, T. Kobayashi, B.G. Trewyn, M. Pruski, and I.I. Slowing, ACS Catalysis 3 (2013) 265-271.

[30] S. Meiboom, and D. Gill, Review of Scientific Instruments 29 (1958) 688-691.

[31] H.C. Marsmann, Silicon-29 Nmr, Emagres, John Wiley & Sons, Ltd, 2007.

[32] G. Engelhardt, Silicon-29 Nmr of Solid Silicates, Emagres, John Wiley & Sons, Ltd, 2007.

[33] J.W. Wiench, V.S.-Y. Lin, and M. Pruski, Journal of Magnetic Resonance 193 (2008) 233-242.

[34] T. Nguyen Minh, and T.K. Ha, Journal of the American Chemical Society 106 (1984) 599-602.

[35] O. Acevedo, and W.L. Jorgensen, Chapter 14 Solvent Effects on Organic Reactions from Qm/Mm Simulations. in: C.S. David, (Ed.), Annual Reports in Computational Chemistry, Elsevier, 2006, pp. 263-278.

[36] C. Reichardt, Organic Process Research & Development 11 (2006) 105-113.

[37] C. D'Agostino, G.L. Brett, P.J. Miedziak, D.W. Knight, G.J. Hutchings, L.F. Gladden, and M.D. Mantle, Chemistry – A European Journal 18 (2012) 14426-14433.

[38] N. Naulet, M.L. Filleux, G.J. Martin, and J. Pornet, Organic Magnetic Resonance 7 (1975) 326-330.

[39] N. Naulet, and G.J. Martin, Tetrahedron Letters 20 (1979) 1493-1496.

[40] A. Erkkilä, I. Majander, and P.M. Pihko, Chemical Reviews 107 (2007) 5416-5470.

[41] B. List, Accounts of Chemical Research 37 (2004) 548-557.

[42] C. Allemann, R. Gordillo, F.R. Clemente, P.H.-Y. Cheong, and K.N. Houk, Accounts of Chemical Research 37 (2004) 558-569.

[43] W. Notz, F. Tanaka, and C.F. Barbas, Accounts of Chemical Research 37 (2004) 580-591.

[44] J. Brazier, and N. Tomkinson, Secondary and Primary Amine Catalysts for Iminium Catalysis
Asymmetric Organocatalysis. in: B. List, (Ed.), Springer Berlin / Heidelberg, 2009, pp. 281-347.

[45] Crc Handbook of Chemistry and Physics, CRC Press, Boca Raton, FL, 2012.

[46] S. Nedd, T. Kobayashi, C.-H. Tsai, I.I. Slowing, M. Pruski, and M.S. Gordon, The Journal of Physical Chemistry C 115 (2011) 16333-16339.

[47] Q. Wang, and D.F. Shantz, Journal of Catalysis 271 (2010) 170-177.

[48] Y. Kubota, H. Yamaguchi, T. Yamada, S. Inagaki, Y. Sugi, and T. Tatsumi, Topics in Catalysis 53 (2010) 492-499.

[49] J.D. Bass, A. Solovyov, A.J. Pascall, and A. Katz, Journal of the American Chemical Society 128 (2006) 3737-3747.

[50] N.A. Brunelli, K. Venkatasubbaiah, and C.W. Jones, Chemistry of Materials 24 (2012) 2433-2442.

[51] Y. Kubota, K. Goto, S. Miyata, Y. Goto, Y. Fukushima, and Y. Sugi, Chemistry Letters 32 (2003) 234-235.

[52] S.L. Hruby, and B.H. Shanks, Journal of Catalysis 263 (2009) 181-188.

[53] V.H. Pan, T. Tao, J.-W. Zhou, and G.E. Maciel, The Journal of Physical Chemistry B 103 (1999) 6930-6943.

[54] M.I. Zaki, M.A. Hasan, F.A. Al-Sagheer, and L. Pasupulety, Langmuir 16 (1999) 430-436.

[55] J.H. Drese, A.D. Talley, and C.W. Jones, ChemSusChem 4 (2011) 379-385.

[56] V.Y. Borovkov, A.V. Zaiko, V.B. Kazansky, and W.K. Hall, Journal of Catalysis 75 (1982) 219-224.

[57] I.D. Gay, The Journal of Physical Chemistry 78 (1974) 38-42.

[58] T. Bernstein, D. Michel, H. Pfeifer, and P. Fink, Journal of Colloid and Interface Science 84 (1981) 310-317.

[59] V.Y. Borovkov, A.V. Zaiko, V.B. Kazansky, and W.K. Hall, Journal of Catalysis 75 (1981) 219-224.

[60] H.E. Zimmerman, and M.D. Traxler, Journal of the American Chemical Society 79 (1957) 1920-1923.

[61] S. Bahmanyar, and K.N. Houk, Journal of the American Chemical Society 123 (2001) 11273-11283.

[62] D.W. Sindorf, and G.E. Maciel, Journal of Physical Chemistry 87 (1983) 5516-5521.

Table 1. Structural properties of amine-functionalized mesoporous silica nanoparticle catalysts

Catalyst	S_{BET} (m_2/g)[a]	V_p (cm_3/g)[a]	W_{BJH} (Å)[a]	Amount of organic groups: Elemental analysis (mmol/g)	Amount of organic groups: ^{29}Si NMR evaluation (mmol/g)[b]	SiOH loading: ^{29}Si NMR evaluation (mmol/g)[b]
AP-MSN-2.8	906	1.0	2.8	1.01	1.13	6.8
AP-MSN-2.8 after reaction	894	0.76	2.0	1.70		
AP-MSN-3.6	807	1.2	3.6	1.08	0.98	6.8
HMDS-AP-MSN-3.6						4.6
MAP-MSN-2.6	1008	1.1	2.6	0.50	0.54	6.8
MAP-MSN-3.5	937	1.3	3.5	1.14	0.88	7.5
HMDS-MAP-MSN-3.5	745	1.0	3.3			4.6
DMAP-MSN	673	0.9	3.2	1.29	1.4	7.6

[a] The BET surface area (S_{BET}), the mesopore volume (V_p), and the mean mesopore widths (W_{BJH}) were obtained from the nitrogen sorption analysis. [b] The amounts of organic functional groups incorporated to the silica materials were determined by elemental analysis and further evaluated from the ^{29}Si DPMAS NMR spectra.

CHAPTER 5: DIFFUSION OF HEXANE AND WATER IN TWO DIFFERENT PORE SIZED AP-MSNS MEASURED BY SSNMR: AN EXPLORATORY INVESTIGATION

Stacey Althaus[‡†] *and Marek Pruski*[‡†]

[‡] *U.S. DOE Ames Laboratory, Ames, IA 50011-3020, USA*

[†]*Department of Chemistry, Iowa State University, Ames, IA 50011-3020, USA*

Abstract

The previous chapter described the aldol reaction in amine functionalized mesoporous silica nanoparticles (MSNs) of different pore sizes and with different solvents. In this chapter, solid state NMR, specifically ^{1}H stimulated echo with pulsed field gradient (PFG), will be used to determine the diffusion of two solvents, hexane and water, in MSNs with pore diameters of 2.7 and 3.7 nm functionalized with 3-aminopropyl trimethoxysilane catalysts (referred to as AP-MSN-2.7 and AP-MSN-3.7, respectively). The PFG data were analyzed using a single effective diffusion coefficient and a bi-exponential model. This leads to a clear dependence of the diffusion coefficient on the pore size when hexane is the solvent. In water no significant difference was measured in the diffusion between AP-MSN-2.7 and AP-MSN-3.7 and it is therefore still unclear the role water diffusion plays in this system.

1. Introduction

In the previous chapter, heterogeneous aminopropyl mesoporous silica nanoparticle (AP-MSN) catalysts were examined through a combination of synthetic and characterization techniques. The formation of a stable intermediate Schiff base in hexane caused a decrease in the activity of the primary functionalized amine [1]. This lower activity could be attributed to two different factors, the blocking of the active catalytic sites and the obstruction of diffusion within the pore. When the solvent was changed to water the activity increased dramatically [2]. This change was partially due to the change in affinity toward forming the Schiff base, but may also have contributions from the diffusion properties of water. In this chapter we will delve into the diffusion matter in more depth.

The behavior of reactants and solvents in the pores is still not well understood. It is currently assumed that the reactants and products enter and exit the pores with little steric hindrance. This assumption may be valid in larger pore systems, but becomes problematic in systems with small pores and/or large molecules. In order to understand this process, a number of studies have been undertaken to examine the diffusion of gases and solvents in confined geometries [3-15].

The combination of spin echo sequences [16] with pulsed field gradients (PFG) for the measurement of diffusion processes has been used for many decades [3-4,17-18]. Initially the self-diffusion coefficient was measured in liquids [19] and in crystalline materials, however for the past three decades the diffusivity has also been studied in solids, such as zeolites [6-7] and mesoporous particles [8-15]. In the porous solids it has

been shown that the self-diffusion coefficient of the solvent can depend on a number of factors including, material size [7], solvent concentration [9-11], temperature [12-13], and pressure [14]. Work has also been done to show that the diffusion of different solvents can affect the overall catalytic activity [20-22].

A major complicating factor in the measurement of diffusion in heterogeneous materials is the presence of multiple diffusion coefficients within one sample, often for the same species. For example, these systems may exhibit both inter-particle and intra-particle diffusion, but other groups have shown that the diffusion can also occur in micro cracks in the pore support [5,23-24]. Due to technical limitations set by the gradient strength, particles may leave the pore before a significant measurement can be made, making the separation of an intra-particle diffusion coefficient particularly complicated. As shown in other reports [25], at very short times the molecule may not travel far enough for collision with the wall to take place, and the measured coefficient resembles bulk diffusion. At long time scales the particle is able to travel in and out of the pore multiple times and therefore behaves similarly to the diffusion at infinite time. The intermediate time scale will be a mix of these conditions, but separating all the components is no trivial task.

Previously published research has shown the usefulness of bi-exponential (or multi-exponential) fitting methods of diffusion data in heterogeneous systems [7,15,23,26-29]. These methods use the probabilities of particle presence in locations characterized by different diffusion coefficients. They were first shown to work for the separation of diffusion coefficients in zeolites [7], but since have been used in a variety of other cases including metal organic framework (MOFS) [29], MCM-41[9,15], and other

heterogeneous systems [23,27]. One potential problem with this model is the fitting of many parameters, which lends itself to a large margin of error.

Another method for the observation of restricted diffusion is the time-dependence measurement of the so-called effective self diffusion coefficient, D_{eff}, also referred to as the apparent diffusion coefficient [8,28,30]. In this case only a single exponential curve is fit to the measured gradient echo data points. The change in D_{eff} with time can lead to understanding of restricted diffusion in materials with different pore sizes. Previous studies have used D_{eff} to examine the behavior of solvents and gases in porous glass beads [25], MCM-41 mesoporous silica [8], and a variety of other heterogeneous media [21-22].

In this study hexane and water were chosen as solvents based on the previous reported catalytic data [1-2]. The diffusion of these solvents in AP-MSN-2.7 and AP-MSN-3.7 is studied via STE-PFG. The effective self diffusion coefficients are compared, along with the overall time dependence of the measured diffusion. The bi-exponential model is also used in hexane to compare the inter-particle and intra-particle diffusion, confirming the effective diffusion measurement results.

2. Materials and Methods

2.1.1 Diffusion Measurements

The spin echo was discovered in 1950 by Erwin Hahn [16]. The addition of pulsed field gradients (PFG) allowed for the measurement of self-diffusion coefficients [18]. The stimulated echo pulse sequence (PFG-STE), Figure 1, was chosen because of its insensitivity to T_2 relaxation, which can be exceedingly fast in solids [31]. In this

sequence, a π/2 pulse is first used to flip magnetization into the x-y plane. A gradient field is then applied to the spins, which, in effect, encodes the spin location. A π/2 pulse with opposite phase is applied again to the spins, to realign their magnetization with the z axis, where it remains stored for a period of time before being flipped once more to the x-y plane by a third π/2 pulse. Subsequently, a gradient pulse of the same length and strength as the first one is applied. If the spin is the same location throughout the sequence, its magnetization is completely refocused by this pulse sequence producing the so-called spin echo. If the spin has changed its original location due to diffusion, the second gradient will not 'unwind' the dephasing of magnetization produced by the first gradient, causing attenuation of the echo signal.

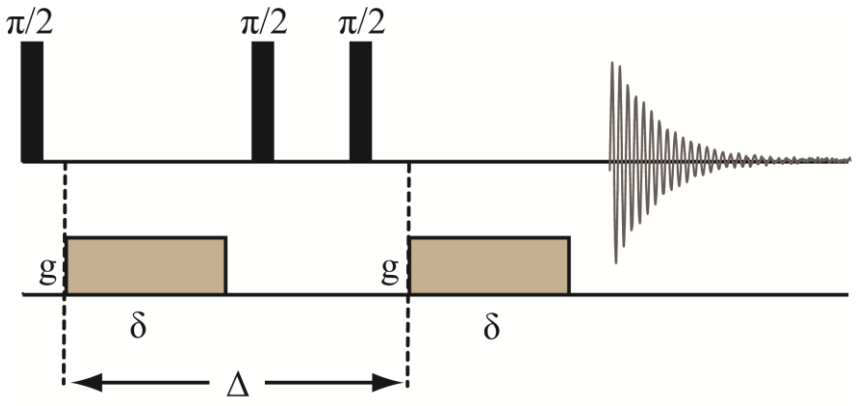

Figure 1. The stimulated echo with pulsed field gradients (STE- PFG) pulse sequence.

This attenuated signal intensity, I_g, can be used to calculate the self-diffusion coefficient, D, as:

$$I_g = I_0 e^{-Dg^2\gamma^2\delta^2(\Delta-\frac{\delta}{3})} = I_0 e^{-Dg^2\gamma^2\delta^2 t_{eff}} \quad (1)$$

where I_0 is the initial intensity, g is the gradient strength, γ is the gyromagnetic ratio, δ is the length of the gradient pulse, Δ is the interval between gradient pulses, and t_{eff} is the effective time constant. By altering the strength of the gradient pulse, data points can be acquired which can then be fit with an exponential curve. This data was collected and the results were examined using two different fitting models.

2.1.2 Effective Diffusion Fitting Model

The studied heterogeneous system is expected to show restricted diffusion, which should manifest in a change of the effective self-diffusion coefficient, D_{eff}, with time [8]. In order to investigate this, multiple values of Δ were used, with a set of data points being collected with changing gradient strength at each time. For each value of Δ the collected data points were fit to an exponential curve using equation 1.

2.1.3 Bi-exponential Fitting Model

Another way to examine the behavior in the pore is to use a bi-exponential fit [7]. It is expected that there will be at least two different types of diffusion occurring in the sample, inter-particle and intra-particle. The shape of the exponential decay in signal can be represented as:

$$I_g = A_1 e^{-(\gamma\delta g)^2 t_{eff} D_1} + (1 - A_1) e^{-(\gamma\delta g)^2 t_{eff} D_2} \quad (2)$$

where A1 is the probability of the particle being in the pore, D_1 is the intra-particle diffusion and D_2 is the inter-particle diffusion. The probability of a solvent molecule being inside or outside of the pore depends on the amount of time that has elapsed. Since

the data was acquired at multiple Δ values, the bi-exponential fits can be performed for each data set.

2.1.4 Experimental Parameters

All experiments were performed at 14.1 T on a Varian 600-MHz NMR spectrometer using a 1.6 mm FastMAS^{TM} triple resonance probe operated at 599.6 MHz for ^{1}H. The probe was equipped with a gradient coil capable of producing gradients of up to ~.75 T/m (75 gauss/cm) along the magic angle. Gradients were calibrated using room temperature water as a standard. The measurement of bulk hexane was also done to confirm the calibration. The ^{1}H stimulated echo measurements were all done at room temperature, under static conditions to avoid any displacement of the sample due to vibrations of the MAS rotor during spinning. The following experimental parameters were used: ν_{RF}^{H}=100 kHz, δ = 2.5 ms or 10 ms with gradient strength arrayed up to 0.69 T/m, and Δ values ranging between 3 ms and 211 ms. Data were processed in Gsim and then transferred to Excel for calculation. The fitting of the exponential curves was done using Origin Pro 9.

2.2 Materials

2.2.1 AP-MSN and Non-porous Nanoparticle Synthesis

The synthesis of 3-aminopropyl mesoporous silica (AP-MSN) materials with 2.7 and 3.7 nm pores was done by Igor Slowing, Kapil Kandel, and Umesh Chaudhary as previously described [27-29]. AP-MSN-2.7 had a pore volume of 0.758 ml/g, a functional group loading of 1.5 mmol/g, and a silanol loading of 5.5 mmol/g. AP-MSN-3.7 had a pore volume of 1.11 ml/g, a functional group loading of 1.3 mmol/g, and a

silanol loading of 6.6 mmol/g. The presence of the functional groups and surfactant free pores were confirmed by ^{13}C cross polarization magic angle spinning (CPMAS) and ^{1}H direct polarization magic angle spinning (DPMAS) measurements. The pore volume was measured by were measured by nitrogen sorption isotherms in a Micromeritics Tristar 3000 using the Barrett-Joyner-Halenda (BJH) calculation methods.

The non-porous silica nanoparticles were synthesized by Igor Slowing using the following method. Concentrated ammonia (2.5 mL), water (2.8 mL) and ethanol (18.5 mL) were mixed in a 50 mL centrifuge tube. Tetraethyl orthosilicate (1.4 mL) was quickly added to the mixture, the tube was capped and the entire mixture was stirred overnight. The resulting colloid was centrifuged and washed four times with ethanol and two times with deionized water. The white solid was then dried overnight under vacuum at room temperature. The particles had a surface area of 11 m^2/g.

2.2.2 Loading of the Surface Groups

The loading of the functional groups and the silanol sites were measured by ^{29}Si Carr-Purcell-Meiboom-Gill (CPMG) DPMAS as reported in the chapter 4 and elsewhere [32]. Experiments were performed at 9.4 T on a Chemagnetics Infinity 400 Spectrometer equipped with a 5-mm MAS probe operated at 400.00 MHz (^{1}H) and 79.4 MHz (^{29}Si). Experimental parameters were described previously (see chapter 4 section 2.3.1). The parameters used in these experiments were ν_R = 10 kHz, ν_{RF}^{Si} = 50 kHz, ν_{RF}^{H} = 45 kHz, N_{CPMG} = 10, τ_{RD} = 300s, NS = 296, and AT = 25h. The chemical shifts of ^{29}Si, ^{13}C and ^{1}H are reported using the δ scale and are secondary referenced to tetramethylsilane (TMS) at 0 ppm.

2.2.3 Sample Preparation

The samples, AP-MSN-2.7 and AP-MSN 3.7, were packed into a 1.6 mm rotor and massed. The solvent (either water or hexane) was then introduced to the sample via pipette to reach filling factor of 1.3 by weight. The sample was then allowed to equilibrate overnight to allow for a homogenous distribution of the liquid throughout the entire volume.

3. Results and Discussion

3.1 Hexane

Hexane was added to AP-MSN-2.7 and AP-MSN-3.7, to achieve a pore filling factor of 1.3, as described before. The sample was then measured using a stimulated echo with pulsed field gradients. Data points were collected at multiple gradient strengths for each Δ value. An example plot of the signal intensity for AP-MSN-2.7 versus the gradient strength using a 2.5 ms gradient pulse length is shown in figure 2.

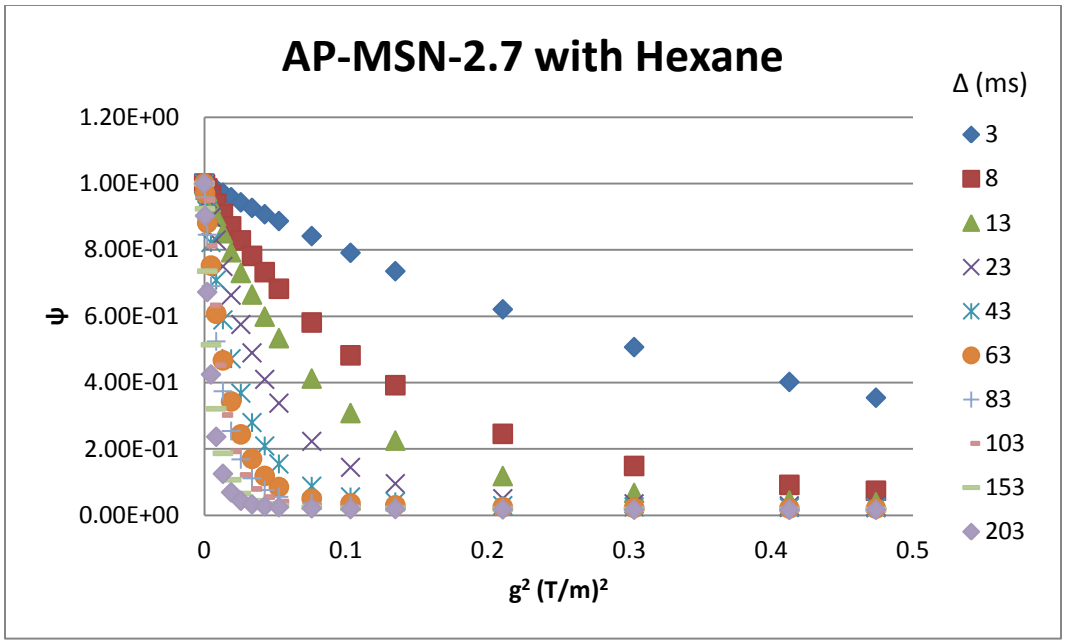

Figure 2. A plot of the signal intensity of hexane in AP-MSN-2.7 versus gradient strength for δ = 2.5 ms. Each data set was acquired at a different Δ value, as noted in the key. Notice the change in the curve shape as Δ increases. Similar data sets were obtained for AP-MSN-2.7 with hexane using δ = 10 ms and for AP-MSN-3.7 with hexane using δ = 2.5 ms and 10 ms.

3.1.1 *Effective Diffusion of Hexane*

For each value of Δ, a single exponential line (equation 1) was used to fit the data, the resulting in the D_{eff} values plotted in figures 3 and 4. These curves appear to fit the data with good accuracy. In both AP-MSN-2.7 and AP-MSN-3.7 the effective diffusion was slower than the bulk hexane diffusion of $4*10^{-9}$ m^2/s, as expected. However, D_{eff} of hexane in AP-MSN-2.7 is larger than in the AP-MSN- 3.7. There are two possibilities for this occurrence; either the diffusion in the AP-MSN-2.7 pores is faster than AP-MSN-3.7 or the intra-particle diffusion in the AP-MSN-2.7 is so slow that the inter-particle

diffusion overwhelms the measured effective diffusion curve. It seems reasonable that the second case is what is occurring here. Based on the filling factor, the molar ratio of particles in the pore versus outside of the pore should be approximately 3:1. This should weigh the diffusion coefficient in favor of the intra-particle diffusion; however, if the intra-particle diffusion is orders of magnitude slower than the inter-particle one, the latter term will dominate. We will confirm that the diffusion of hexane in AP-MSN-2.7 is indeed slower through another fitting method in the next section.

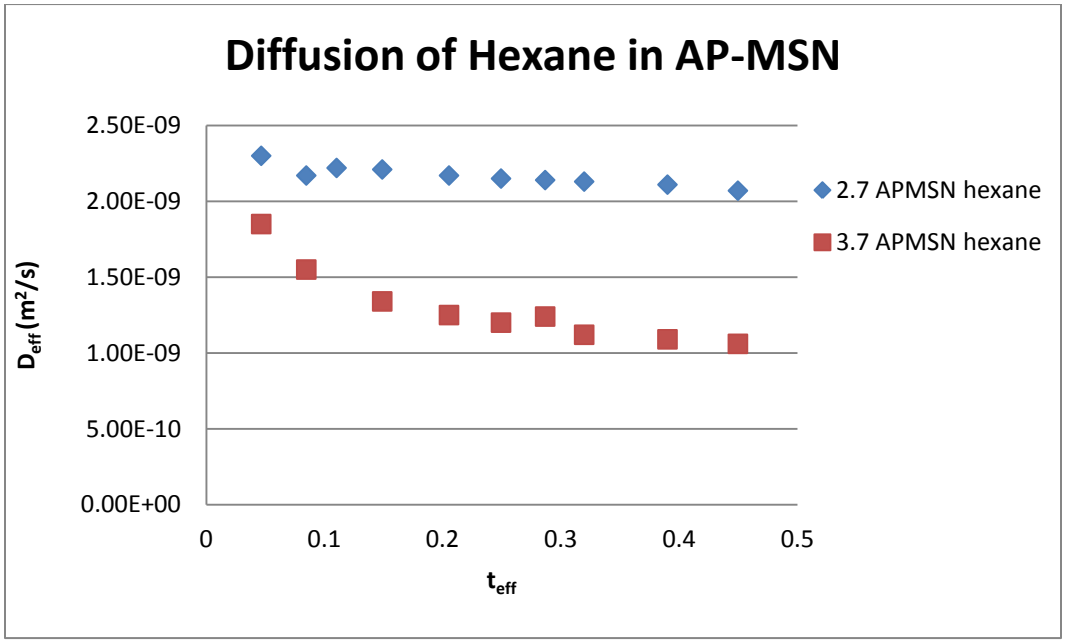

Figure 3. The D_{eff} of hexane in the pores of AP-MSNs using δ = 2.5 ms.

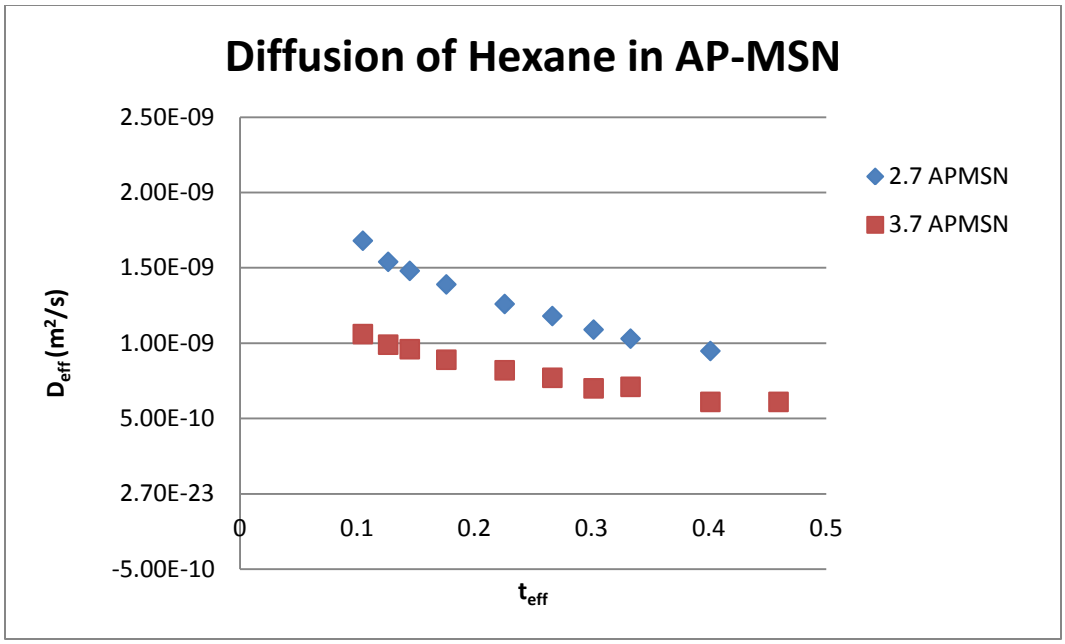

Figure 4. The D_{eff} of hexane in the pores of AP-MSNs using δ = 10 ms.

3.1.2 Bi-exponential Fit of Hexane Diffusion

To further examine the diffusion behavior of hexane within AP-MSNs, a bi-exponential fit (Eq. (2)) was applied to the data acquired with δ = 2.5 ms (shown in figure 3). To reduce the fitting error for intra-particle diffusion coefficient, a model system was used to independently measure the inter-particle diffusion. To this end, non-porous silica nanoparticles of similar size to AP-MSNs were exposed to 25% by weight of hexane. As expected, the resulting diffusion coefficient, $2.5*10^{-9}$ m^2/s, was lower than one measured for bulk hexane ($4*10^{-9}$ m^2/s). Using this value to mimic the inter-particle diffusion in AP-MSNs, the intra-pore diffusion in the AP-MSN-3.7 was fit to be $4*10^{-10}$ m^2/s. This agrees well with a previous report for similar sized MSNs [33]. In the smaller AP-MSN-2.7, the intra-pore diffusion was fit to approximately $8*10^{-11}$ m^2/s, which agrees well with the theorized slower diffusion in AP-MSN-2.7 from the effective diffusion

measurements. Note that the diffusion coefficient measured for non-porous silica is nearly equal to the D_{eff} value measured for AP-MSN-2.7, which further supports the notion that intra-particle diffusion is very slow in this sample. This leads to the conclusion that the diffusion coefficient of hexane is dependent on the pore size of the AP-MSN, and this restricted diffusion contributes to the overall decreased reaction rate in the smaller pores.

3.2 Water

Water was also introduced into the pores of AP-MSN-2.7 and AP-MSN-3.7 (filing factor of 1.3 by weight). Again data were acquired by varying the gradient strength for δ = 2.5 ms and 10 ms and several values of Δ. The data set obtained for AP-MSN-2.7 and δ = 2.5 ms is shown in figure 5.

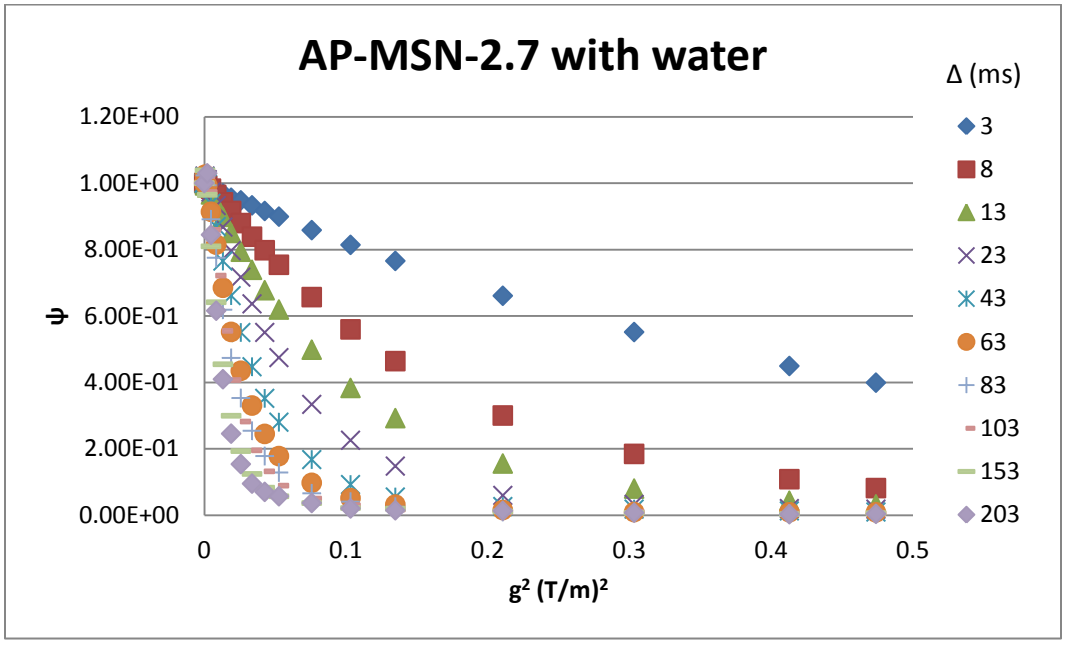

Figure 5. A plot of the signal intensity of water in AP-MSN-2.7 versus gradient strength for δ = 2.5 ms. Each data set was acquired at a different Δ value, as noted in the key.

Similar data was obtained for AP-MSN-2.7 with water using δ= 10 ms and for AP-MSN-3.7 with water using δ= 2.5 ms and 10 ms.

3.2.1 Effective Diffusion of Water

Similar to hexane, water exhibits restricted diffusion in AP-MSNs, as the measured D_{eff} values (figures 6 and 7) are smaller than in the bulk, $2.3*10^{-9}$ m^2/s. In contrast to hexane, however, there is little difference between the effective diffusion coefficients in AP-MSN-2.7 and AP-MSN-3.7. While this may lead to the idea that diffusion does not play a large role in the differences in reaction rate between pore sizes in water, the measurements of intra-particle diffusion proved challenging (see below).

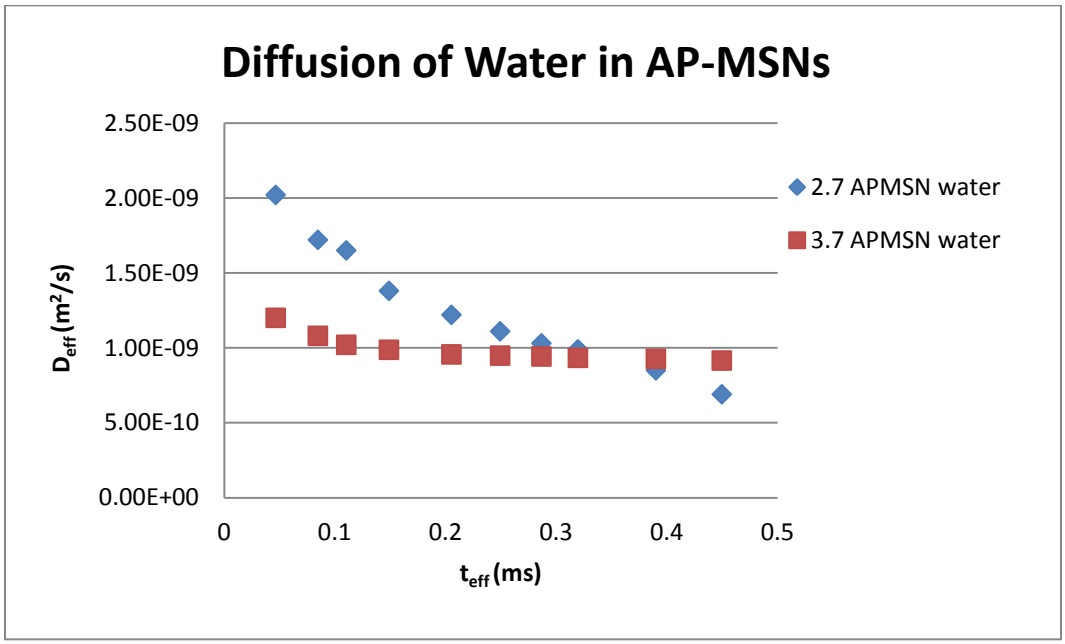

Figure 6. The D_{eff} of water in the pores of AP-MSNs using δ = 2.5 ms.

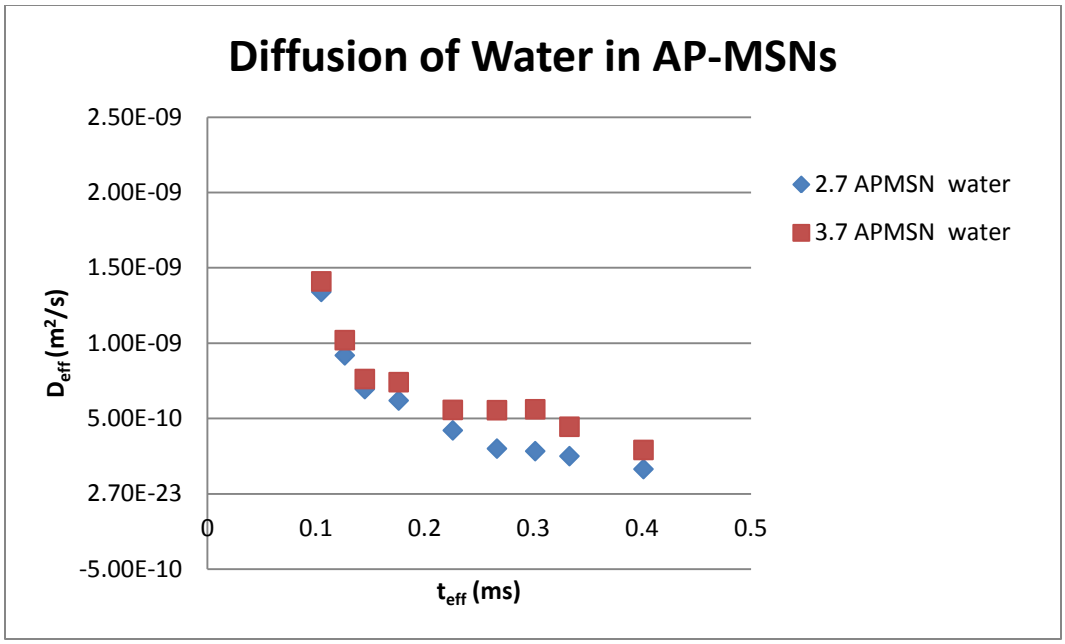

Figure 7. The D_{eff} of water in the pores of AP-MSNs using δ = 10 ms.

3.2.2 Bi-exponential Fit of Water Diffusion

Water was added to the non-porous nanoparticle so that is was approximately 25% water by weight. This mixture was allowed to disperse overnight; unfortunately, unlike the hexane-non-porous system, the measured diffusion coefficient showed a time dependence as a function of Δ. As the Δ delay was increased, the resulting measured diffusion coefficient decreased, which is typically observed in systems with restricted diffusion and multiple diffusion coefficients. Here, this may be attributed due to strong interaction between water molecules and the silanol groups on the silica surface [2], which can inhibit the overall diffusion between the non-porous nanoparticles. Hypothetically, at shorter times the only coefficient measured is that between the particles, but at longer times the slow diffusion of water along the surface is also taken into account. Consequently, we could not perform a reliable bi-exponential fit for the AP-

MSN-water system. At this point, this leaves the effect of water on diffusion in the AP-MSN pores unclear.

3.3 Water vs. Hexane

In our previous paper [2] it was shown that the reaction rate in water was 10 times higher than in hexane for AP-MSN. This effect can be attributed to a favorable equilibrium; however, it was unclear if diffusion plays any role. Comparing the diffusion coefficients at similar effective times, the D_{eff} of water in the MSN is slightly lower than that of hexane, despite water having the higher reaction rate. However, whether or not water diffusion plays a role in AP-MSN's activity cannot be determined without a reliable measurement of its intra-particle diffusion. Such measurement will require the use of stronger gradients to provide better spatial resolution. Another approach could be the use of a changing solvent concentration in order to effectively separate the intra- and inter-particle coefficients.

4. Conclusion

In this study, stimulated echo with pulsed field gradients was used to measure the diffusion of two different solvents, water and hexane, in AP-MSN-2.7 and AP-MSN-3.7. The resulting data were then fit using two different methods.

Based on these fits, the diffusion of hexane in AP-MSN-2.7 was shown to be slower than in the larger pores. This agrees well with our studies of catalytic activity, which show an increase in the reaction rate with the increase in pore size. Thus, both substrate inhibition and diffusion played a role in the decreased efficiency of the AP-MSN with small pore sizes.

When water was introduced to AP-MSNs, the aldol reaction showed an increase in the overall rate compared to that observed for hexane. Our PFG NMR measurements showed no significant difference in the effective diffusion coefficient with a change in pore size. However, the critical measurement of intra-particle diffusion coefficient could not be reliably performed. And thus it remains unclear if diffusion played a role in this difference, or if it was only the favorable equilibrium and the cooperation of water with the surface catalyst, as was previously discussed [2].

Whereas these studies provided some useful insights, they should be considered as an exploratory investigation. Due to the limitations of the probe components (weak gradient strengths), in some cases the time a molecule spent in a pore was significantly shorter than the length of the gradient pulse. For example, the pore lengths in the AP-MSNs were on the order of 200 nm. Thus, a molecule diffusing at $8*10^{-11}$ m^2/s (D_{intra}, hexane) would spend approximately 0.1 ms to travel the length of a pore, which is considerably shorter than the employed gradient pulses.

In future studies, stronger gradients will have to be employed to allow for the use of shorter pulse lengths and thereby separate the effects of intra- and inter-particle diffusion. The length of the gradient pulse can be arrayed to explore its effect on the measurement of effective diffusion (especially in the multi-coefficient case). The effect of concentration should be studied to determine the optimal filling factor. The effect of pore length on the diffusion coefficient could be examined, as well. In particular, larger nanoparticles with longer pores should be used to increase the residence time of molecules within a single pore. Pores with larger diameter could be used to determine the limitations of the diffusion effects seen in hexane.

The future studies should also involve examining the diffusion of reactants and the reaction products within the system using different solvents. To separate the individual resonances, magic angle spinning may need to be employed to provide adequate spectral resolution. In this case the reliability of spatially stable spinning would need to be explored to a greater degree.

5. Acknowledgements

Thank you to Igor Slowing, Kapil Kandel, and Umesh Chaundary for the synthesis of the AP-MSN and for the inspiration for this study. This research was supported at the Ames Laboratory by the U.S. Department of Energy, Office of Basic Energy Sciences. Ames Laboratory is operated for the U.S. Department of Energy by Iowa State University under Contract No.DE-AC02-07CH11358.

6. References

[1] K. Kandel, S.M. Althaus, C. Peeraphatdit, T. Kobayashi, B.G. Trewyn, M. Pruski, and I.I. Slowing, Journal of Catalysis 291 (2012) 63-68.

[2] K. Kandel, S.M. Althaus, C. Peeraphatdit, T. Kobayashi, B.G. Trewyn, M. Pruski, and I.I. Slowing, ACS Catalysis 3 (2013) 265-271.

[3] W.S. Price, Concepts in Magnetic Resonance 9 (1997) 299-336.

[4] W.S. Price, Concepts in Magnetic Resonance 10 (1998) 197-237.

[5] R. Valiullin, and J. Kärger, Chemie Ingenieur Technik 83 (2011) 166-176.

[6] H. Mehrer, Diffusion in Solids: Fundamentals, Methods, Materials, Diffusion-Controlled Processes, Springer, 2007.

[7] J. Kärger, American Institute of Chemical Engineers Journal 28 (1982) 417-423.

[8] F. Stallmach, A. Gräser, J. Kärger, C. Krause, M. Jeschke, U. Oberhagemann, and S. Spange, Microporous and Mesoporous Materials 44–45 (2001) 745-753.

[9] F. Courivaud, E.W. Hansen, A. Karlsson, S. Kolboe, and M. Stöcker, Microporous and Mesoporous Materials 35–36 (2000) 327-339.

[10] C. Krause, F. Stallmach, D. Honicke, S. Spange, and J. Kärger, Adsorption 9 (2003) 235-241.

[11] F. Courivaud, E.W. Hansen, S. Kolboe, A. Karlsson, and M. Stöcker, Microporous and Mesoporous Materials 37 (2000) 223-232.

[12] T. Kirchner, A. Shakhov, P. Zeigermann, R. Valiullin, and J. Kärger, Carbon 50 (2012) 4804-4808.

[13] M. Dvoyashkin, R. Valiullin, and J. Karger, Physical Review E 75 (2007) 041202.

[14] R. Valiullin, M. Dvoyashkin, P. Kortunov, C. Krause, and J. Kärger, The Journal of Chemical Physics 126 (2007) 054705.

[15] E.W. Hansen, F. Courivaud, A. Karlsson, S. Kolboe, and M. Stöcker, Microporous and Mesoporous Materials 22 (1998) 309-320.

[16] E.L. Hahn, Physical Review 80 (1950) 580.

[17] J. Kärger, and D. Ruthven, Diffusion in Zeolites and Other Microporous Solids, John Wiley & Sons, 1992.

[18] E.O. Stejskal, and J.E. Tanner, Journal Chemical Physics 42 (1965) 288-292.

[19] D.E. Woessner, Review of Scientific Instruments 31 (1960) 1146-1146.

[20] W. Dai, M. Scheibe, L. Li, N. Guan, and M. Hunger, The Journal of Physical Chemistry C 116 (2011) 2469-2476.

[21] C. D'Agostino, G.L. Brett, P.J. Miedziak, D.W. Knight, G.J. Hutchings, L.F. Gladden, and M.D. Mantle, Chemistry – A European Journal 18 (2012) 14426-14433.

[22] M.D. Mantle, D.I. Enache, E. Nowicka, S.P. Davies, J.K. Edwards, C. D'Agostino, D.P. Mascarenhas, L. Durham, M. Sankar, D.W. Knight, L.F. Gladden, S.H. Taylor, and G.J. Hutchings, The Journal of Physical Chemistry C 115 (2010) 1073-1079.

[23] R. Valiullin, J. Kärger, K. Cho, M. Choi, and R. Ryoo, Microporous and Mesoporous Materials 142 (2011) 236-244.

[24] P. Zeigermann, S. Naumov, S. Mascotto, J. Kärger, B.M. Smarsly, and R. Valiullin, Langmuir 28 (2012) 3621-3632.

[25] V.V. Loskutov, and V.A. Sevriugin, Journal of Magnetic Resonance 230 (2013) 1-9.

[26] F. Stallmach, S. Gröger, V. Künzel, J. Kärger, O.M. Yaghi, M. Hesse, and U. Müller, Angewandte Chemie International Edition 45 (2006) 2123-2126.

[27] A.R. Menjoge, Q. Huang, B. Nohair, M. Eic, W. Shen, R. Che, S. Kaliaguine, and S. Vasenkov, The Journal of Physical Chemistry C 114 (2010) 16298-16308.

[28] J. Kärger, Advances in Colloid and Interface Science 23 (1985) 129-148.

[29] G. Marcel, H. Stefan, W. Markus, S. Frank, and G. Petrik, New Journal of Physics 13 (2011) 045016.

[30] J.-F. Kuntz, P. Palmas, V. Level, and D. Canet, Journal of Magnetic Resonance 191 (2008) 239-247.

[31] J.E. Tanner, The Journal of Chemical Physics 52 (1970) 2523-2526.

[32] S. Meiboom, and D. Gill, Review of Scientific Instruments 29 (1958) 688-691.

[33] Z. Adem, F. Guenneau, M.-A. Springuel-Huet, A. Gédéon, J. Iapichella, T. Cacciaguerra, and A. Galarneau, The Journal of Physical Chemistry C 116 (2012) 13749-13759.

CHAPTER 6: CONCLUSIONS

Solid State NMR is a versatile technique which is applicable to many types of solid materials in chemistry, biology and materials science. New technical advances have led to the use of sequences in solids which were previously available only in solution state. This has allowed for the study of a variety of systems, from carbonaceous disordered coals to well-ordered mesoporous nanoparticles to natural abundance low gamma nuclei. These advances have also lead to the measurement of effective self diffusion coefficients in confined liquids.

In chapter 2 new advancements in high field and fast MAS technology were utilized to update the protocol for the measurement of coals and other carbonaceous materials. The standard Argonne Premium Coal Samples were used to test sensitivity and resolution. The 1D experiments preformed at high fields and under fast MAS were shown to be only slightly less sensitive in comparison to the traditional experiments, while providing improved resolution. More importantly, fast MAS enabled the measurement of 2D and *J*-coupling filtered spectra of these materials for the first time. These experiments proved to be easy to implement, requiring no need for homonuclear decoupling (CRAMPS), while still maintaining quantative accuracy.

The detection of natural abundance ^{15}N spectra was shown in chapter 3. Despite the low natural abundance of ^{15}N, 2D indirectly detected spectra, both through-space and through-bond, were acquired for bulk species. For the first time, a ^{1}H detected, ^{15}N natural abundance spectrum of a surface bound species was acquired in 2D, which was enabled by the 15-fold sensitivity gain compared to the traditional protocol utilizing the

^{15}N detection. INEPT magnetization transfers were also examined, showing that the magnetization transfer via *J*-coupling is indeed occurring. The remarkable efficiency of CP transfer at fast MAS was shown by comparison of HMB spectra at different MAS rates.

In chapter 4 the aldol reaction between *p*-nitrobenzaldehyde and acetone as catalyzed by amine functionalized MSN was studied using spectroscopic techniques, which lead to a better catalyst design. A stable Schiff bases was found to form in the primary amine (AP-MSN) when hexane was used as the solvent, which led to a decrease in reactivity. The group was then chemically altered to be a secondary amine (MAP-MSN) and the reactivity increased. The Schiff base was shown to be reversible and therefore a new solvent, water, was used. When water was used as a solvent, the reactivity of AP-MSN increased 10-fold, while the MAP-MSN decreased dramatically. This increase in AP-MSN may be attributed to a change in equilibrium of the formed intermediates. The cooperative effect of surface silanols in the reaction was shown to play a role in the overall higher activity seen in the heterogeneous catalysts.

Chapter 5 is a continuation of the aldol condensation study from the previous chapter. The diffusion of the two solvents, hexane and water, within an AP-MSN system was explored using PFG NMR. 3.7 and 2.7 nm AP-MSN samples were used for the diffusion comparison. In the AP-MSNs with smaller pores the diffusion of hexane within the pore was much slower than in the larger pore system, which contributed to the lower activity of this catalyst in aldol reaction. In water, the difference in intra-particle diffusion between samples with different pore sizes could not be unambiguously established.